Correlated Voltage Dependent- and Magnetic-Reflectometry at Transition Metal/Insulator Heterostructures

Von der Fakultät Mathematik und Physik
der Universität Stuttgart zur Erlangung der Würde eines
Doktors der Naturwissenschaften (Dr. rer. nat.)
genehmigte Abhandlung

Vorgelegt von
Sven Erik Ilse
aus Stuttgart

Hauptberichter:	PD Dr. Eberhard Goering
Mitberichter:	Prof. Dr. Peter Michler

Tag der mündlichen Prüfung: 01.08.2023

Max-Planck-Institut für Festkörperforschung, Stuttgart
2023

Sven Erik Ilse: *Correlated Voltage Dependent- and Magnetic-Reflectometry at Transition Metal/Insulator Heterostructures.*

Betreuer:
PD Dr. Eberhard Goering

Zeitraum:
2018 - 2023

Contents

Acronyms

CCL copper clad laminate

DOS density of states

EDX energy-dispersive x-ray spectroscopy

EELS electron energy loss spectroscopy

ERNSt Stuttgart Novel Reflectometer Experiment

FIB focused ion beam

FYB fluorescence yield background

GMR giant magnetoresistance

LED light-emitting diode

MCA magnetocrystaline anisotropy

MOS-FET metal-oxide-semiconductor field-effect transistor

MRAM magnetoresistive random-access memory

MTJ magnetic tunnel junction

PMA perpendicular magnetic anisotropy

RAM random-access memory

SHE spin Hall effect

SOT spin-orbit torque

SQUID superconducting quantum interference device

STT spin-transfer torque

TEM transmission electron microscopy

TEY total electron yield

TFY total fluorescence yield

TM transition metal

TMR tunnel magnetoresistance

UHV ultra-high vacuum

VCMA voltage control of magnetic anisotropy

VXRR voltage x-ray reflectometry

XAS x-ray absorption spectroscopy

XMCD x-ray magnetic circular dichroism

XRMR x-ray resonant magnetic reflectometry

XRR x-ray reflectometry

Abstract

Magnetism is an integral part of our everyday lives. Whether in the form of permanent and electromagnets in electromotors and generators, or simply as fridge magnets. In particular, the magnetism of thin films has become increasingly important for modern technology in the last decades. Closely related is the research field of spintronics, which explores the interaction of electron spin and electron charge and how they can be used to process and represent information.

Spintronic devices are typically built from thin film samples consisting of magnetic, non-magnetic, and insulating layers. Such devices utilize a variety of effects, all of which depend critically on the structural and magnetic properties of the thin layers, as well as electronic transport phenomena at the interfaces. Therefore, precise knowledge of the element-specific, depth dependent structural and magnetic properties, with special focus on the interfaces, is indispensable for the design of spintronic devices and the improvement of their functionality.

Information on interfacial electronic states at the Fermi energy and how they are influenced by an applied electric field is essential for a better un-

derstanding of electronic transport properties at interfaces. However, extracting this information, especially in the case of buried layers, is not trivial. An experimental method capable of obtaining such information would be of interest not only for spintronic devices, but also for conventional electronic devices such as metal-oxide-semiconductor field-effect transistors (MOS-FETs), capacitors, or solid-state electrolyte lithium batteries, and for recently emerging topics such as 2D materials and topological insulators.

In this thesis, layered structures that are similar to those widely used in spintronic devices, consisting of layers of SiO_2, magnetic transition metals (TMs), Cr, and Au are studied.

In the first part of the thesis, the resonant (magneto-)optical x-ray parameters of the used materials are retrieved from x-ray absorption spectroscopy (XAS) and x-ray magnetic circular dichroism (XMCD) measurements. Here, the TM L-edges and the O K-edge are of interest for this study. The knowledge of the resonant optical parameters is a prerequisite for the analysis of the reflectometry data in the second and third part of this thesis.

The second part of the thesis is dedicated to the study of structural and magnetic properties of $Si/SiO_2/TM/Cr/Au$ layer stacks, with the TMs of interest being Fe, Co, and Ni. X-ray reflectometry (XRR) and x-ray resonant magnetic reflectometry (XRMR) measurements are utilized in order to retrieve high resolution depth dependent structural and magnetic properties. The influence of small structural variations on the magnetic properties of the whole TM layer as well as on the magnetic properties at the interfaces are investigated. Complementary superconducting quantum interference device (SQUID) measurements allow quantification of the observed magnetization reduction of the thin TM layers. Different effects

leading to the magnetization reduction, namely a reduced effective Curie temperature and intermixing at the interfaces, are disentangled.

In the third and central part, the new measurement technique of voltage x-ray reflectometry (VXRR) is presented, which was developed in the context of this work. For voltage x-ray reflectometry (VXRR) measurements, an electric field is applied to a sample containing an insulating layer, and voltage-induced variations of the reflected x-ray intensity are measured. These intensity variations originate from tiny changes in the x-ray optical properties induced by electrons (de)populating interfacial states at the Fermi energy at the interface to the insulating layer. The changes of x-ray optical properties are directly related to changes in the electronic structure. Thus, with VXRR it becomes possible to measure electric-field-induced changes to interfacial electronic structures in an element-specific manner.

The experimental details of this new measurement technique are presented and a scheme for the analysis of VXRR data is outlined. First successful VXRR measurements on a $Si/SiO_2/Ni/Cr/Au$ layer stack are shown. The electric-field-induced changes to the x-ray optical properties at the Ni L_3-edge and the O K-edge are retrieved. The results show that the average oxidation state of interfacial Ni atoms is changed by the applied voltage and that the interfacial states at the Fermi energy for Ni have no measurable spin polarization with the current noise level of the experiment. Furthermore, only about 40 % of the electrons that are moved to the SiO_2/Ni interface (de)populate Ni states. A strong electric-field-induced effect on the interfacial electronic structure of O atoms at the Si/SiO_2 and the SiO_2/Ni interface could be measured.

The results presented in this thesis can provide better understanding of interfacial effects in spintronic devices and might help to design future devices with improved functionality. The newly developed method of VXRR yields the possibility to gain insight in the interfacial electronic structure

of buried layers and has a great potential for many different systems in solid-state research.

Zusammenfassung

Magnetismus ist ein fester Bestandteil unseres alltäglichen Lebens, sei es in Form von Elektro- und Permanentmagneten in Elektromotoren und Generatoren oder auch nur als einfacher Kühlschrankmagnet. In den letzten Jahrzehnten hat außerdem der Magnetismus dünner Schichten für moderne technologische Anwendungen stetig an Bedeutung gewonnen. Damit eng verbunden ist das Forschungsgebiet der Spintronik, welches die Wechselwirkung zwischen Spin und Ladung des Elektrons untersucht und wie Informationen durch sie dargestellt und verarbeitet werden können.

Spintronische Bauelemente bestehen in der Regel aus einer Reihe verschiedener magnetischer, nichtmagnetischer und isolierender Dünnschichten. Für die Funktionalität solcher Bauelemente spielen eine Vielzahl physikalischer Effekte eine Rolle, die oft entscheidend von den strukturellen und magnetischen Eigenschaften der dünnen Schichten sowie von elektronischen Transportphänomenen an den Grenzflächen abhängen. Für das Design und die Weiterentwicklung spintronischer Bauelemente ist daher eine genaue Kenntnis der elementspezifischen, tiefenabhängigen strukturellen und magnetischen Eigenschaften unter besonderer Berücksichtigung

der Grenzflächen unerlässlich.

Die elektrischen Transporteigenschaften an Grenzflächen hängen dabei entscheidend von den elektronischen Grenzflächenzuständen an der Fermi-Kante und deren mögliche Beeinflussung durch äußere elektrische Felder ab. Die Untersuchung dieser Grenzflächenzustände und deren Beeinflussung ist dabei keineswegs trivial, besonders wenn die zu untersuchenden Grenzflächen von anderen Schichten verdeckt sind. Eine experimentelle Methode, die in der Lage ist, solche Informationen zu liefern, wäre nicht nur für spintronische Bauelemente von Interesse, sondern auch für konventionelle elektronische Bauelemente wie Metall-Oxid-Halbleiter-Feldeffekttransistoren, Kondensatoren oder Lithiumbatterien mit Festkörperelektrolyten sowie für aktuell interessante Themen in der Grundlagenforschung wie 2D-Materialien und topologische Isolatoren.

In dieser Arbeit werden Dünnschichtsysteme untersucht, die eine große Ähnlichkeit mit vielen spintronischen Bauelementen aufweisen. Die untersuchten Proben bestehen aus dünnen SiO_2, magnetischen Übergangsmetall, Cr und Au-Schichten.

Im ersten Teil der Arbeit werden die resonanten (magneto)optischen Röntgeneigenschaften der verwendeten Materialien durch Röntgenabsorptionsspektroskopie (engl. x-ray absorption spectroscopy (XAS)) und durch Messungen des zirkularen magnetischen Röntgendichroismus (engl. x-ray magnetic circular dichroism (XMCD)) ermittelt. Dabei sind insbesondere die optischen Eigenschaften an den Übergangsmetall L-Kanten und an der O K-Kante für diese Arbeit von Interesse. Die Kenntnis der genauen resonanten optischen Eigenschaften ist eine Voraussetzung für die Analyse der Reflektometriedaten im zweiten und dritten Teil dieser Arbeit.

Der zweite Teil der Arbeit ist der Untersuchung der strukturellen und magnetischen Eigenschaften von Si/SiO_2/Übergangsmetall/Cr/Au-Schicht-

systemen gewidmet, wobei die Übergangsmetalle Fe, Co und Ni von Interesse sind. Konventionelle Röntgenreflektometrie (engl. x-ray reflectometry (XRR)) und resonante, magnetische Röntgenreflektometrie (engl. x-ray resonant magnetic reflectometry (XRMR)) werden verwendet, um hochauflösende tiefenabhängige strukturelle und magnetische Eigenschaften zu bestimmen. Der Einfluss kleiner struktureller Variationen auf die magnetischen Eigenschaften der gesamten Übergangsmetall-Schicht sowie auf die magnetischen Eigenschaften an den Grenzflächen wird untersucht. Ergänzende Messungen mit einem SQUID-Magnetometer ermöglichen die Quantifizierung der beobachteten Magnetisierungsverringerung der dünnen Übergangsmetall-Schichten. Es werden verschiedene Effekte, die zur Magnetisierungsverringerung führen, nämlich eine verringerte effektive Curie-Temperatur und die Vermischung von Elementen an den Grenzflächen, diskutiert.

Im dritten Teil, dem Kernstück der Arbeit, wird die neue Messmethode Spannungs-Röntgenreflektometrie (engl. voltage x-ray reflectometry (VXRR)) vorgestellt, die im Rahmen dieser Arbeit entwickelt wurde. Bei VXRR-Messungen wird ein elektrisches Feld an eine Probe mit einer isolierenden Schicht angelegt und die spannungsinduzierten Intensitätsänderungen der reflektierten Röntgenstrahlung werden gemessen. Diese Intensitätsänderungen entstehen durch kleinste Änderungen der röntgenoptischen Eigenschaften, welche durch Elektronen verursacht werden, die an der Grenzfläche zur isolierenden Schicht Grenzflächenzustände an der Fermi-Energie be- und entvölkern. Die Änderung der röntgenoptischen Eigenschaften steht in direktem Zusammenhang mit Änderungen der elektronischen Struktur. Mit Hilfe von VXRR-Messungen ist es daher möglich, spannungsinduzierte Änderungen der elektronischen Struktur an Grenzflächen zu messen.

Die experimentellen Details dieser neuen Messtechnik werden vorgestellt und ein Schema für die Analyse von VXRR-Daten wird umrissen.

Erste erfolgreiche VXRR-Messungen an einem $Si/SiO_2/Ni/Cr/Au$-Schichtsystem werden gezeigt. Die durch das elektrische Feld induzierten Änderungen der röntgenoptischen Eigenschaften an der Ni L_3-Kante und der O K-Kante werden ermittelt. Die Ergebnisse zeigen, dass die durchschnittliche Oxidationszahl der Ni-Atome an der Grenzfläche durch die angelegte Spannung verändert wird und dass die Grenzflächenzustände für Ni-Atome an der Fermi-Energie bei gegebenem Rauschniveau aktuell nicht messbar spinpolarisiert sind. Außerdem besetzten nur etwa 40 % der Elektronen, die zur SiO_2/Ni-Grenzfläche bewegt werden, Ni-Zustände. Zusätzlich konnte ein starker, durch das elektrische Feld induzierter Effekt auf die elektronische Struktur der O-Atome an der Si/SiO_2 und der SiO_2/Ni-Grenzfläche gemessen werden.

Die Ergebnisse dieser Arbeit können dazu beitragen, Grenzflächeneffekte in spintronischen Bauelementen besser zu verstehen und zukünftig Bauelemente mit verbesserter Funktionalität zu entwickeln. Die neu entwickelte VXRR-Methode bietet die Möglichkeit, Einblicke in die elektronische Struktur an Grenzflächen von verdeckten Schichten zu gewinnen und hat ein großes Potenzial für viele verschiedene Systeme in der Festkörperforschung.

Introductions

Chapter 1

General Introduction

Magnetism is an integral part of our everyday lives. Whether in the form of permanent and electromagnets in electromotors of all kinds and sizes, in bearings, in generators or even just as fridge magnets. In the last decades, the magnetism of thin films has received a lot of attention. Since the discovery of the giant magnetoresistance (GMR) in 1988 by Peter Grünberg [1] and Albert Fert [2], magnetic thin film systems have become an essential part of modern technology, especially in information technology. Without the GMR and also the tunnel magnetoresistance (TMR) [3,4] effect, modern magnetic field sensors and hard disk drives would not exist in their present form. The discovery of the GMR effect, for which Grünberg and Fert received the Nobel Prize in 2007, opened the research field that is known today as *spintronics* [5–11].

In spintronics, it is no longer only the charge of the electron that is used to represent and process information, but also the spin and the associated magnetic moment of the electron. Nowadays, there are a variety of effects

that are utilized to measure and manipulate the magnetization of thin layers in spintronic devices, in addition to the GMR and TMR effect. One important example is the spin Hall effect (SHE), where an electric current through a heavy metal generates a spin polarization at its interface which can be used to manipulate magnetic layers by utilizing the related spin-orbit torque (SOT) [12,13]. Another important effect is the voltage control of magnetic anisotropy (VCMA), where the magnetic anisotropy can be altered by an applied electric field, which can be used to assist magnetization switching of thin layers [14,15]. Also worth mentioning is the effect of spin-transfer torque (STT), where a spin polarized current is used to exert a torque to a magnetic layer and thereby exciting oscillations or switching the magnetization direction [16]. There are many spintronic devices based on these effects already in use in current technology, but they are also still the subject of ongoing fundamental research [11]. Examples for such spintronic devices are: magnetic field sensors [17], read heads of hard disk drives [18], spin-torque oscillators [18,19], devices for neuromorphic computing [20,21], racetrack memories [22,23] or magnetoresistive random-access memory (MRAM) [24,25]. The MRAM is a non-volatile memory in which data is stored by the relative magnetization orientation of two magnetic layers in so called magnetic tunnel junctions (MTJs). MRAMs seek to combine the advantages of conventional volatile random-access memorys (RAMs), namely their speed, with the ability to store information in a non-volatile manner, similar to Flash or magnetic memories [26].

For all the effects that are utilized in spintronic devices, electronic transport phenomena through and at interfaces and the interfacial electronic structures play a crucial role. Such devices typically consist of multiple thin magnetic, non-magnetic, and insulating layers, and their functionality depends critically on their microscopic structural and magnetic properties, especially those at the interfaces. Characteristic physical values such as the magnetoresistance, the spin Hall angle or the spin dif-

fusion lengths, which are important for the functionality, are extremely sensitive to structural properties and show large variations throughout literature [27–32]. Thus, it is important to exactly know and control element-specific, depth dependent structural and magnetic properties of such thin layered systems in order to design highly functional spintronic devices. However, experimental techniques that yield depth dependent structural and magnetic information on buried layers and their interfaces are rare. Transmission electron microscopy (TEM) and neutron reflectometry are two experimental techniques that can yield this kind of information, but TEM measurements require sophisticated sample preparation techniques, and neutron reflectometry does not have a high element specificity and measurement times are long.

Another experimental technique to obtain this kind of information is x-ray resonant magnetic reflectometry (XRMR). It combines x-ray reflectometry (XRR) with x-ray magnetic circular dichroism (XMCD) and allows to obtain element-specific depth dependent structural and magnetic properties with high depth resolution and with an extremely high interface sensitivity. One of first experiments where XRMR was used to study structural and magnetic interfacial profiles was performed by Geissler et al. at Pt/Co bilayers [33]. Since then, many studies have been performed utilizing XRMR, revealing detailed information about interfacial magnetic structures and their correlation with the interfacial structure in a multitude of different systems [34–39]. XRMR is also capable of retrieving interfacial electronic properties such as the valence state of Fe atoms at the Fe_3O_4/ZnO interface [40], or retrieving spatially resolved electronic structures and depth dependent orbital polarization profiles of superlattices [41–44].

Electronic transport phenomena and electronic structures at interfaces play a central role not only in spintronics, but also in conventional electronic devices such as capacitors [45,46], MOS-FETs [47–49], or solid-state electrolyte lithium batteries [50–52]. Recently, much attention has also been

paid to topological insulators[53,54] and 2D materials[55], where interfacial electronic transport phenomena determine their properties. In all these applications, the interfacial electronic structure and especially the electronic states at the Fermi energy are of interest, since these states are the ones involved in electronic transport phenomena and are (de)populated when an electric field is applied. However, there is no straightforward way to study the states at the Fermi energy at buried interfaces and how they change under applied voltages.

The first part of this thesis deals with the measurement of resonant (magneto) optical x-ray parameter by means of x-ray absorption spectroscopy (XAS) and XMCD. The exact knowledge of them is necessary for the second and third part of this thesis.

In the second part of this thesis, layered structures that are similar to those that are widely used in spintronic devices, consisting of SiO_2, magnetic TMs, Cr, and Au layers are studied by means of XRMR and SQUID-magnetometry. Element-specific, high resolution depth dependent chemical and magnetic profiles are obtained for these samples. The magnetic properties of the thin TM layers and their sensitivity to structural parameters will be studied, with particular emphasis on the interfacial properties. For the analysis of the XRMR data, the exact resonant x-ray (magneto-)optical properties are necessary, which were retrieved in the first part.

The third part of this thesis is dedicated to the development of a new measurement method called voltage x-ray reflectometry (VXRR). In VXRR, a voltage is applied to a layered sample that includes an insulating layer and the electric-field-induced variations of the reflected x-ray intensity are measured. This intensity variations originate from tiny changes in the x-ray optical properties, which are directly related to changes in the

interfacial electronic structure, since electrons that are moved by the electric field (de)populate interfacial states at the Fermi energy. Thus, with VXRR it is now possible to study interfacial states at the Fermi energy and electric-field-induced changes to them at buried interfaces.

First successful VXRR measurements will be presented, measured on a sample consisting of SiO_2, Ni, Cr, and Au layers, and a scheme to analyze VXRR data is introduced on the basis of this data.

Chapter 2

Introduction to Related Physical Concepts

2.1 Stoner model of ferromagnetism

The ferromagnetism of the magnetic 3d transition metals can be explained by the Stoner model for band ferromagnetism [56–58], which successfully describes their non integer values of the magnetic moments. A band structure arises when many atoms form a periodic structure (i.e. a crystal). Because the electron wave functions overlap with each other the discrete atomic states are smeared out into continuous bands due to the Pauli principle. The resulting band structure shows the allowed energy states for a given electron wave vector k, and the density of states (DOS) can be obtained from the band structure by summing over all possible k values within the Brillouin zone [56].

In Fig. 2.1, the density of states $D(E)$ of the 3d electrons is for simplicity approximated by a semicircle. The DOS is separated into states

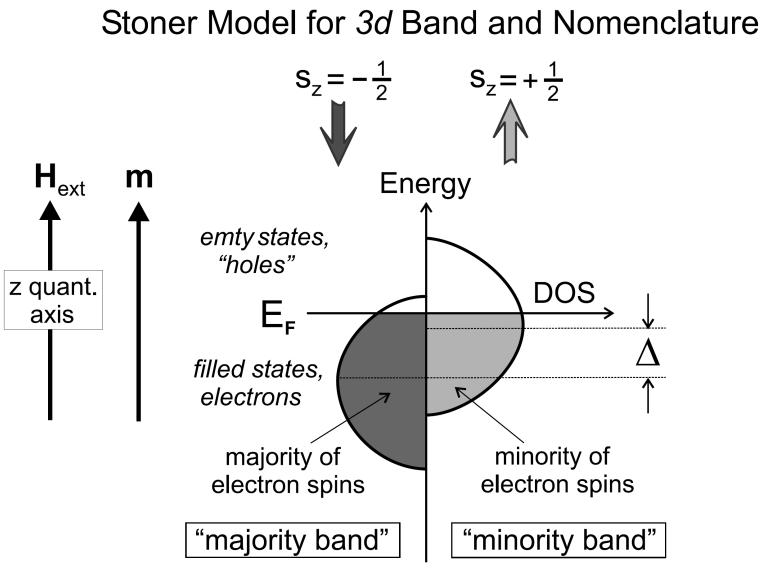

Figure 2.1: Schematic illustration of the 3d density of states (DOS) and how the majority and minority bands are shifted by the exchange splitting in band ferromagnetism. The figure is taken from [56] .

with spin up and spin down, and the two halves of the DOS are shifted with respect to each other by the exchange splitting energy Δ. The exchange splitting can be described by a simplified molecular field and has its quantum mechanical origin in the exchange interaction [56,59,60]. All states up to the Fermi energy E_F are filled and the spin states that have the larger population are called majority states and the ones with the lower population minority states. The magnetic moment can be calculated by the difference in number of electrons in the majority states and minority states, which are obtained by integrating the respective part of the DOS from $E = -\infty$ to $E = E_F$.

The Stoner criterion [56,61]

$$UD(E_F) \geq 1 \tag{2.1}$$

with the Stoner parameter U, that is calculated from the exchange and Coulomb interaction for a given material, and the DOS at the Fermi energy $D(E_\mathrm{F})$, is used to determine whether a material shows a spontaneous magnetization.

The Curie temperature T_C is the temperature above which the ferromagnetic order of a ferromagnetic material disappears. Within the frame of the Stoner model T_C can be determined via [56]

$$U \int_0^\infty D(E) \left| \frac{\partial f(T_\mathrm{C})}{\partial E} \right| = 1, \tag{2.2}$$

with the Fermi function $f(T)$ given by:

$$f(T) = \frac{1}{e^{(E-\mu)/k_\mathrm{B}T} + 1}. \tag{2.3}$$

However, this formalism fails to describe the temperature dependence and Curie temperature in real systems appropriately (as it overestimates T_C by an order of magnitude), thus the temperature dependence of magnetization is usually described by the mean-field Weiss-Heisenberg model. In this model the Curie temperature T_C can be calculated via [56]

$$T_\mathrm{C} = \frac{2\langle s \rangle^2 J_0}{3k_\mathrm{b}}, \tag{2.4}$$

with the expectation value of the atomic spin moment $\langle s \rangle$, the Boltzmann constant k_b, and the exchange constant J_0 given by the sum over all neighbors

$$J_0 = \sum_j J_{ij} \tag{2.5}$$

and the exchange constant per pair of neighboring atoms J_{ij}.

Curie Temperature at Interfaces and in Thin Layers

By taking a closer look at equation 2.5 it becomes clear that J_0 has to be significantly smaller for atoms sitting at a surface or interface, since about half the neighboring atoms are missing. This directly affects the Curie temperature in the same way, as T_C is proportional to J_0. Thus, it is expected that the T_C is reduced at interfaces and surfaces, which directly results in a reduced saturation magnetization at room temperature. However, interfaces and surfaces in real systems will be a lot more complex since interface roughness and the surrounding chemistry has to be taken into account.

A nice example of an experimental study about reduced magnetization was done by Mauri et al. on the ferromagnetic glass $FeNiB_{0.5}$ [62]. They found a reduced exchange interaction at the surface that also depends critically on the chemistry of the surface which results in a reduced surface magnetization.

In systems of thin magnetic layers, with layer thicknesses of only a few nanometers (only several stacked monolayers), such interfacial effects can become dominant, resulting in reduced Curie temperatures and saturation magnetization of such layers. There has been a variety of extensive studies on the magnetic properties of thin layers and the dependence on thickness and interface chemistry [63–66].

2.2 Magnetic Anisotropy

Magnetic anisotropy is the energy that is related to the rotation of the magnetization direction from an easy to a hard direction. The easy and hard direction of a sample can have its origin in different types of anisotropy, e.g. shape anisotropy, magnetocrystaline anisotropy (MCA), or anisotropy

induced by mechanical strain or stress. Anisotropies lead to favored magnetization axis (i.e. hard and easy axis) along which it is easier to magnetize a sample. Since the magnetization of a sample never has a unique favored direction, but rather a favored axis the anisotropy energy E_{ani} has to stay the same when the magnetization direction is switched. E_{ani} can be expanded by the following equation [56]:

$$E_{\mathrm{ani}} = K_1 \sin^2\gamma + K_2 \sin^4\gamma + K_3 \sin^6\gamma + ... \tag{2.6}$$

with the anisotropy constants K_i, and the angle γ between the magnetization and a characteristic axis that fits the geometry of the sample (for thin films the surface normal is usually chosen as axis). Different anisotropy contributions within a given sample just add up.

In the following the origin of the anisotropies that are most important in thin layered samples, namely shape anisotropy and the MCA, will be shortly summarized.

Shape Anisotropy

The stray field, generated by the magnetization of a sample, tends to demagnetize the sample. Outside of a sample the stray field is given by $\vec{H}_{\mathrm{S}} = \vec{B}/\mu_0$ and inside the sample it is often called the demagnetizing field H_d and is given by [56]

$$\vec{H}_{\mathrm{D}} = \frac{1}{\mu_0}(\vec{B} - \vec{M}), \tag{2.7}$$

with the vacuum magnetic permeability μ_0, the magnetization $\vec{M}$, and the magnetic induction $\vec{B}$. The energy E_{D} stored in this field can be calculated via the following integral over the sample volume [56]

$$E_{\mathrm{D}} = \int_V \vec{H}_{\mathrm{D}}\vec{M}dV. \tag{2.8}$$

For a sample with an arbitrary shape, this term leads to favorable and unfavorable directions of the magnetization (i.e the shape anisotropy). For arbitrary shaped samples, there is no analytical solution for this, however there are solutions for example for ellipsoidal samples [67] or thin films [56] and also approximations for rectangular rods and cylinders [68]. For thin layers the stray field energy is minimized for an in-plane magnetization and the energy difference between out-of-plane and in-plane

Magnetocrystalline Anisotropy

The magnetocrystaline anisotropy (MCA) arises from the spin-orbit interaction, that couples the spin magnetic moment to the orbital magnetic moment, which tries to minimize its energy by its orientation with respect to the crystal lattice. In a intuitive picture one can imagine that the electronic wave functions and the corresponding orbital moment lock into preferred directions within the crystal in order to reduce the interaction with electrons of neighboring atoms. Since the spin-orbit interaction couples the spin and orbital moments this leads to the coupling of the isotropic spin moments to the lattice, resulting in favorable and unfavorable (or easy and hard) axis for the magnetization direction. Depending on the symmetry of the lattice there can be a single easy axis, multiple easy axis, or easy planes within the crystal. However, this simplified picture only gives an intuitive approach to MCA, for an actual description, one would need to calculate the spin-orbit energy along different crystallographic directions by taking into account the geometry of the lattice and the resulting crystal fields. The energy difference of the spin-orbit energy ΔE_{SO} between the magnetization being aligned with the hard axis and easy axis is the MCA [56]:

$$\Delta E_{\mathrm{SO}} = \langle H_{\mathrm{SO}} \rangle_{\mathrm{hard}} - \langle H_{\mathrm{SO}} \rangle_{\mathrm{easy}} = \zeta [\langle \vec{L} \cdot \vec{S} \rangle_{\mathrm{hard}} - \langle \vec{L} \cdot \vec{S} \rangle_{\mathrm{easy}}] > 0, \quad (2.9)$$

with the spin-orbit coupling constant ζ. Bruno developed a model in 1989 where he directly relates the anisotropy of the spin orbit energy with the anisotropy of the projected orbital magnetic moment, suggesting that the orbital moment along the easy axis $m_{\mathrm{O}}^{\mathrm{easy}}$ is larger than the one along the hard axis $m_{\mathrm{O}}^{\mathrm{hard}}$ [56,69]:

$$\Delta E_{\mathrm{SO}} = \zeta[\langle \vec{L} \cdot \vec{S} \rangle_{\mathrm{hard}} - \langle \vec{L} \cdot \vec{S} \rangle_{\mathrm{easy}}] = \frac{\zeta}{4\mu_{\mathrm{B}}}(m_{\mathrm{O}}^{\mathrm{easy}} - m_{\mathrm{O}}^{\mathrm{hard}}) > 0. \quad (2.10)$$

This relation has been experimentally observed, for example via angle dependent XMCD measurements by Weller et al. on a Co wedge that was sandwiched between Au [70], or by Goering et al. on epitaxial CrO_2 films [71]. It is obvious that the MCA at a surface has to be substantially different than that in bulk, since the symmetry of the lattice is broken at a surface. This can lead to a perpendicular magnetic anisotropy at the surface, which can even overcome the shape anisotropy and result in a preferred magnetization direction perpendicular to the surface in ultra thin films [72,73].

Experimental Part I

Chapter 3

Magnetic and Non-Magnetic Resonant X-Ray Optical Parameter

3.1 Introduction

In XRR and XRMR experiments x-rays are reflected at layered systems and the intensity is measured. The x-ray optical properties of the different layers determine how much intensity is reflected and transmitted at each interface. In order to simulate XRR and XRMR measurement data those optical properties need to be known. For photon energies far away from resonant edges (like the TMs L-edges or O K-edge) they are tabulated for example in [74] or [75]. However, the exact optical properties in resonant conditions are not tabulated, but can be measured via e.g. XAS.

XAS measurements yield information about unpopulated electronic states of an atom and the photon energy of the used x-rays determines the specific element to which the measurement is sensitive [76]. Thus, with

XAS the local geometry and the chemical environment of atoms within a sample can be studied. Electron energy loss spectroscopy (EELS) experiments contain the almost the same information as XAS spectra but are measured with electrons in TEM experiments [77,78].

Since XAS probes unpopulated states, the white line intensity (see for example Fig. 3.3) of TM L-edges is proportional to the number of 3d holes [56,79]. Another information that can be retrieved from XAS measurements is the oxidation state of a metal ion within an oxide, since the energy position of the resonant edges in metals tend to shift towards higher energies with increasing oxidation state [80]. This has been shown in multiple studies for example for Mn oxides [81–84], for Fe oxides [82–84], for V oxides [83], for Cr oxides [84] and for Ni oxides [85–87]. XAS measurements at the O K-edge of metal oxides often show a complex spectrum with multiple distinct peaks. The O K-edge spectra vary dramatically for different metals as well as for different oxidation states of the same metal [83,87–89]. Nevertheless, it is often possible to attribute different peaks directly to specific unpopulated states of the oxide [89]. By using circular instead of linear polarized x-ray, XMCD measurements are possible, which yield information about the magnetic properties of an atom, and the spin and orbital magnetic moments can be disentangled quantitatively and element-specifically [90–94].

In this chapter, XAS and XMCD measurements at the $L_{2,3}$-edge of Cr, Fe, Co, and Ni and at the K-edge of O are shown and the x-ray optical properties are retrieved from those measurements. A schematic of the sample design for those measurements is shown in Fig. 3.1. Those elements are chosen for the measurements because they will build up the layers of the samples for the XRR, XRMR, and VXRR measurements in the chapters 4 and 5. Thus, the exact x-ray optical properties at the corresponding resonant edges for those elements need to be known in order to simulate measured reflection data later. The resonant x-ray optical

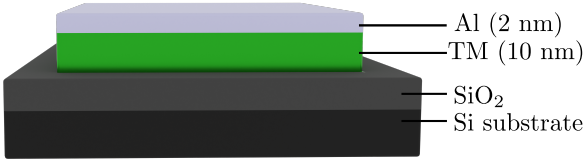

Figure 3.1: Schematic of the sample design for XAS and XMCD measurements throughout this chapter. The Al layer on top is for oxidization protection.

properties should always be measured during the same beamtime as the corresponding reflectometry measurements, and no literature data can be used, since the energy resolution and energy offset of the beamline during the beamtime need to be know. Before the experimental results are presented, the basic principles of XAS and XMCD are briefly explained, how the x-ray optical properties can be retrieved from the measurements, and the measurement procedure itself is outlined.

3.2 Experimental Methods

This section gives an overview of the methods and corresponding theory that are necessary to obtain magnetic and non-magnetic resonant x-ray optical properties. The experimental techniques of XAS and XMCD are described and a brief introduction to the underlying theory is given. The connection between these measurement techniques and x-ray optical properties is explained. The introductions in this section follow the explanations given by Stöhr et al. in [56].

3.2.1 X-Ray Absorption Spectroscopy

Measuring the effect of the interaction of x-rays with condensed matter can yields information about chemical and structural properties of a sample. In XAS experiments, x-rays are shot onto a sample where they are absorbed and cause excitation or ejection of core electrons and the intensity reduction (i.e. absorption) of x-rays is measured. The used x-rays can be loosely divided into soft (from 250 eV to about 1 – 3 keV) and hard x-rays (about 3 – 20 keV) [95,96]. The energy range interesting for this work is in the soft x-ray regime, as the studied TM L-edges and the O K-edge are between 543 eV and 870 eV [97]. Figure 3.2 shows an exemplary XAS measurement showing three distinct absorption edges. An absorption edge is a sharp rise in absorption and it occurs at energies were photons before the edge do not have enough energy to excite electrons from a particular core level, while above the edge the photons have enough energy for that excitation. The absorption edges are named corresponding to the principal quantum number of the state the excited electron initially populates. For an electron initially in a state of principal quantum number $n = 1$ the edge is called a K-edge, for $n = 2$ a L-edge, for $n = 3$ a M-edge, and so forth.

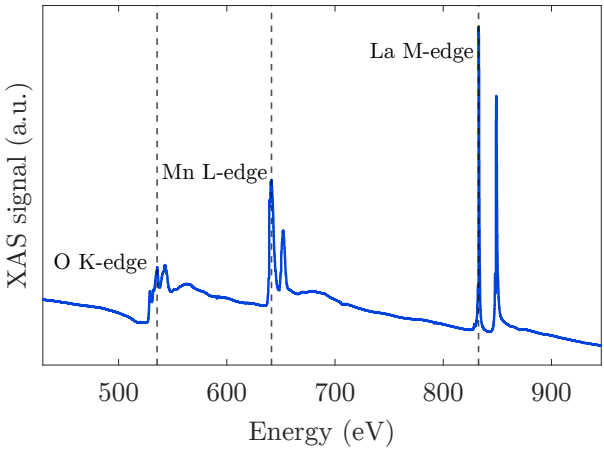

Figure 3.2: An exemplary overview XAS measurement between 430 eV and 940 eV of a sample that contains O, Mn, and La.

Each element has its absorption edges at characteristic energies that are tabulated for example in [97], thus XAS measurements are element sensitive. From the edges visible in Fig. 3.2 one can conclude that the studied sample contains O, Mn, and La.

In order to describe XAS on a quantum mechanical basis, one has to calculate the transition probability per unit time T_{if} between a initial state $|i\rangle$ and a final state $|f\rangle$. The transition probability T_{if} is calculated by *Fermi's golden rule*[56]

$$T_{if} = \frac{2\pi}{\hbar} |\langle f| \mathcal{H}_{\text{int}} |i\rangle|^2 \delta(\epsilon_i - \epsilon_f) \rho(\epsilon_f), \tag{3.1}$$

with interaction Hamiltonian $\mathcal{H}_{\text{int}}$, the energy of the initial and final state ϵ_i and ϵ_f, respectively, the density of final states per unit energy $\rho(\epsilon_f)$, and the Dirac delta function δ.

For 3d TMs, the integrated intensity of the L-edge is directly propor-

tional to the number of unpopulated 3d states, i.e. the number of 3d holes n_{h} [56,79]. L-edge spectra for the TMs Fe, Co, Ni, and Cu are shown in Fig. 3.3(a). The intensity of the resonant edge decreases drastically when going from Fe to Cu because the filling of the 3d states along this series. By integrating over the unpopulated part of the density 3d states $\rho_{3d}(E)$ (see Fig. 3.3(b)) one can obtain the theoretical number of 3d holes $n_{\mathrm{h}} = \int_{E_{\mathrm{F}}}^{\infty} \rho_{3d}(E)dE$. In Fig. 3.3(c) the intensity of the resonance edges of Fe, Co, Ni, and Cu is plotted against the theoretical number of 3d holes and shows a linear relationship.

There are several experimental methods available to measure XAS data. In transmission experiments the initial x-ray intensity is compared to the intensity after the x-rays pass through a thin sample (see Fig. 3.4(a)). Another way is to measure the total number of electrons that are ejected from a sample by the incoming x-rays, this measurement technique is called total electron yield (TEY) and is depicted in Fig. 3.4(b). The total electron yield (TEY) measurement mode is used for the XAS measurements in this chapter. A third possible technique to measure XAS is to detect the number of fluorescence photons that are emitted after electron from an outer shell drops into a core hole. This measurement technique is called total fluorescence yield (TFY).

More details about XAS can be found in [56,76,98,99].

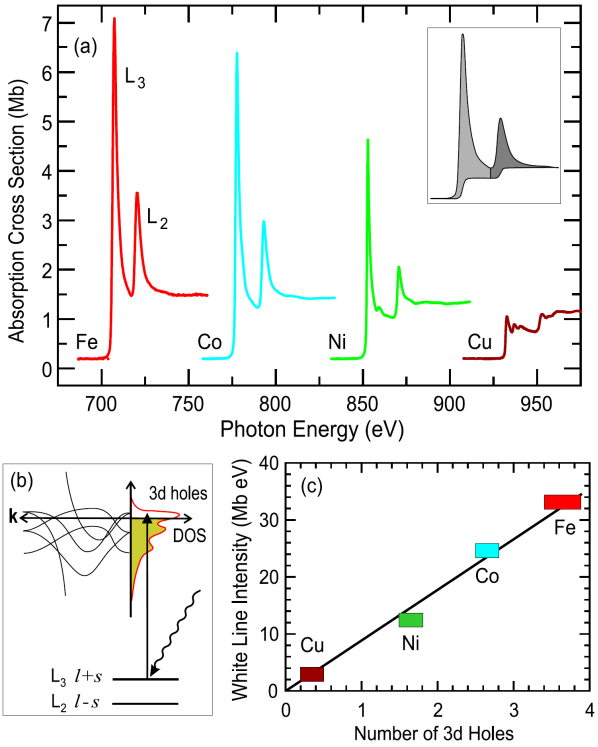

Figure 3.3: (a) L-edge XAS measurements for the TMs Fe, Co, Ni, and Cu. The inset depicts how the intensity of the spectra is obtained from the area. (b) The theoretical number of 3d holes can be derived by integrating over the 3d density of states above the Fermi energy. (c) Linear relationship between theoretical obtained number of 3d holes and the L-edge intensity. The figure is taken from [56].

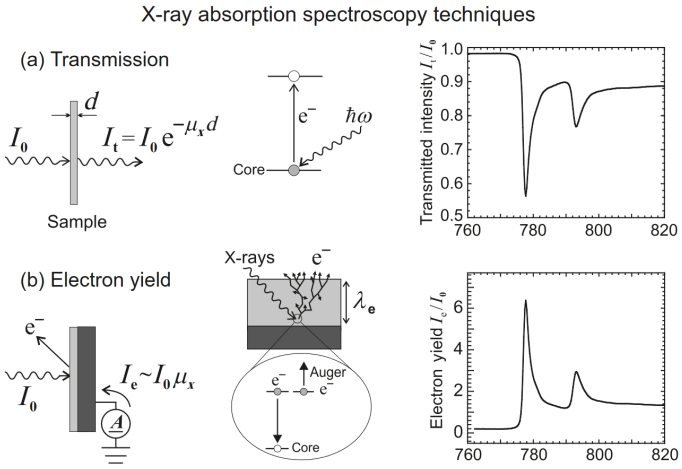

Figure 3.4: (a) Typical geometry for XAS experiments in transmission mode. A core electron is excited by the x-ray that pass through the sample, thus the x-ray intensity after passing through the sample is reduced. The ratio between transmitted and initial intensity for a 10 nm thick Co layer is plotted on the right. (b) Illustration of the principles of measuring XAS in TEY mode. An x-ray photon excites a core electron, the corresponding hole is filled by an outer electron and an Auger electron is emitted. On its way to the surface, a low energy cascade is induced by the primary Auger electron. The number of emitted electrons is proportional to the absorption probability. The TEY signal is measured with an ammeter, that measures the current that flows back to the sample from ground. On the right is a typical XAS measurement in TEY mode, measured at a Co sample. This figure is taken from [56].

3.2.2 X-Ray Magnetic Circular Dichroism

The intensity of 3d TM L-edge spectra is proportional to the number of 3d holes, as described above. If the absorption process would additionally be spin dependent the number of spin-up and spin-down 3d holes could be measured, which would be proportional to the magnetic moment of a sample. With circular polarized x-rays it is indeed possible to measure spin dependent x-ray absorption and the effect is called x-ray magnetic circular dichroism (XMCD).

One of the first experimental realizations to measure the XMCD effect was done by Schütz et al. in 1987 at the Fe K-edge[90]. Since then the XMCD effect has become an integral part of magnetic research. With XMCD measurements, the uncompensated magnetic moments of a magnetic compound can be element specifically determined. Furthermore, the so called *Sum Rules* allow to separately determine the atomic orbital and spin magnetic moment from the intensities of a XMCD spectrum[56,93,94]. In this thesis, the XMCD effect is mainly used to change the optical properties of buried magnetic layers which allows to determine magnetic depth profiles from XRMR measurements (see chapter 4). Which is why only a short introduction to the principles of the XMCD effect is given here, for further details see [56,100,101].

Circular polarized photons carry an angular momentum L_{Ph} which has an opposing sign for opposing helicities (i.e. right and left hand circular polarized photons) and points either parallel or antiparallel to the direction of propagation (i.e. the wave vector $\mathbf{k}$). The XMCD effect can now be described in a two-step model. In the first step a circular polarized photon is absorbed and excites an electron. Since the angular momentum has to be conserved it is transferred to the electron, resulting in excitation of spin polarized electrons. In the second step the unoccupied 3d spin-up and spin-down states, which are shifted with respect to each other

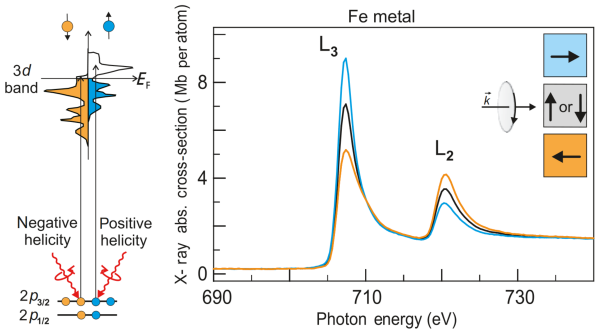

Figure 3.5: Schematic illustration of the XMCD effect, exemplarily shown for absorption at the Fe L-edge. On the left, the density of states for spin up and spin down (shifted with respect to each other by exchange splitting) in Fe is shown and the excitation of 2p core electrons by circular polarized x-rays is depicted. On the right, the corresponding absorption spectrum for parallel (blue), antiparallel (orange) and perpendicular (black) alignment of photon helicity and sample magnetization is shown. The figure is taken from [56].

in energy by exchange splitting, act as detector for the spin polarized excited electrons. This process is schematically illustrated in the left of Fig. 3.5. Measuring now the x-ray absorption with parallel and antiparallel orientation of photon helicity and sample magnetization results in different intensities. The XMCD intensity ΔI is defined as:

$$\Delta I = I^{\uparrow\downarrow} - I^{\uparrow\uparrow} \propto \mu^{\uparrow\downarrow} - \mu^{\uparrow\uparrow}, \tag{3.2}$$

with the XAS intensities $I^{\uparrow\uparrow}$ and $I^{\uparrow\downarrow}$ and the x-ray absorption coefficients $\mu^{\uparrow\uparrow}$ and $\mu^{\uparrow\downarrow}$ for parallel and antiparallel alignment, respectively. An example for XAS intensities with parallel and antiparallel orientation is shown on the right of Fig. 3.5 at the L-edge of an Fe sample. As described above, the absorption of x-rays depends on the angular momentum L_{Ph} of the photons and the unequal population of 3d states with spin-up and spin-down (which defines the magnetic moment m) in a sample. Thus the

XMCD intensity is proportional to the dot product of L_{Ph} and m:

$$\Delta I \propto \mathbf{L}_{\mathrm{Ph}} \cdot \mathbf{m}. \tag{3.3}$$

The maximum XMCD effect is obtained for a collinear orientation of L_{Ph} and m. In order to measure $I^{\uparrow\uparrow}$ and $I^{\uparrow\downarrow}$ either the photon helicity or the direction of the magnetization has to be switched.

3.2.3 X-Ray Optical Properties

In order to describe the propagation of x-rays through a material, the complex index of refraction $n(\omega)$ is used [56]:

$$n(\omega) = 1 - \delta(\omega) + i\beta(\omega), \tag{3.4}$$

where the real and imaginary components $\delta(\omega)$ and $\beta(\omega)$ describe the frequency ω dependent refraction and absorption of a material, respectively. The index of refraction $n(\omega)$ describes the optical properties of a material as a whole, i.e. in a macroscopic manner. The material can be build up of any kind of mixture of elements, $n(\omega)$ describes the average optical properties. In order to describe and understand the processes in x-ray scattering on an atomic level, a more suitable description of the optical properties is based on the complex atomic scattering factor [56]:

$$F(\mathbf{Q}, \omega) = F^0(\mathbf{Q}) + F'(\omega) - iF''(\omega), \tag{3.5}$$

where $\mathbf{Q}$ is the momentum transfer in the scattering process and $F^0(\mathbf{Q})$ the atomic form factor. In the soft x-ray regime $F^0(\mathbf{Q}) \approx Z$ with the total number of electrons in an atom Z, thus equation 3.5 changes to:

$$F(\omega) = Z + F'(\omega) - iF''(\omega) = f_1(\omega) - if_2(\omega), \tag{3.6}$$

with the Henke-Gullikson atomic factors $f_1(\omega) = Z + F'(\omega)$ and $f_2 = F''(\omega)$, which are tabulated and can be readily used for frequencies far away from resonances[74,75]. The atomic scattering $F(\omega)$ and the index of refraction $n(\omega)$ are related via:

$$1 - n(\omega) = \frac{r_0 \lambda^2}{2\pi} \sum_j \rho_j F_j(\omega), \tag{3.7}$$

with the classical electron radius r_0, the wavelength λ of the incident x-rays, and the number density ρ_j of the atomic species j. The sum $\sum_j$ runs over all atomic species that are present in the material. For a hypothetical material that consists only of one atomic species, equation 3.7 can be simplified and one obtains the following relations between $\delta(\omega)$ and $f_1(\omega)$ and between $\beta(\omega)$ and $f_2(\omega)$:

$$\delta(\omega) = \frac{\rho_\mathrm{a} r_0 \lambda^2}{2\pi} f_1(\omega) \tag{3.8}$$

$$\beta(\omega) = \frac{\rho_\mathrm{a} r_0 \lambda^2}{2\pi} f_2(\omega), \tag{3.9}$$

with the density ρ_a of the atomic species.

For frequencies close to a resonance the tabulated values for $f_1(\omega)$ and $f_2(\omega)$ can not be used since there the interaction of x-rays with matter is dominated by excitations of core electrons to unpopulated valence states. Thus, the fine structure of the resonance reflects the local environment of the interacting atom. Because of that the atomic factors close to a resonance needs to be determined experimentally. The so called *optical theorem* links the photon energy dependent ($E = \hbar\omega$) x-ray absorption cross section $\sigma^{\mathrm{abs}}(E)$, that can be measured with XAS measurements, to the imaginary part of the scattering factor $f_2(E)$ via[35,56,102]

$$\sigma^{\mathrm{abs}}(E) = \frac{2hcr_0}{E} f_2(E). \tag{3.10}$$

Here h is the Planck constant and c the speed of light. The *optical theorem* is only valid for long wavelengths compared to typical atom sizes which is the case in the soft x-ray regime. Thus, it is possible to obtain $f_2(E)$ from soft x-ray XAS measurements. The procedure how to obtain $f_2(E)$ from experimental data is explained in section 3.3. The Kramers-Kronig relation can now be used to obtain $f_1(E)$, after $f_2(E)$ is determined from experimental data. The equation for $f_1(E)$ is given by [56]:

$$f_1(E) = Z + \frac{2}{\pi} PV \int_0^\infty \frac{\epsilon f_2(E)}{E^2 - \epsilon^2} d\epsilon. \tag{3.11}$$

where PV denotes the Cauchy principle value.

The *optical theorem* also extends to the magnetic component of the x-ray optical properties, thus $\Delta f_2^{\mathrm{mag}}$ can be determined from XMCD measurements the same way as f_2 from XAS measurements. And $\Delta f_2^{\mathrm{mag}}$ can be derived from $\Delta f_2^{\mathrm{mag}}$ via Kramers-Kronig relation (see equation 3.11 with $Z = 0$) [56].

For more information about x-ray optical properties and their theoretical derivation see for example [56].

3.2.4 XAS Measurements with ERNSt

The XAS measurements are performed in TEY mode with Stuttgart Novel Reflectometer Experiment (ERNSt) [103] (the experimental setup is shown in Figs. 4.4 and 4.5). In order to optimize the current signal and to reduce the impact of electrons based on stray light, a bias voltage of $-40\,\mathrm{V}$ is applied to the sample holder and a magnetic field of 117 mT at an angle of 30° with respect to the sample surface is applied. The angle of the magnetic field and the offset voltage send the electrons that are emitted from the sample on a spiral path away from the sample. The incoming

x-ray intensity I_0, that is needed to normalize the measured TEY signal, is measured via a gold mesh [103]. The integration time for a single data point is set to 1500 ms. For magnetic samples the energy is scanned over the respective resonance edge and the TEY signal is measured for both, parallel and antiparallel, alignment of sample magnetization and photon helicity. A *Keithley 6517B Electrometer* is used to measure the TEY signal.

3.3 XAS and XMCD Measurements – Retrieving Resonant X-Ray Optical Parameter

3.3.1 Procedure for Retrieving Optical Parameter

The procedure that is needed to retrieve x-ray optical parameters from XAS measurements is shown in Fig. 3.6 and is also explained in [35]. The first step is to normalize the raw TEY data with the simultaneously measured incoming x-ray intensity I_0. If the two spectra measured with parallel and antiparallel configuration of sample magnetization and photon helicity do not lie on top of each other in the region before and after the edge, one of the spectra should be multiplied with an appropriate factor that brings them on top of each other [104]. Next, a straight line is fitted to the linear region before the edge. That straight line is then subtracted from the normalized XAS data and the data is divided by the edge jump h_{exp}, which is the difference between the line and the data after the edge. This results in so called edge normalized data, which has a value of 0 before the edge and a value of 1 after the edge. The next step is, to fit a straight line to the pre-edge region of the tabulated f_2 values [74,75] and determine the edge jump of the tabulated data h_{lit} at the same energy as h_{exp} was determined. The edge normalized measurement data are then multiplied with h_{lit} and the fitted straight line from the tabulated data is added to them. This already results in the imaginary part of the atomic scattering factor for parallel and antiparallel configuration of sample magnetization and photon helicity $f_2^{\uparrow\uparrow}$ and $f_2^{\uparrow\downarrow}$. In order to obtain the non magnetic (polarization averaged) atomic scattering factor f_2, the average of $f_2^{\uparrow\uparrow}$ and

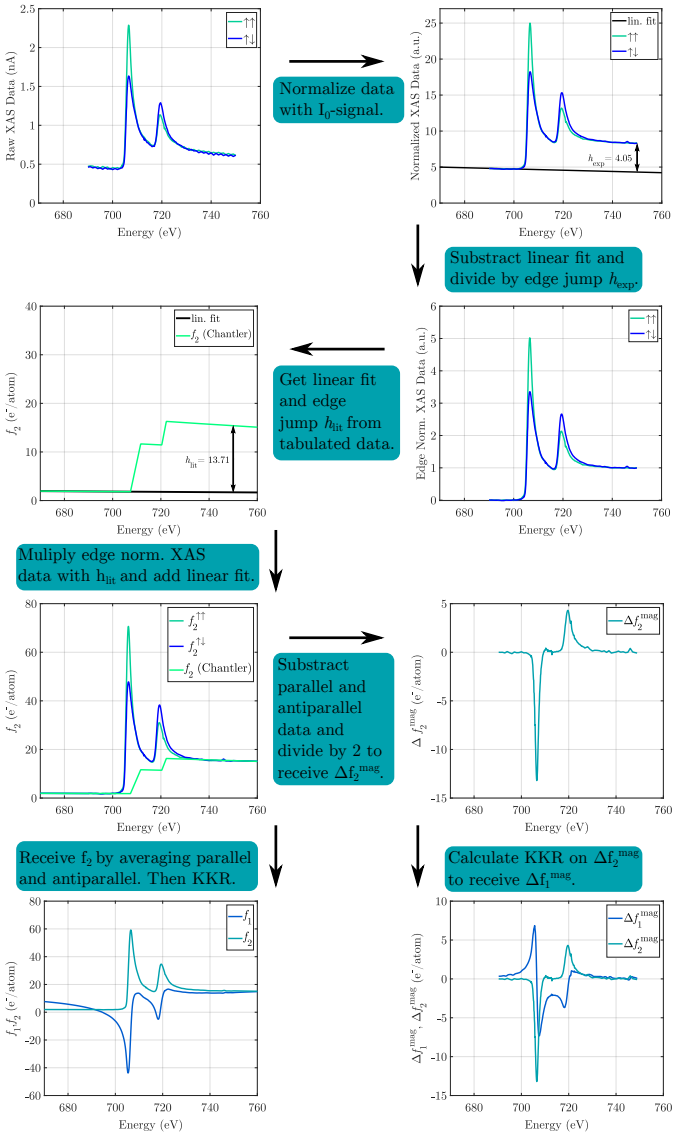

Figure 3.6: Procedure to retrieve x-ray optical parameters from XAS measurements exemplarily shown on basis of data measured at the Fe L-edge.

$f_2^{\uparrow\downarrow}$ has to be calculated:

$$f_2 = \frac{f_2^{\uparrow\uparrow} + f_2^{\uparrow\downarrow}}{2}. \tag{3.12}$$

And the real part of the x-ray optical properties f_1 is obtained by applying Kramers-Kronig relation (see equation. 3.11) to f_2.

The imaginary part of the magnetic component of the x-ray optical properties $\Delta f_2^{\mathrm{mag}}$ is retrieved by

$$\Delta f_2^{\mathrm{mag}} = \frac{f_2^{\uparrow\downarrow} - f_2^{\uparrow\uparrow}}{2 \cdot \cos 30^\circ}, \tag{3.13}$$

where the $\cos 30^\circ$ is needed because the sample is tilted by 30° with respect to the incoming x-ray beam and the applied magnetic field, but the magnetization of it stays in plane because of the high shape anisotropy of thin films. The real part $\Delta f_1^{\mathrm{mag}}$ is again calculated by applying Kramers-Kronig relation to $\Delta f_2^{\mathrm{mag}}$ (see equation 3.11).

3.3.2 Measurement Results for Optical Parameter

The measurement results for the resonant x-ray optical parameters of Fe, Co, Ni and Cr at the L_3-edge and for O at the K-edge obtained by the above procedure are presented below.

Iron

Figure 3.7 shows the x-ray optical properties f_1, f_2, $\Delta f_1^{\mathrm{mag}}$ and $\Delta f_2^{\mathrm{mag}}$ of Fe at the L-edge. The data was measured on a sample that was designed as shown in Fig. 3.1 with a 10 nm thick Fe layer and a 2 nm thick Al capping to protect the Fe from oxidation. The optical properties follow the course of a typical metallic Fe L_2 and L_3-edge spectrum (compare for example spectra shown in [92,105,106]). The maximum of f_2 and $\Delta f_2^{\mathrm{mag}}$ is at a photon energy of 706.2 eV.

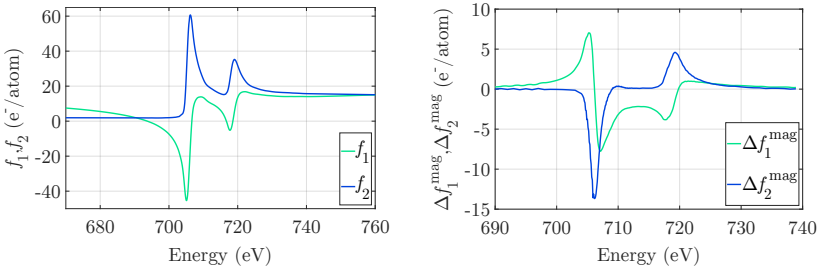

(a) **(b)**

Figure 3.7: (a) f_1 and f_2, the real and imaginary component of the atomic scattering factor of Fe at the L_2 and L_3-edge. (b) $\Delta f_1^{\mathrm{mag}}$ and $\Delta f_2^{\mathrm{mag}}$, the real and imaginary component of the magnetic part of the atomic scattering factor of Fe at the L_2 and L_3-edge.

Cobalt

Figure 3.8 shows the x-ray optical properties f_1, f_2, $\Delta f_1^{\mathrm{mag}}$ and $\Delta f_2^{\mathrm{mag}}$ of Co at the L-edge. The data was measured on a sample that was designed as shown in Fig. 3.1 with a 10 nm thick Co layer and a 2 nm thick Al capping to protect the Co from oxidation. The optical properties follow the course of a typical metallic Co L_2 and L_3-edge spectrum (compare for example spectra shown in [92,107]). The maximum of f_2 and $\Delta f_2^{\mathrm{mag}}$ is at a photon energy of 777 eV.

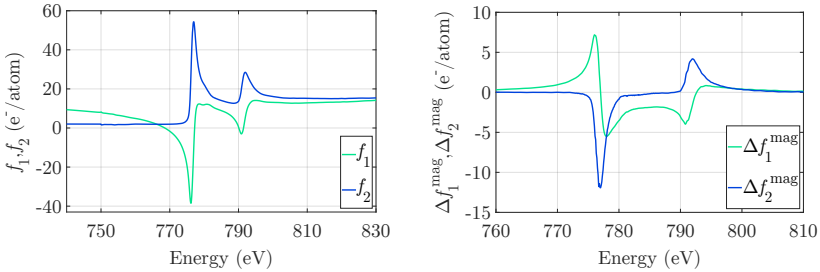

(a) **(b)**

Figure 3.8: (a) f_1 and f_2, the real and imaginary component of the atomic scattering factor of Co at the L_2 and L_3-edge. (b) $\Delta f_1^{\mathrm{mag}}$ and $\Delta f_2^{\mathrm{mag}}$, the real and imaginary component of the magnetic part of the atomic scattering factor of Co at the L_2 and L_3-edge.

Nickel

Figure 3.9 shows the x-ray optical properties f_1, f_2, $\Delta f_1^{\mathrm{mag}}$ and $\Delta f_2^{\mathrm{mag}}$ of Ni at the L-edge. The data was measured on a sample that was designed as shown in Fig. 3.1 with a 10 nm thick Ni layer and a 2 nm thick Al capping to protect the Ni from oxidation. The optical properties follow the course of a typical metallic Ni L_2 and L_3-edge spectrum (compare for example

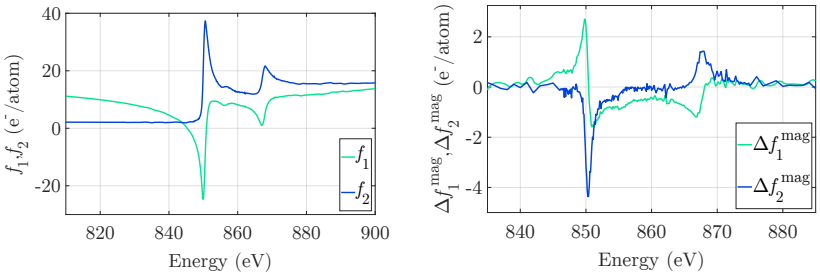

(a) **(b)**

Figure 3.9: (a) f_1 and f_2, the real and imaginary component of the atomic scattering factor of Ni at the L_2 and L_3-edge. (b) Δf_1^{mag} and Δf_2^{mag}, the real and imaginary component of the magnetic part of the atomic scattering factor of Ni at the L_2 and L_3-edge.

spectra shown in [91,108]). The maximum of f_2 and Δf_2^{mag} is at a photon energy of 850.6 eV and 850.3 eV, respectively.

Chromium

Figure 3.10 shows the x-ray optical properties f_1 and f_2 of Cr at the L-edge. The data was measured on a sample that was designed as shown in Fig. 3.1 with a 10 nm thick Cr layer and a 2 nm thick Al capping to protect the Cr from oxidation. The optical properties follow the course of a typical metallic Cr L_2 and L_3-edge spectrum (compare for example spectra shown in [109,110]). The maximum of f_2 is at a photon energy of 575.4 eV.

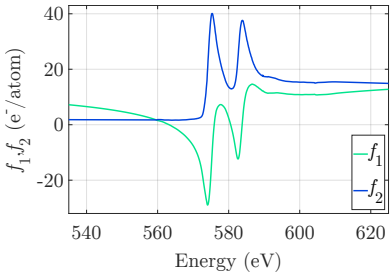

Figure 3.10: f_1 and f_2, the real and imaginary component of the atomic scattering factor of Cr at the L_2 and L_3-edge.

Oxygen

Figure 3.11 shows the x-ray optical properties f_1 and f_2 of Cr at the L-edge. The data was measured on a blank substrate, that consists of Si capped with a 50 nm layer of thermally oxidized SiO_2. The optical properties follow a similar course than O K-edge spectra measured at SiO_2 samples in the literature (compare for example with [48,111]).

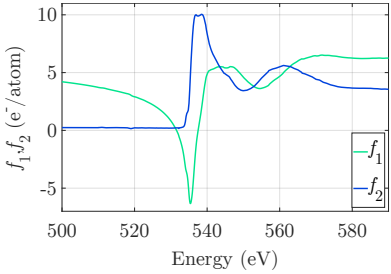

Figure 3.11: f_1 and f_2, the real and imaginary component of the atomic scattering factor of O at the O K-edge.

3.4 Summary

In this chapter the x-ray optical properties f_1 and f_2 of Cr, Fe, Co, and Ni at the L-edge and of O at the K-edge were retrieved from XAS measurements. For Fe, Co, and Ni also the magnetic component of the x-ray optical properties $\Delta f_1^{\mathrm{mag}}$ and $\Delta f_2^{\mathrm{mag}}$ were obtained from XMCD measurements. Comparing the measured spectra to spectra from literature showed that they are in good quantitative agreement. The x-ray optical properties of those elements are needed for the following chapters, where XRR, XRMR, VXRR measurements are performed on layered samples, build up of those elements. To obtain physically meaningful results from reflectometry measurements, the data must be compared with simulations. For those simulations the exact x-ray optical properties must be known.

Experimental Part II

Chapter 4

Reduced Thin Layer Magnetizations

In this chapter different interfacial effects of reduced thin layer magnetization in multilayered systems are analyzed. Chemical and magnetic depth profiles are retrieved by means of XRR and XRMR. Together with magnetometry measurements the origin of reduced thin layer magnetization is studied in detail.

The introduction of the chapter explains the interest of current research in thin film magnetism and its importance for modern technology. The experimental methods and aspects of data processing used to obtain the presented results are then introduced. XRR and XRMR measurements with the resulting chemical and magnetic depth profiles are shown and additional magnetometry measurements are presented. At the end of the chapter the results are discussed and conclusions are drawn.

4.1 Introduction

Multilayer systems with thin magnetic films ranging from a few atomic layers to several nanometers are ubiquitous in the field of magnetism and spintronics. For example magnetic sensors and hard disk read heads are build up of a multilayered thin film stacks and exploit the GMR or TMR effect. New data storage concepts like MRAMs are build up of multiple thin layers including MTJs[17,25,112,113]. Thin magnetic layers also appear in magnonics[114–116], are used for spin Hall nano-oscillators[21,117], or build up systems with perpendicular magnetic anisotropy (PMA) and VCMA[113,118,119]. In order to optimize and fine tune the functionality of such systems, exact knowledge of structural and magnetic properties is necessary. Layer thicknesses, chemical and magnetic depth profiles, interfacial properties such as roughness, intermixing at interfaces, and interfacial magnetism are parameters which strongly influence the functionality. Characteristic physical values as magnetoresistance and spin diffusion lengths are extremely sensitive to these parameters and show large variations throughout literature[27–31]. In devices which utilize STT or SOT the boundary between ferromagnetic and non-ferromagnetic layer is of particular interest[120–122]. For theoretical approaches and simulations, structural and magnetic properties are basic inputs. However, the actual depth dependent element distributions and magnetization profiles are usually unknown and not easily accessible, which makes it harder to perform meaningful simulations of real systems.

Experimental techniques providing detailed information about buried layers are rare. TEM is a common imaging technique yielding depth dependent information with high resolution. TEM is often used in combination with element-specific methods such as energy-dispersive x-ray spectroscopy (EDX) and EELS. A drawback with TEM measurements is, that a lamella of about $10-100\,\mathrm{nm}$ thickness has to be cut out of the layer stack and

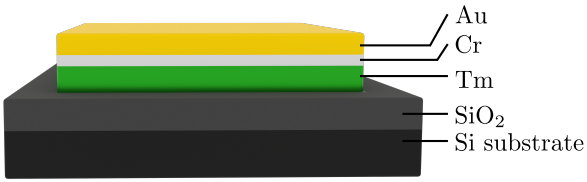

Figure 4.1: Schematic of the sample design for XRR and XRMR measurements throughout this chapter.

the information is restricted to several 10 nm and therefore rather local. Also, obtaining depth dependent magnetic information is not easily possible with TEM. In contrast to this, element-specific chemical and magnetic depth profiles averaged over larger areas of several µm^2 to mm^2 can be obtained with high depth resolution with XRR in combinations with XRMR [33–37]. Additionally, a multilayered sample can be measured without elaborate preparation as long as its lateral dimension is in the range of mm to cm. XRMR measurements have proven to be extremely beneficial in many different experimental studies, e.g. retrieving spatially resolved electronic structures and depth dependent orbital polarization profiles of superlattices [41–44], studying pinned magnetic moments in exchange bias systems [38,123], or for the investigation of the magnetic proximity effect in Pt [33,39,124–127]. The technique is still under constant progress, e.g. XRMR has been advanced recently to study depth dependent magnetization dynamics [128,129].

The depth dependent chemical and magnetic depth profiles of sputtered 2 nm thick TM layers in contact with 50 nm of insulating SiO_2 on one side and 1 nm Cr on the other side are systematically studied in this chapter. Figure 4.1 shows the design of the samples. The investigated magnetic TMs are namely iron, cobalt, and nickel. By means of XRR and XRMR the exact chemical and magnetic depth profiles are deduced and the magnetic properties at the interfaces are studied in particular. The

influence of small structural changes such as roughness and thickness variations induced by the sputtering process on the magnetic properties between otherwise identical samples is revealed. In combination with SQUID measurements, the magnetization reduction of the ferromagnetic TM layers is measured quantitatively and the origin of this reduction is investigated. Whether this is caused by a reduced saturation magnetization due to a lower Curie temperature in thin films, actual magnetic dead layers, reduced magnetization due to intermixing of elements at the interface, or a mixture of all three.

4.2 Experimental Methods

4.2.1 X-Ray Reflectometry

X-ray reflectometry (XRR) is a technique that allows to determine chemical depth profiles of layered samples and is especially sensitive to interfaces. X-rays are transmitted and reflected at each interface of a layered sample, and the partial beams interfere with each other, leading to a complex interference pattern. By simulating these patterns with appropriate software (e.g. *ReMagX* [35,36,130]) detailed structural parameter of the studied sample can be retrieved. The introduction to XRR in this section follows the explanations given by Macke et al. in [35].

Figure 4.2 exemplary shows the scattering geometry for XRR experiments. The scattering plane is defined by the incoming and reflected wave vectors $\vec{k_0}$ and $\vec{k'}$. The momentum transfer in z-direction q_z is given by the absolute value of the difference between $\vec{k'}$ and $\vec{k_0}$:

$$q_z = |\vec{k'} - \vec{k_0}| = 2|\vec{k_0}| \cos\alpha = \frac{4\pi}{\lambda} \cos\alpha = \frac{2E}{\hbar c} \sin\Theta, \tag{4.1}$$

with the photon energy E , the reduced Planck constant $\hbar$, the speed of light c, and the angle of incident Θ. For constructive interference, the optical path difference has to be equal to a multiple integer of the wavelength λ:

$$\Delta s = P(AD) - P(ABC) \cdot n_1 = 2d \cdot \sqrt{n_1^2 - \cos^2\Theta} = m\lambda. \tag{4.2}$$

Since $n_1 \approx 1$ for x-rays this simplifies to

$$\Delta s = 2d \cdot \sin\Theta = 2d \cdot \cos\alpha = m\lambda, \tag{4.3}$$

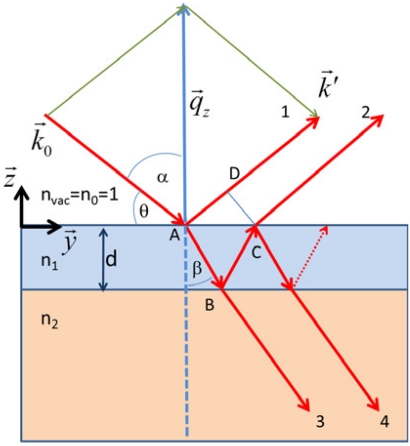

Figure 4.2: Schematic illustration of the scattering plane of a thin film sample with two layers, with index of refraction n_1 and n_2. The thickness of layer 1 is given by d. The momentum transfer $\vec{q_z}$ is given by the difference of the wave vectors of reflected and incoming light $\vec{k'}$ and $\vec{k_0}$. The angle of incidence is given by Θ. Note that the shown refraction depicts the case of visible light entering glass. For x-rays the refraction would be almost not visible and in the opposite direction (i.e. $\beta > \alpha$) because the index of refraction is usually slightly less but very close to 1. The figure is taken from [35].

which is known as the Bragg condition. By replacing $\cos\alpha$ in equation 4.3 with $\cos\alpha = q_z\lambda/(4\pi)$ from equation 4.1 the Laue equation is obtained:

$$q_z = \frac{2\pi}{d}m. \tag{4.4}$$

For simple single film samples the q_z positions of constructive interference can be predicted. Or the other way round, from the periodicity in the interference pattern the layer thickness can be calculated (see for example Fig. 4 in [35]).

Since x-rays are partially transmitted and reflected at each interface of a multilayered sample the intensity of interfering beams is not always

the same. With the Fresnel equations the ratio of transmitted to reflected light at an interface can be calculated. This has to be done separately for light where the electric field vector is parallel (π) and perpendicular (σ) to the scattering plane[35,131]:

$$t_\sigma = \frac{E_t}{E_i} = \frac{2n_1 \cos\alpha}{n_1 \cos\alpha + n_2 \cos\beta} \tag{4.5}$$

$$r_\sigma = \frac{E_r}{E_i} = \frac{n_1 \cos\alpha - n_2 \cos\beta}{n_1 \cos\alpha + n_2 \cos\beta} \tag{4.6}$$

$$t_\pi = \frac{E_t}{E_i} = \frac{2n_1 \cos\alpha}{n_2 \cos\alpha + n_1 \cos\beta} \tag{4.7}$$

$$r_\pi = \frac{E_r}{E_i} = \frac{n_2 \cos\alpha - n_1 \cos\beta}{n_2 \cos\alpha + n_1 \cos\beta}. \tag{4.8}$$

The complex index of refraction in this equations is described by equation 3.4 for x-rays. The resulting numbers for t_σ, r_σ, t_π, and r_π are complex.

However, calculating the reflected intensity at a given q_z only based on the interference and the Fresnel coefficients does usually not result in good agreement with experimental data. There are several reasons for that. As depicted in Fig. 4.2, beams can be reflected multiple times back and forth within one layer resulting in complex interference of many beams. Furthermore, real samples have rough interfaces. Instead of an immediate change from one index of refraction to another one at an interface it usually changes more or less gradually, which strongly reduces the Fresnel coefficients. In addition, the absorption at resonant edges (e.g TM L-edges or O K-edge), which are of interest for this study, can be very high. Thus, the attenuation of light within a layer becomes considerably high. Therefore, the knowledge of the exact resonant optical x-ray properties is necessary, which can be retrieved from XAS measurements (see chapter 3). But all of these issues can be described quantitatively using physical models. For example, interface roughnesses can be determined or the reflection from selected interfaces can be strongly enhanced by tuning the photon energy

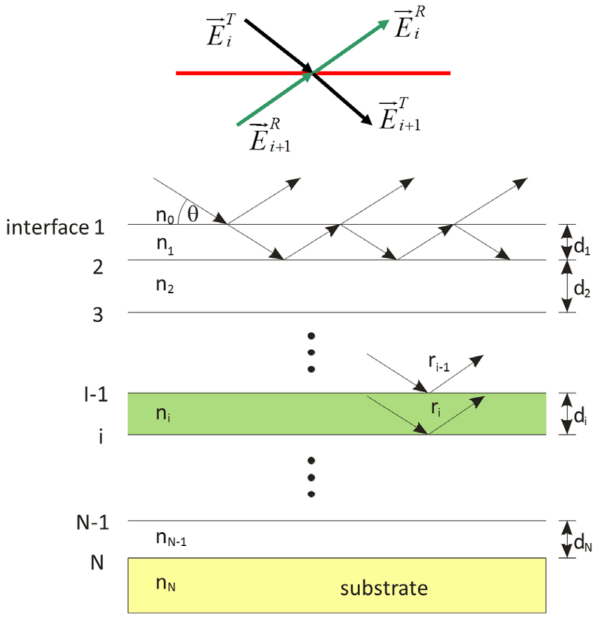

Figure 4.3: Schematic representation of multiple beam reflection in a multilayered sample. The definition of the four partial waves that have to be considered at each interface can be seen at the top. This figure is taken from [35].

to the respective edge which makes the experiment especially sensitive to that interface.

The issue of multiple beam reflection can be dealt with by solving a recursive formalism that was introduced by Parratt in 1954 [132]. The basic idea of this formalism is depicted in Fig. 4.3. At each interface i and for every light polarization, four partial waves have to be taken into account, namely two waves traveling towards the interface from above and below ($\vec{E}_i^T$ and $\vec{E}_{i+1}^R$) and two waves going away from the interface towards the top and bottom of the sample ($\vec{E}_i^R$ and $\vec{E}_{i+1}^T$). The complex amplitudes

of these partial waves have to fulfill the following continuity conditions:

$$E_i^R e^{ik_i z} = r \cdot E_i^T e^{-ik_i z} + (1-r) \cdot E_{i+1}^R e^{ik_{i+1} z}, \tag{4.9}$$

$$E_{i+1}^T e^{-ik_{i+1} z} = -r \cdot E_{i+1}^R e^{ik_{i+1} z} + (1+r) \cdot E_i^T e^{-ik_i z}, \tag{4.10}$$

where i is the index of the layer, r is the reflectivity of one light beam at an interface as defined by the Fresnel equations, k_i are the normal component of the wave vector within the respective layer, and z is depth of the respective interface. The ratio of the amplitudes of all partial waves that are transmitted and reflected at an interface is now defined by

$$R_i = \frac{E_i^R}{E_i^T}. \tag{4.11}$$

With this the above equation can be rewritten to:

$$R_i = \frac{r_i + R_{i+1} e^{2ik_{i+1} d_{i+1}}}{1 + r_i R_{i+1} e^{2ik_{i+1} d_{i+1}}}, \tag{4.12}$$

where d_i is the thicknesses of the respective layer. This equation can be solved recursively, starting at the lowest interface N under the assumption that no light is injected from the substrate that is assumed to be infinitely thick (i.e. $R_N = r_N$). Following this way, the complex ratio R_i of incoming and reflected wave can be calculated step by step for each interface. This has to be done separately for π and σ polarized light. The total reflected intensity, that will be measured in the experiment, is then given by:

$$\frac{I_R}{I_0} = |R_0|. \tag{4.13}$$

This method provides a fast way to calculate the reflected x-ray intensity at multilayered systems.

So far the interfaces are treated without any roughness property. But real systems will have rough interfaces, which strongly reduces the reflec-

tivity. Macke et al. show an example of how much an interface roughness of 1 nm in a sample with a 20 nm thick Fe layer changes the reflected intensity (see Fig. 7 of [35]). The intensity for the rough interface drops a lot faster with increasing q_z and the interference pattern changes. This example shows that it is indispensable to properly describe the interface roughness in the model, otherwise it is not possible to provide a reasonable model for given experimental data. The roughness can be described by an error function shaped optical profile which results in an exponential damping of the Fresnel coefficients [35,133]

$$r_{i,i+1}^{\text{rough}} = r_{i,i+1} \cdot e^{-k_{z,i} \cdot k_{z,i+1} \cdot \sigma^2} \tag{4.14}$$

where σ describes the roughness as the root mean square of the vertical interface roughness. Another way to treat the roughness of interfaces is the so called multi-slicing method, where the chemical profile is approximated by slicing the interface artificially into multiple layers with varying density but no roughness between those layers. This methods gives more flexibility and the optical profile is not restricted to the shape of an error function.

In the Parratt formalism, the polarization of the light is fixed when the light propagates through a sample. However, in real systems there can be transitions between polarizations. This can be handled by the so called matrix formalism, that was introduced 1990 by Mansuripur [134] and Zak et al. [135]. In the matrix formalism both the propagation of light between interfaces and the reflection and transmission at interfaces is described by 4×4 matrices. To solve this problem, iterative matrix products and solutions to the corresponding systems of linear equations are used. This replaces the recursive algorithm, that was introduced by Parratt. For more details about the matrix formalism see [35,134–141].

X-Ray Resonant Magnetic Reflectometry

Modeling XRR experimental data with either of the formalism described above allows to retrieve chemical depth profiles of a multilayered sample with high accuracy. As described in section 3.2.2 and 3.2.3, the x-ray optical properties for magnetic atoms and circular polarized light depend on the orientation of photon helicity and sample magnetization with respect to each other. This can be exploited in XRMR measurements, where XRR data with both orientations are measured and the magnetic depth profile of a sample is retrieved by modeling these measurements.

The atomic scattering factor of a magnetic atom, that relates incident and scattered x-rays with polarization $\vec{e}_i$ and $\vec{e}_f$, respectively, with each other, is described by [35,142]

$$\begin{aligned} f(q,\omega,\vec{e}_f,\vec{e}_i) &= -(\vec{e}_f^{\,*}\cdot\vec{e}_i)\cdot[f_1(\omega)+if_2(\omega)] \\ &+i(\vec{e}_f^{\,*}\times\vec{e}_i)\cdot\vec{b}\cdot[\Delta f_1^{\mathrm{mag}}(\omega)+i\Delta f_2^{\mathrm{mag}}(\omega)]., \end{aligned} \tag{4.15}$$

with the Henke-Gullikson atomic factors $f_1(\omega)$ and $f_2(\omega)$ and the magnetic components of the scattering factor $\Delta f_1^{\mathrm{mag}}(\omega)$ and $\Delta f_2^{\mathrm{mag}}(\omega)$ as described in section 3.2.3. The vector $\vec{b}$ defines the direction of the magnetic moment of the atom and takes the following form in spherical coordinates:

$$\vec{b} = \begin{pmatrix} \sin\Theta_{\mathrm{M}}\sin\varphi_{\mathrm{M}} \\ \sin\Theta_{\mathrm{M}}\cos\varphi_{\mathrm{M}} \\ cos\Theta_{\mathrm{M}} \end{pmatrix}. \tag{4.16}$$

With the geometry introduced in Fig. 4.2 the vectors for σ and π polarized light can be described by

$$\vec{e}_\sigma = \begin{pmatrix} 1 \\ 0 \\ 0 \end{pmatrix}, \qquad \vec{e}_\pi = \begin{pmatrix} 0 \\ \sin\Theta \\ \cos\Theta \end{pmatrix}, \tag{4.17}$$

and left and right circular polarized light by a combination of these two:

$$\vec{e}_{\mathrm{l}} = \frac{1}{\sqrt{2}} \cdot (\vec{e}_{\sigma} + i\vec{e}_{\pi}), \qquad \vec{e}_{\mathrm{r}} = \frac{1}{\sqrt{2}} \cdot (\vec{e}_{\sigma} - i\vec{e}_{\pi}). \tag{4.18}$$

With these polarization definitions, equation 4.15 can be rewritten in terms of the possible combinations of incident and scattered light polarization $(\vec{e}_i \rightarrow \vec{e}_f)$ [35]:

$$\sigma \rightarrow \sigma : \tag{4.19}$$
$$f = [f_1 + if_2]$$

$$\pi \rightarrow \pi : \tag{4.20}$$
$$f = [f_1 + if_2]$$

$$\mathrm{l} \rightarrow \mathrm{l} : \tag{4.21}$$
$$f = [f_1 + if_2] - i[\Delta f_1^{\mathrm{mag}} + i\Delta f_2^{\mathrm{mag}}] \cdot [\sin\Theta \cos\Theta_{\mathrm{M}} - \cos\Theta \sin\Theta_{\mathrm{M}} \sin\varphi_{\mathrm{M}}]$$

$$\mathrm{r} \rightarrow \mathrm{r} : \tag{4.22}$$
$$f = [f_1 + if_2] + i[\Delta f_1^{\mathrm{mag}} + i\Delta f_2^{\mathrm{mag}}] \cdot [\sin\Theta \cos\Theta_{\mathrm{M}} - \cos\Theta \sin\Theta_{\mathrm{M}} \sin\varphi_{\mathrm{M}}]$$

$$\sigma \rightarrow \pi : \tag{4.23}$$
$$f = -[\Delta f_1^{\mathrm{mag}} + i\Delta f_2^{\mathrm{mag}}] \cdot [\cos\Theta \cos\Theta_{\mathrm{M}} + \cos\Theta \sin\Theta_{\mathrm{M}} \sin\varphi_{\mathrm{M}}]$$

$$\mathrm{l} \rightarrow \mathrm{r} : \tag{4.24}$$
$$f = 0$$

Measurements with different polarizations for $\vec{e}_i$ and $\vec{e}_f$ are usually not accessible in experiments, since they would require a polarization filter. The highest magnetic contrast is achieved for measurements $\mathrm{l} \rightarrow \mathrm{l}$ and $\mathrm{r} \rightarrow \mathrm{r}$ and taking their difference, which is done in XRMR measurements.

The same contrast is achieved when switching the magnetization direction instead of the circular polarization.

4.2.2 ERNSt – The Experimental Reflectometry Setup

The magnetic reflectometer setup ERNSt (*Stuttgart Novel Reflectometer Experiment*) is used for the XRR and XRMR measurements in this chapter, for the XAS and XMCD measurements in chapter 3, and for the VXRR measurements in chapter 5. The measurements with ERNSt were performed at the UE56-2 PGM-2 beamline at the BESSY II synchrotron in Berlin, Germany. A brief introduction to the relevant features of the experimental setup is given in this section while a detailed summary can be found in [103].

ERNSt is an experimental setup which is dedicated to XAS, XMCD, XRR, and XRMR measurements in the soft x-ray regime. Figure 4.4 shows a 3D model of the setup. Since it is designed for operation with soft x-rays it is build as an ultra-high vacuum (UHV) chamber with a possible base pressure down to $2 \cdot 10^{-10}$ mbar. Figure 4.5 shows a schematic of the setup in the main and I_0 chamber. The incoming x-ray intensity reference I_0 can be monitored via a SiN membrane, an Al foil, or (as in the case of the present experiments) a gold mesh. ERNSt has detectors to simultaneously measure TEY, total fluorescence yield (TFY), fluorescence yield background (FYB), and the specular reflected x-rays. The magnet system is build up of two water cooled field coils with 1300 windings each, which are located outside of the UHV chamber. The field is guided by an iron yoke into the chamber and depending on the yoke gap a field of 639 mT (for 10 mm gap) or 261 mT (for 30 mm gap) can be achieved. The magnet can be rotated from $-10°$ to $100°$ and the detector for specular reflection from $-30°$ to $140°$ with respect to the incoming x-rays. The rotary feed-through allows for a $360°$ rotation of the sample. The magazine in

the sample storage can carry up to six samples and the loadlock enables a fast and easy way to exchange samples without venting the whole system. The software to control ERNSt and all possible measurements modes is written in *LabVIEW*. The measurement modes include point by point Θ, 2Θ, $\Theta - 2\Theta$, energy, magnetic field, and constant q_z scans, as well as fast scanning modes where Θ or the energy can be swept continuously.

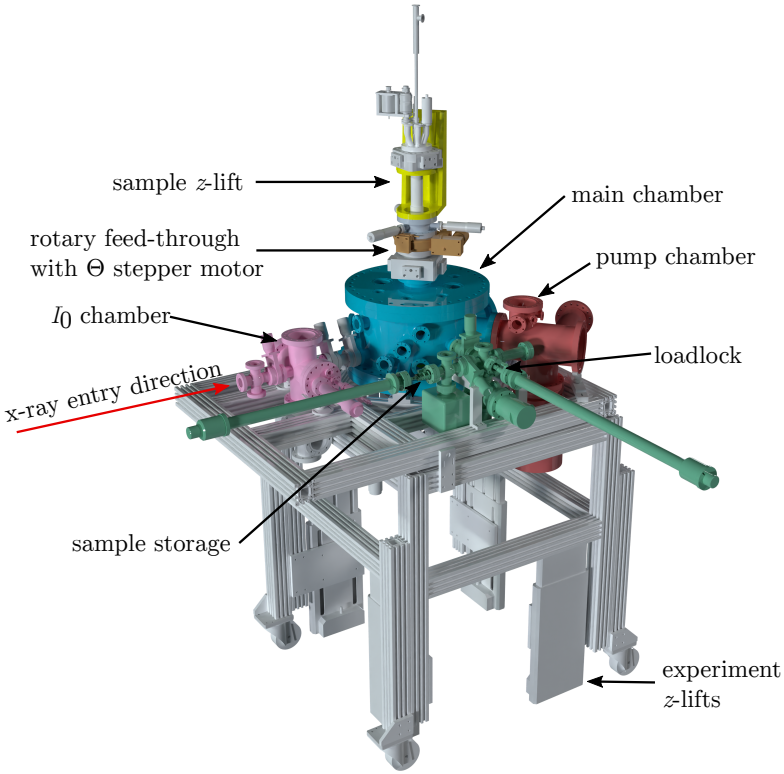

Figure 4.4: 3D model of the magnetic reflectometer experiment ERNSt.

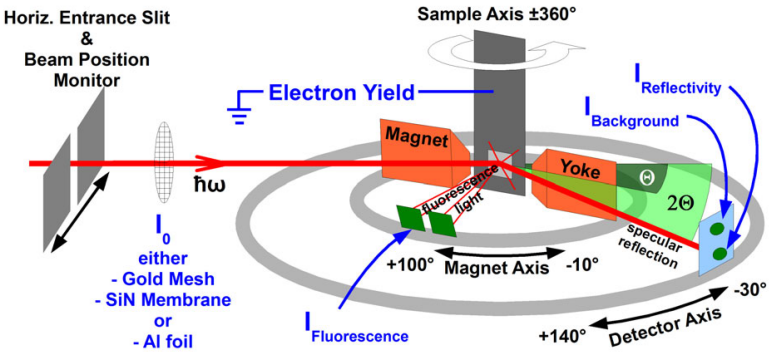

Figure 4.5: Schematic of the experimental setup in the main and I_0 chamber of ERNSt. The figure is taken from [103].

4.2.3 XRR and XRMR Measurement Procedure

Figure 4.6a shows a typical constant q_z scan, where the momentum transfer q_z is kept constant by adjusting the angle Θ as the energy is scanned. Thus, the path difference between layers stays constant for all energies. To obtain a data point, the reflected x-ray intensity I_{Det} and the x-ray intensity reference I_0 are measured for a given integration time (usually between 0.5 s and 10 s), which is chosen appropriately, and then averaged. Figures 4.6b and 4.6c show the raw data which result in the measurement point marked with the red cross in Fig. 4.6a. After each data point, the angle Θ, the photon energy, or both are changed (depending on the measurement mode) to move on to the next data point. Before the data acquisition for the next data point begins, there is a delay time (usually between 0.1 s and 3 s), which can be seen in Figs. 4.6b and 4.6c since the averaging for the data point only starts after a 3 s delay.

There is also the option for fast $\Theta - 2\Theta$ and fast photon energy scans. In this mode Θ or the photon energy are swept continuously with fixed speeds (typically $0.1-0.4\,^\circ$/s and $0.1-1$ eV/s, respectively) and the inte-

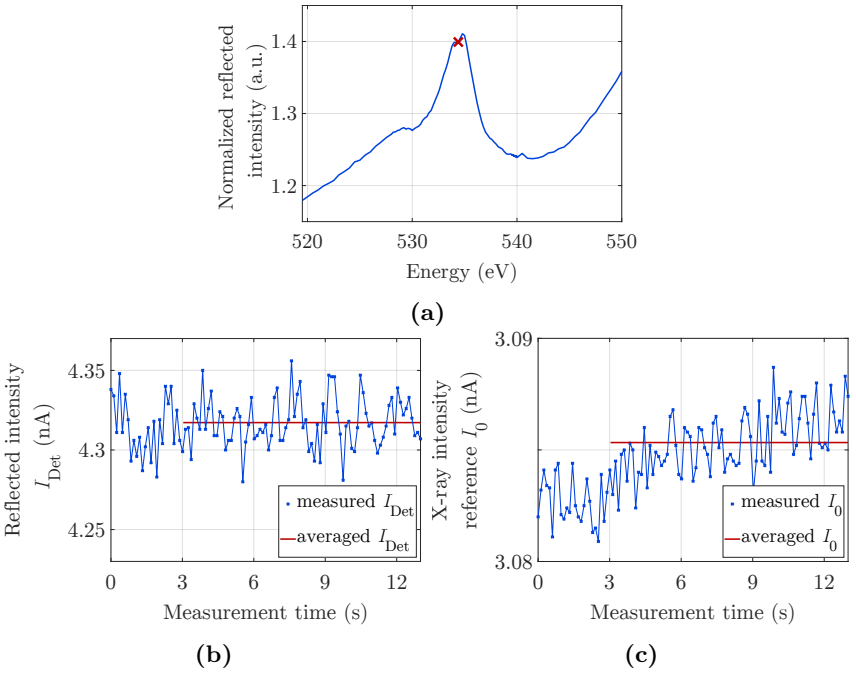

Figure 4.6: (a) Normalized reflected x-ray intensity of a typical constant q_z scan. (b) and (c) display the measured I_{Det} and I_0, respectively, within the 13 s measurement interval for the data point marked with a red cross in (a). The average for I_{Det} and I_0 over the 10 s integration interval is shown in red.

gration time is set to small values around 0.2 s. This allows for much faster scans compared to point by point scans, but the signal to noise ratio of the data suffers slightly.

4.2.4 Processing XRR and XRMR Data

In order to obtain physically meaningful results such as structural parameters and magnetic depth profiles from x-ray reflectometry measurements,

simulations are required. For this purpose the software package *ReMagX* is used [35,36,130]. Structural parameters of a sample, such as layer thicknesses and interface roughnesses, and the x-ray optical parameters are the input parameters in *ReMagX* and are used to calculate the reflected x-ray intensity. The results of this calculation are then compared with measured reflectivity curves and the input parameters are adjusted until the calculation and measurements match.

Preparing Raw Data for *ReMagX*

Before explaining in detail the procedure of fitting data with *ReMagX* and how to retrieve chemical and magnetic depth profiles, the process of preparing raw data for *ReMagX* has to be explained. First the measured data of all detectors (TEY, TFY, FYB, and the detector for specular reflection) have to be normalized with the simultaneously measured x-ray intensity reference I_0. Since reflectivity measurements are usually plotted as a function of momentum transfer q_z instead of Θ, q_z has to be calculated via equation 4.1. When plotted as function of q_z instead of Θ, measurements at different energies are easier to compare because the interference conditions remain similar for equal q_z values, which is not the case when plotted as function of Θ.

When multiple measurements were done with the same measurement parameters and are supposed to be averaged they need to be interpolated to a common x-axis. The same has to be done for reflectivity measurements with parallel and antiparallel orientation of sample magnetization and photon helicity in order to calculate the magnetic asymmetry A_{mag}:

$$A_{\mathrm{mag}} = \frac{I_{\uparrow\uparrow} - I_{\uparrow\downarrow}}{I_{\uparrow\uparrow} + I_{\uparrow\downarrow}}, \tag{4.25}$$

with the respective reflected x-ray intensities $I_{\uparrow\uparrow}$ and $I_{\uparrow\downarrow}$.

Once the measured data has been properly prepared, it can be imported into *ReMagX*. For XRR measurements only the q_z and normalized reflected intensity I data needs be imported, whereas for XRMR measurements q_z, normalized reflected intensities $I_{\uparrow\uparrow}$ and $I_{\uparrow\downarrow}$, and the magnetic asymmetry A_{mag} has to be imported. For constant q_z measurements, an array of the photon energies at which the measurements were done is also required. The last step is to set parameters like photon polarization, photon energy (for measurements with constant energy), angular resolution, and an intensity scaling factor in *ReMagX* for the corresponding measurement data (see the right panel in Fig. 4.7).

Retrieving Chemical Depth Profiles with *ReMagX*

In order to retrieve chemical depth profiles, a model of the studied sample is created in *ReMagX*. The theoretically reflected x-ray intensity of this model is calculated and compared with measured data at the real sample. Figure 4.7 shows a screenshot of *ReMagX* at the beginning of the simulation process for a sample with a Si substrate and SiO_2, Fe, Cr, and Au layers of nominal thicknesses 50 nm, 2 nm, 1 nm, 10 nm, respectively. The individual layers are defined in the top left panel with their x-ray optical properties δ and β, and the interface roughness σ. For energies far away from resonance edges, the real and imaginary components δ and β of the complex refractive index $n = 1 - \delta + i\beta$ can be taken from x-ray optical property databases such as [74] or [75]. There are two different modes in *ReMagX* for the description of the layers, the compound mode and the element mode. In the compound mode, the top left panel consists of a table of different compound materials, where a compound can consist of a single element or of a group of elements that have a homogeneous density distribution within the layer. The x-ray optical constants of a compound are

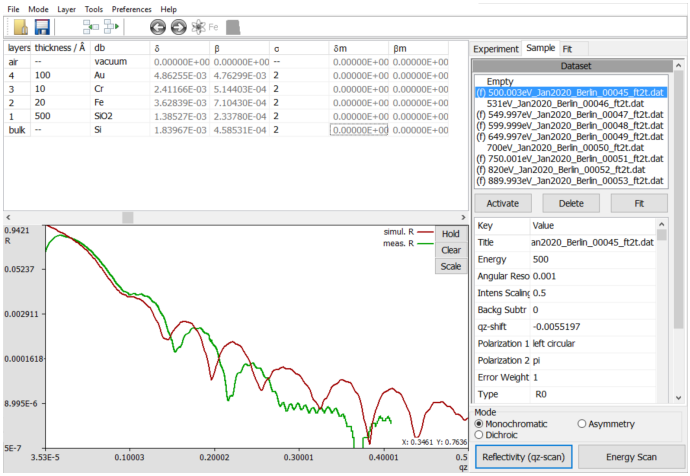

Figure 4.7: Screenshot of the *ReMagX* software. The individual layers for the current simulation are defined in the top left panel. The current experimental and simulated curves are displayed in the bottom left panel. The right panel shows all imported data sets and the corresponding settings.

achieved by a linear combination of the element-specific scattering factors of the constituents. In the element mode, there are separate layer profiles for each element with the molar density as parameter and instead of the x-ray optical constants δ and β the atomic scattering factors f_1 and f_2 are used. The advantage of the element mode is that the layer profile for each element can be freely chosen and, for example, if an element has different valences (with different on-resonant scattering factors), a separate layer can be introduced for each valence with the corresponding scattering factors. In the right panel of Fig. 4.7 all imported measurement sets and the corresponding settings are displayed. The bottom panel shows the measured reflectivity curve in green and the simulated curve in red. For the calculation of the curves the Parratt [132,143,144] and the matrix [135–137] formalism are available.

As a first step, the layer thicknesses and roughnesses should be adjusted manually in compound mode until the measured and calculated reflected intensities roughly match. Next, reflectivity measurements at different energies can be fitted simultaneously. Which layer thicknesses and roughnesses should be included in the fit and appropriate limits can be set individually. For the fitting process three different algorithms are available: downhill simplex algorithm [145] (with and without simulated annealing), Levenberg & Marquardt algorithm [146,147], and an evolution (genetic) algorithm [148–150]. For more complex models of a sample, such as layers of elements with different valences, the next step is to switch to element mode. Here, the structural parameters that should be used as free parameters in the fit can be selected again and the available fitting algorithms can be used to fit measured reflectivity curves. Once a mutual parameter set (layer thicknesses and roughnesses) is found where the calculated and measured reflectivity curves sufficiently match they can be read out of the layer input table. Those parameters represent the real structure of the studied sample and can be used to plot depth dependent elemental distributions, so called chemical depth profiles.

Retrieving Magnetic Depth Profiles with *ReMagX*

To obtain information about the depth dependent magnetization of magnetic layers, magnetic asymmetries A must be measured. For this, reflectivity curves at the corresponding resonant magnetic absorption edge are measured with parallel and antiparallel orientation of the sample magnetization and x-ray photon helicity. The magnetic asymmetry A_{mag} is then calculated according to Eq. 4.25. For the simulation of the asymmetry the resonant x-ray optical parameters are needed. They are not tabulated, like the off resonant optical parameters, but need to be retrieved from XAS and XMCD measurements, as described in chapter 3.

For fitting the magnetic asymmetry, the structural parameters of the chemical depth profile are kept constant. An artificial layer is introduced for the fit which only carries the magnetic scattering factors $\Delta f_1^{\mathrm{mag}}$ and $\Delta f_2^{\mathrm{mag}}$, retrieved from XMCD measurements, while the corresponding chemical layer carries the resonant scattering factors f_1 and f_2. Position, thickness, roughness, and density of the artificial magnetic layer are then the free parameters for fitting the magnetic asymmetry. The density is proportional to the magnetization of the magnetic layer and can also take negative values for layers with antiparallel magnetic orientation. While fitting the parameters need to be kept within physically reasonable boundaries (e.g. position must be within chemical layer and density should not exceed the density of the chemical layer) for the results to be meaningful. For higher accuracy of the results, magnetic asymmetries at various energies around an resonant edge can be measured and fitted simultaneously.

4.2.5 Magnetometry

The magnetic field and temperature dependent magnetic moment measurements in this chapter were performed with a state of the art superconducting quantum interference device (SQUID) by *Quantum design*. Namely, the *Quantum Design MPMS 3 SQUID VSM* (see Fig. 4.8a) was used, which has a temperature range of $1.8-1000\,\mathrm{K}$, a sensitivity of $\leq 10^{-8}\,\mathrm{emu}$ in optimal conditions, and a magnetic field of $\pm 7\,\mathrm{T}$ can be applied [151]. The SQUID at hand is an RF-SQUID, which has a single Josephson junction in a superconducting loop. The magnetic flux through a superconducting loop can only be integer multiples of the magnetic flux quantum Φ_0. In an RF-SQUID, the superconducting loop is inductively coupled to a tank circuit which is driven with I_{rf}. The amplitude of the RF-voltage, which is read out with the connected preamplifier, is periodic in the applied flux Φ_A

with period Φ_0. For further details on the functional principles of SQUIDs literature such as [152,153] is recommended.

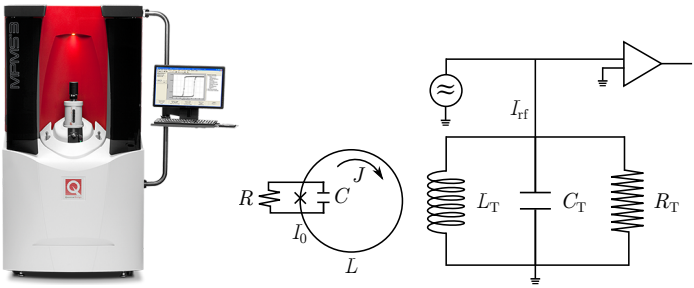

Figure 4.8: (a) Image of the *Quantum Design MPMS 3 SQUID VSM* (taken from [151]) and (b) a schematic of the circuit diagram of an RF-SQUID with the superconducting loop on the left and the tank circuit with preamplifier on the right (reproduced from [152]).

4.2.6 Transmission Electron Microscopy

Transmission electron microscopy (TEM) is an imaging technique, which can be used to obtain local information on buried layers with high depth resolution. In transmission electron microscopy, a beam of electrons passes through a sample and is detected to produce an image. In order for the electrons to be able to pass through the sample it has to be thinner than $\approx$ 100 nm. For thin film systems a lamella has to be cut out of the layer stack with a FIB and thinned down to the required thickness[154]. In Fig. 4.9 the process of preparing such a lamella is shown. A *JEOL ARM200F* microscope was used to measure such a lamella of a sample studied in this chapter, thus imaging the profile of the layer stack. Additional techniques such as EDX and EELS can provide element-specific information. More details about TEM can be found in [155].

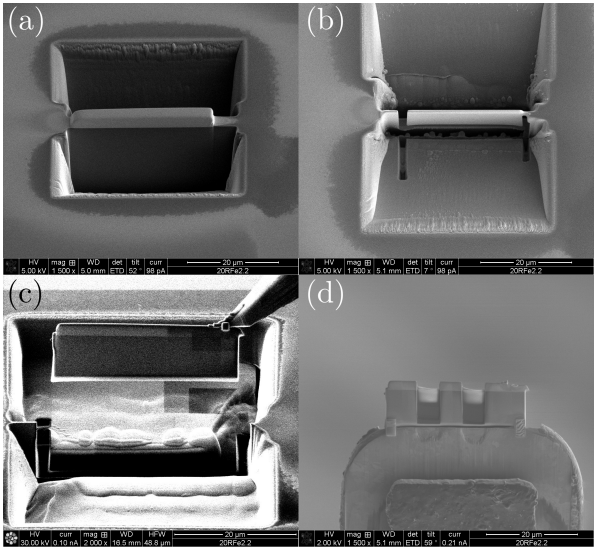

Figure 4.9: Four different stages of preparing a lamella of a multilayered sample with focused ion beam (FIB) for cross sectional TEM measurements are shown. (a) Milling a triangular trench to expose the cross section of the layered sample. (b) A so called J-cut is made to separate the bottom and sides of the lamella from the sample. (c) Lift out of the lamella with a micromanipulator. After the lift out, the lamella is attached to a TEM grid. (d) Lamella on the TEM grid, with two thinned windows that are electron transparent.

4.2.7 Sample Preparation

For the samples, a p-type (boron) doped Si (100) wafer with a resistivity of $0.001 - 0.05\,\Omega\,\mathrm{cm}$ and a dry thermally oxidized SiO_2 layer with a nominal thickness of $(50 \pm 30)\,\mathrm{nm}$ was used as substrate. The wafer was ordered from `https://www.microchemicals.com/de/`. The wafer was cut into pieces of $5 \times 5\,\mathrm{mm}^2$. By drawing over the boarder of the substrate with a permanent marker, deposition of material in the marked area is prevented. This technique is called marker pen lithography and is used to obtain

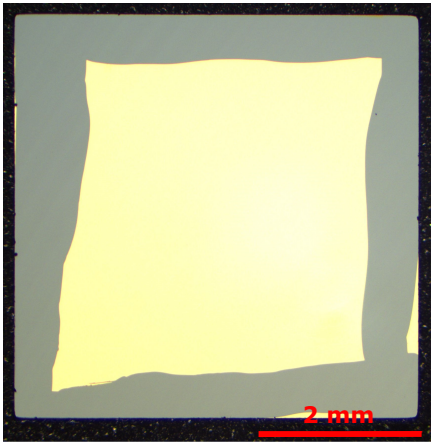

Figure 4.10: Light microscope image of a reflectometry sample. The bare SiO_2 surface is visible at the edge of the substrate, while the Au surface is visible in the center.

sharp layer edges with no electrical short between the layers [156]. Layers of magnetic TMs, Cr, and Au are grown on top of the wafer by ion beam sputtering, a schematic of the sample design is shown in Fig. 4.1. As magnetic TMs layers Fe, Co, and Ni, respectively, are chosen. The nominal thicknesses of the layers are 10 nm for the Au layer, 1 nm for the Cr layer, and for the magnetic TM layers samples with 2 nm and 10 nm thick layers are sputtered. After sputtering, the permanent marker, and with it the material deposited onto it, is removed with acetone in a ultrasonic bath. The deposited material stays on the substrate in areas where no permanent marker was. In Fig. 4.10 an image of a finished sample is shown, at the border the SiO_2 surface and in the middle of the substrate the Au surface can be seen.

4.3 XRR and XRMR Measurements – Chemical and Magnetic Depth Profiles

The chemical and magnetic depth profiles and the magnetic properties of six different samples are studied in this chapter. One sample with a 2 nm Fe layer, two different samples with a 2 nm Co layer (labeled 2 nm Co(I) and 2 nm Co(II)), one sample with a 10 nm Co layer, and two different samples with a 2 nm Ni layer (labeled 2 nm Ni(I) and 2 nm Ni(II)). The exact chemical and magnetic depth profiles of the samples are retrieved from XRR and XRMR measurements. Figure 4.11 shows the sample design and the measurement geometry together with the direction of the applied magnetic field. All reflection measurements in this chapter are done at room temperature and for the XRMR measurements an in-plane magnetic field of 117 mT was applied. Off-resonant $\Theta - 2\Theta$ measurements

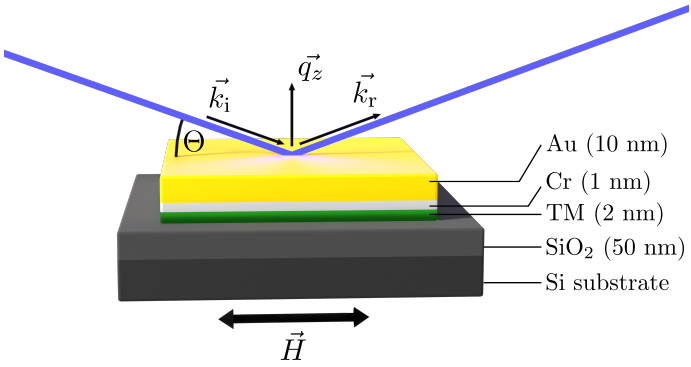

Figure 4.11: Schematic of the sample design and measurement geometry for XRR and XRMR measurements. The incident and reflected x-rays are shown in blue with the wave vectors $\vec{k}_\mathrm{i}$ and $\vec{k}_\mathrm{r}$, respectively. The momentum transfer $\vec{q}_z$ is defined as the difference between $\vec{k}_\mathrm{r}$ and $\vec{k}_\mathrm{i}$. The magnetic field $\vec{H}$ is applied parallel to the plane of incidence and the sample surface.

are performed with linearly π-polarized x-rays at various x-ray photon energies between 500 eV and 890 eV at each sample in order to extract the exact chemical depth profile. For one sample, all off-resonant measurements are simulated simultaneously with *ReMagX* using the same set of structural parameters. This provides much more redundancy compared to single photon XRR measurements, which means that the accuracy of the results obtained is increased [35,36].

In order to obtain magnetic depth profiles of the magnetic TM layers, measurements with circular polarized x-rays and the photon helicity parallel and antiparallel to the sample magnetization (at $\Theta = 0°$) are performed at the respective TM L_3-edge. The resulting magnetic asymmetry A_{mag} (see Eq. 4.25) is then fitted again with *ReMagX* to obtain the magnetic depth profile. The exact procedure of the fitting process with *ReMagX* is described in section 4.2.4. Temperature dependent SQUID measurements are performed to obtain detailed information about the saturation magnetizations. Furthermore, a cross sectional TEM image is taken from the 2 nm Fe sample.

4.3.1 Iron Sample

XRR measurements and the corresponding *ReMagX* fits for the sample with a 2 nm Fe layer are shown in Fig. 4.12. Reflectivity curves were measured at 9 different off-resonant photon energies between 500 eV and 890 eV. The *ReMagX* fits were calculated simultaneously with a mutual set of structural parameters, which consists of the thickness and roughness at the top and bottom interface for each individual layer. The accuracy of the results is increased by fitting the samples structure on the basis of reflectivity measurements at various photon energies. By tuning the photon energy over an elements characteristic absorption edge, the x-ray

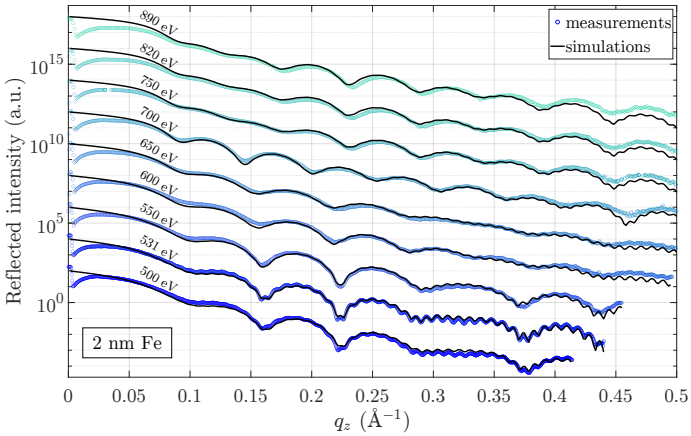

Figure 4.12: X-ray reflectivity measurements between 500 eV and 890 eV and the corresponding *ReMagX* fits for the 2 nm Fe sample. For a better readability of the figure, measurements at different energies are plotted with a vertical offset.

absorption of the respective layer will increase and less x-rays reach the layers underneath. Thus, less reflected intensity from layers and interfaces below reaches the detector. This way the sensitivity for specific layers and interfaces can be enhanced by the choice of photon energy. Also the statistics is increased in a straightforward way by fitting multiple energies at the same time[35,36].

The measured x-ray reflectivity curves in Fig. 4.12 show the typical behavior of soft x-ray reflectometry data. The intensity decreases exponentially (see equation 4.14) with increasing momentum transfer q_z, and characteristic intensity variations arising from multiple reflection at the samples interfaces are visible. The intensity variations with the shortest periodicity, which are most pronounced at 531 eV, reflect the total thickness of the layer stack. Since the total thickness is dominated by the SiO_2 layer the exact thickness of it can be very well determined by fitting those short periodic intensity variations. The fits show that the SiO_2 layer has

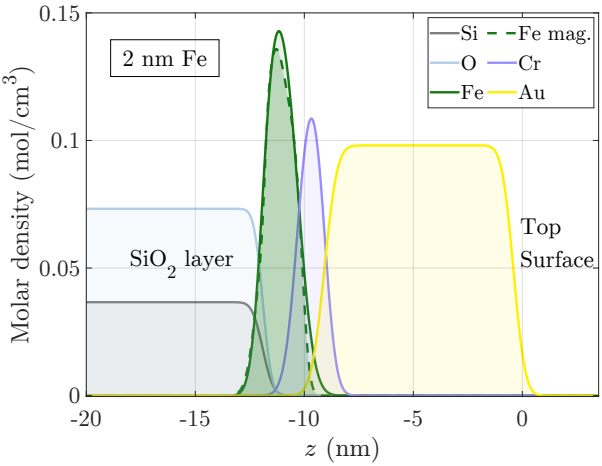

Figure 4.13: Chemical and magnetic depth profile of the 2 nm Fe sample. The magnetic depth profile of the Fe layer is shown with the dashed green line.

a thickness of 59.1 nm and by changing this thickness only by ±0.5 nm the fit for the short periodic intensity variations is completely off. The other intensity variations can not be attributed to one particular layer but arise from a complex interference of x-rays reflected multiple times at the interfaces of the sample. However, the structural parameters of the sample, namely the thickness and the roughness at the top and bottom interfaces of each layer, can still be obtained from the fits and are listed in table 4.1. The corresponding plot of the chemical depth profile can be seen in Fig. 4.13.

In order to retrieve the magnetic depth profile, reflectivity measurements with circular polarized x-rays are performed 2.2 eV before the maximum of the Fe L_3-edge (at 704 eV) and at the maximum (at 706.2 eV). At both energies, measurements with parallel and antiparallel orientation of photon helicity and sample magnetization are executed and the magnetic asymmetries are calculated with equation. 4.25. Figure 4.14 shows the

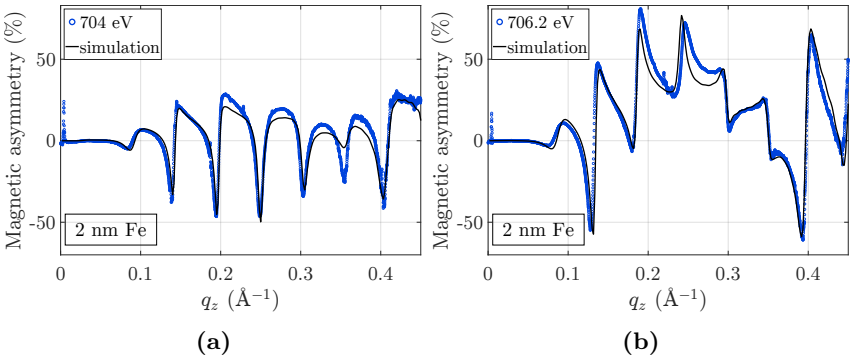

Figure 4.14: Magnetic asymmetries measured at the 2 nm Fe sample with photon energies (a) 2.2 eV before the maximum and (b) at the maximum of the Fe L_3-edge. The corresponding *ReMagX* fits are plotted in black.

magnetic asymmetries and the corresponding *ReMagX* fits. The magnetic and non-magnetic x-ray optical parameters used for the fits were retrieved from XAS and XMCD measurements at a quasi bulk reference sample with a 10 nm Fe layer, as described in chapter 3, and can be seen in Fig. 3.7. As can be seen, the real components of the x-ray optical properties f_1 and f_1^{mag} dominate for the measurement before the L_3-edge, while the complex component f_2 and f_2^{mag} dominate at the maximum of the L_3-edge. Again, one set of parameters for the magnetic depth profile is used to fit both magnetic asymmetries simultaneously, which enhances the accuracy of the results compared to only fitting at one energy. The resulting magnetic depth profile is indicated with the dashed green line in Fig. 4.13. The overall molar density of the magnetic layer is slightly lower than the one of the chemical Fe layer. Since the molar density of the magnetic layer is proportional to its magnetization (as described in section 4.2.4), the lower density indicates that the saturation magnetic moment per Fe atom is slightly reduced when compared to the room temperature saturation magnetization of the quasi bulk 10 nm reference sample. In addition, there is a thin layer with an even greater reduction in magnetization at the Fe/Cr

interface. At the SiO_2/Fe interface, no such magnetization reduction is visible.

Figure 4.15 shows a dark field TEM image of the cross section of the 2 nm Fe sample. At the top the protective Pt layer is visible, that was added while preparing the TEM lamella. The Fe and Cr layer cannot be distinguished here because they have a similar scattering cross sections. The Au and Fe+Cr layer thickness from the image can be determined to roughly (9.2 ± 0.5) nm and (3.2 ± 0.5) nm, respectively, which is in good agreement with the values retrieved from the *ReMagX* fits.

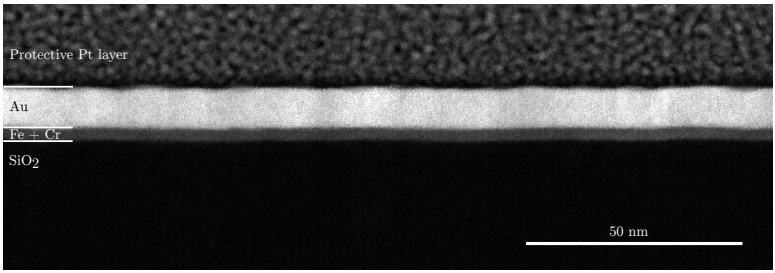

Figure 4.15: Annular dark field TEM image of the cross section of the 2 nm Fe sample.

Table 4.1: Structural parameters of the 2 nm Fe sample determined from XRR measurements. The up and down arrows denote the roughness at the top and bottom interface of the respective layer.

Layer	Thickness (nm)	Roughness (nm)	
Au	8.7	$\uparrow$ 0.42	$\downarrow$ 0.47
Cr	1.2	$\uparrow$ 0.43	$\downarrow$ 0.49
Fe	1.6	$\uparrow$ 0.57	$\downarrow$ 0.43
SiO_2	59.1	$\uparrow$ 0.38	$\downarrow$ 0.10

4.3.2 Cobalt Samples

The same set of measurements which were performed in the previous section at the 2 nm Fe sample are now performed on samples where Fe was substituted by Co. However, in this case two different samples with a 2 nm Co layer, henceforth referred to as 2 nm Co(I) and 2 nm Co(II), and one sample with a 10 nm Co layer are studied. A schematic of the layer stack is shown in Fig. 4.11. The two samples with the 2 nm Co layer were not sputtered all at once but rather consecutively. The nominal sputtering conditions and layer thickness settings, however, were the same for both samples. Nevertheless, tiny structural variations will inevitable occur between the two samples introduced by the sputtering process itself or differences in the substrate and its surface. This way the effect of tiny structural variations on the magnetic depth profile can be studied.

In order to determine the chemical depth profile XRR measurements at room temperature and at multiple x-ray photon energies between 500 eV and 890 eV are performed for all three samples. In Figs. 4.16, 4.17, and 4.18 the corresponding x-ray reflection curves and *ReMagX* fits are shown for 2 nm Co(I), 2 nm Co(II), and 10 nm Co, respectively. Again, the thickness of the SiO_2 layer can be fitted with high accuracy on the basis of the short periodic reflected intensity variations that are most pronounced around 530 eV. The resulting structural parameters are listed in table 4.2 and the layer profiles are plotted in 4.19, 4.20, and 4.21. Small structural variations between 2 nm Co(I) and 2 nm Co(II) can be seen from the results. Especially the Au and Cr layers are thinner and the roughness between Co/Cr and Cr/Au is more pronounced for sample 2 nm Co(I). The magnetic depth profiles which are shown with dashed orange lines in the layer profile plots were obtain by fitting the magnetic asymmetries shown in Figs. 4.22, 4.23, and 4.24. The magnetic and non-magnetic x-ray optical properties at the Co L_3-edge necessary for the fits are retrieved from XAS and XMCD at a quasi bulk reference sample with a 10 nm Co layer

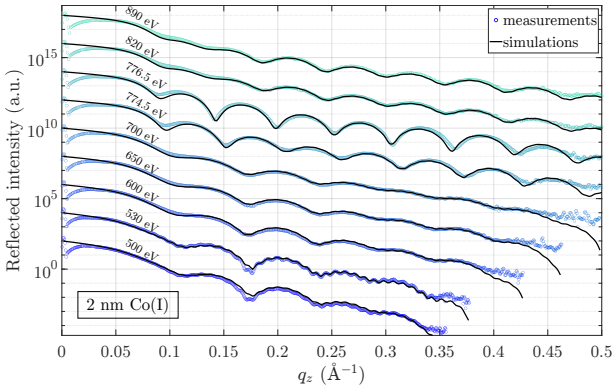

Figure 4.16: X-ray reflectivity measurements between 500 eV and 890 eV and the corresponding *ReMagX* fits for the 2 nm Co(I) sample. For a better readability of the figure, measurements at different energies are plotted with a vertical offset.

and are shown in Figs. 3.8. The magnetic depth profile of both 2 nm samples show an overall reduced magnetic moment per Co atom and similar to the 2 nm Fe sample there is again a thin layer at the Co/Cr interface where the magnetization is even more reduced. The magnetic layer of the 2 nm Co(I) sample has a slightly lower density and the Co/Cr interface is slightly rougher compared to sample 2 nm Co(II). This results in a overall smaller amplitude of the magnetic asymmetry for the 2 nm Co(I) sample. However, the general shape of the magnetic asymmetries is about the same for both samples (see Figs. 4.22 and 4.23). The different magnetic properties between the two samples may originate from the higher interface roughnesses between cobalt, chromium and gold for 2 nm Co(I).

In contrast to the 2 nm Co samples the 10 nm Co sample does not show an overall magnetization reduction but it does show a thin layer of reduced magnetization at the Co/Cr interface. This result suggests that the overall reduced magnetization of the 2 nm Co layers arises from the smaller layer thickness and that a 10 nm Co layer is already thick enough to have bulk like magnetic properties.

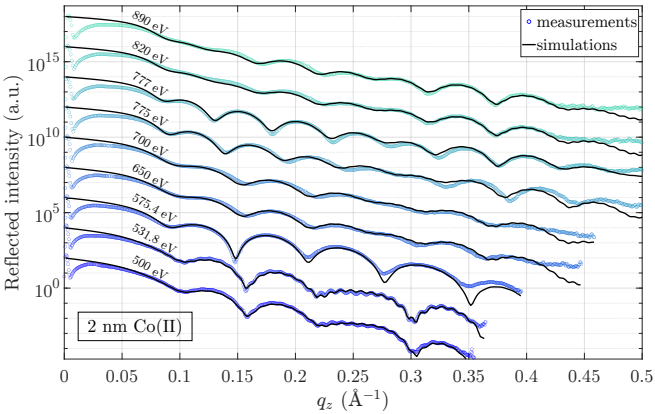

Figure 4.17: X-ray reflectivity measurements between 500 eV and 890 eV and the corresponding *ReMagX* fits for the 2 nm Co(II) sample. For a better readability of the figure, measurements at different energies are plotted with a vertical offset.

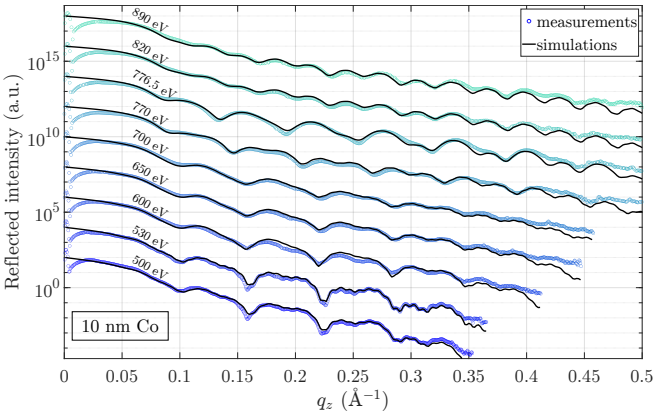

Figure 4.18: X-ray reflectivity measurements between 500 eV and 890 eV and the corresponding *ReMagX* fits for the 10 nm Co sample. For a better readability of the figure, measurements at different energies are plotted with a vertical offset.

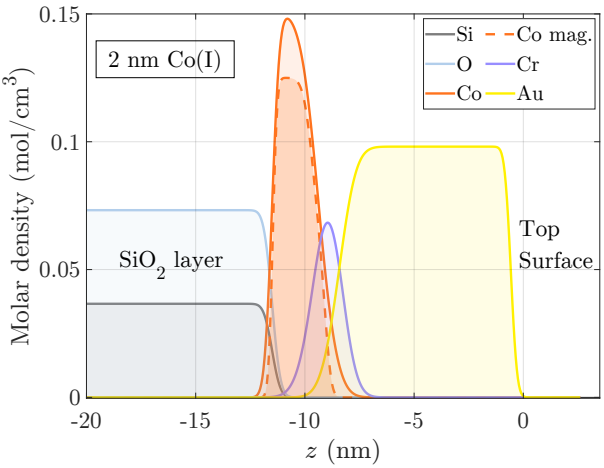

Figure 4.19: Chemical and magnetic depth profile of the 2 nm Co(I) sample. The magnetic depth profile of the Co layer is shown with the dashed orange line.

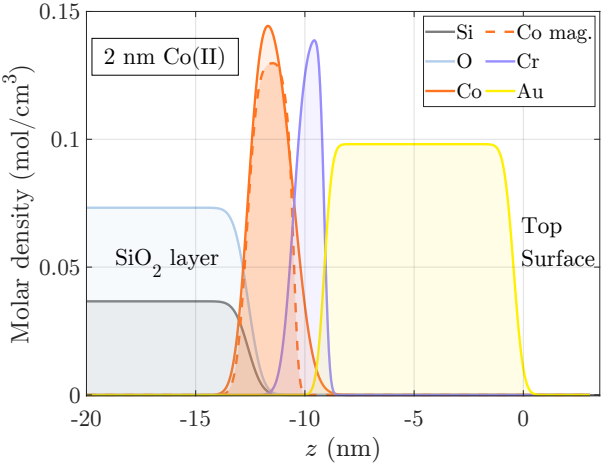

Figure 4.20: Chemical and magnetic depth profile of the 2 nm Co(II) sample. The magnetic depth profile of the Co layer is shown with the dashed orange line.

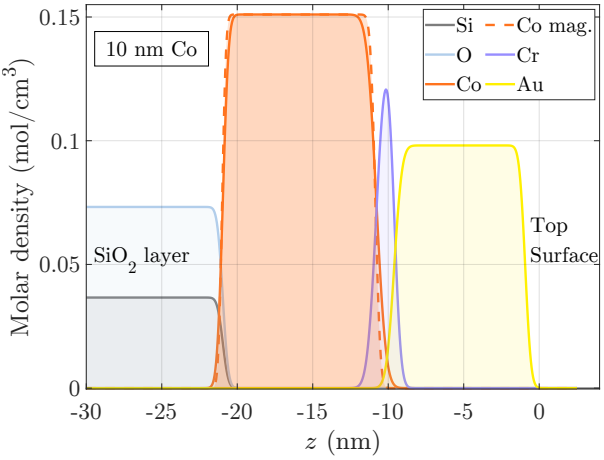

Figure 4.21: Chemical and magnetic depth profile of the 10 nm Co sample. The magnetic depth profile of the Co layer is shown with the dashed orange line.

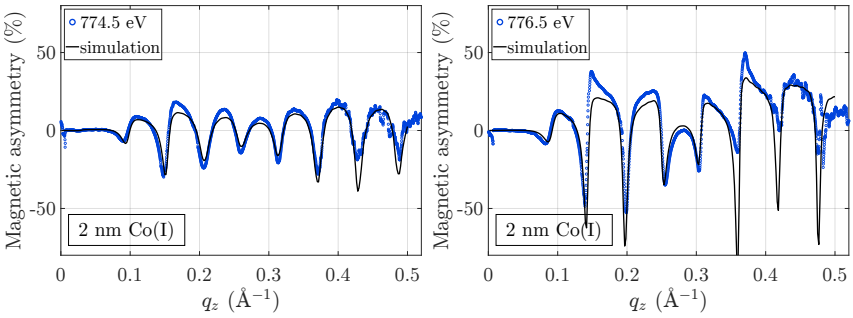

Figure 4.22: Magnetic asymmetries measured at the 2 nm Co(I) sample with photon energies (a) 2 eV before the maximum and (b) at the maximum of the Co L_3-edge. The corresponding *ReMagX* fits are plotted in black.

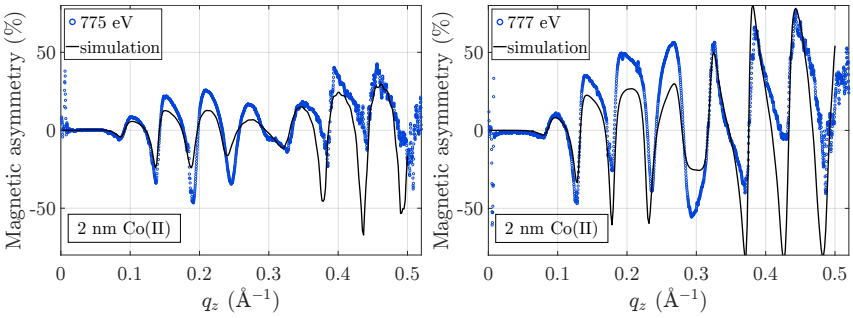

Figure 4.23: Magnetic asymmetries measured at the 2 nm Co(II) sample with photon energies (a) 2 eV before the maximum and (b) at the maximum of the Co L_3-edge. The corresponding *ReMagX* fits are plotted in black.

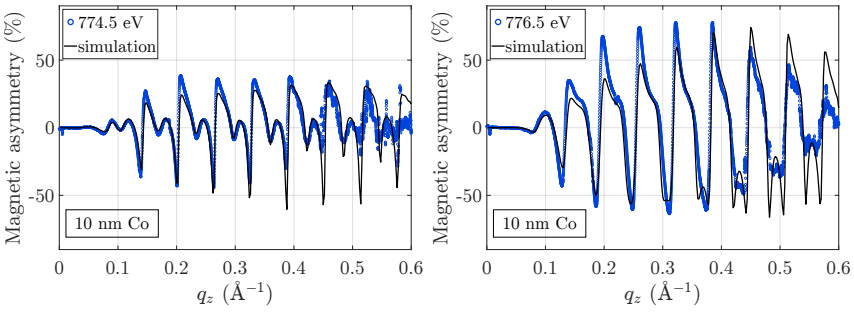

Figure 4.24: Magnetic asymmetries measured at the 10 nm Co sample with photon energies (a) 2 eV before the maximum and (b) at the maximum of the Co L_3-edge. The corresponding *ReMagX* fits are plotted in black.

Table 4.2: Structural parameters of the 2 nm Co(I), 2 nm Co(II) and 10 nm Co samples determined from XRR measurements. The up and down arrows denote the roughness at the top and bottom interface of each layer.

	Layer	Thickness (nm)	Roughness (nm)	
2 nm Co(I):	Au	7.9	↑ 0.22	↓ 0.62
	Cr	0.8	↑ 0.59	↓ 0.73
	Co	2.2	↑ 0.67	↓ 0.27
	SiO_2	58.8	↑ 0.30	↓ 0.10
2 nm Co(II):	Au	8.7	↑ 0.35	↓ 0.29
	Cr	1.4	↑ 0.18	↓ 0.44
	Co	2.1	↑ 0.69	↓ 0.48
	SiO_2	59.0	↑ 0.51	↓ 0.10
10 nm Co:	Au	8.7	↑ 0.31	↓ 0.41
	Cr	1.2	↑ 0.35	↓ 0.48
	Co	10.2	↑ 0.50	↓ 0.30
	SiO_2	59.0	↑ 0.29	↓ 0.10

4.3.3 Nickel Samples

The same measurement procedure as previously for the samples with Fe and Co as magnetic TM layer is performed for two samples with a 2 nm Ni layer. In order to distinguish between the two samples they are referred to as 2 nm Ni(I) and 2 nm Ni(II). A schematic of the layer stack is shown in Fig. 4.11. The two samples were sputtered consecutively under the same nominal conditions and with the same set points for the layer thicknesses. However, there will be tiny structural differences between the two samples induced by the sputtering process and variations of the substrate surface. Similar to the previous study on Co layers, this yields again the opportunity to study the effect of tiny structural variations on the magnetic properties of thin Ni layers sandwiched between SiO_2 and Cr.

The measured x-ray reflectivity curves and corresponding *ReMagX* for the two samples are plotted in Figs. 4.25 and 4.26, respectively. The structural parameters which were retrieved from those fits are listed in table 4.3 and the layer profiles are shown in Figs. 4.27 and 4.28. The structural parameters of the two samples samples are almost identical, with only small differences in interface roughness, and the Au, Cr and Ni layers are each 0.3 nm thinner in the Ni(I) sample. The magnetic depth profiles, which are shown with the dashed blue lines in Figs. 4.27 and 4.28, were retrieved from fits of the magnetic asymmetries shown in Figs. 4.29 and 4.30. For both samples, magnetic asymmetries were measured 2 eV before and at the maximum of the Ni L_3-edge and the fitting with *ReMagX* was done simultaneously at both energies for each sample. The magnetic depth profile reveals that the magnetization of the whole Ni layer in both samples is reduced compared to the magnetization of the quasi bulk reference sample with a 10 nm thick Ni layer. The reduction in magnetization is more pronounced for the 2 nm Ni(I) sample, which has the Ni layer that is 0.3 nm thinner. Comparing the magnetic asymmetries of the two samples shows that the general shape is the same, but the amplitude of the magnetic

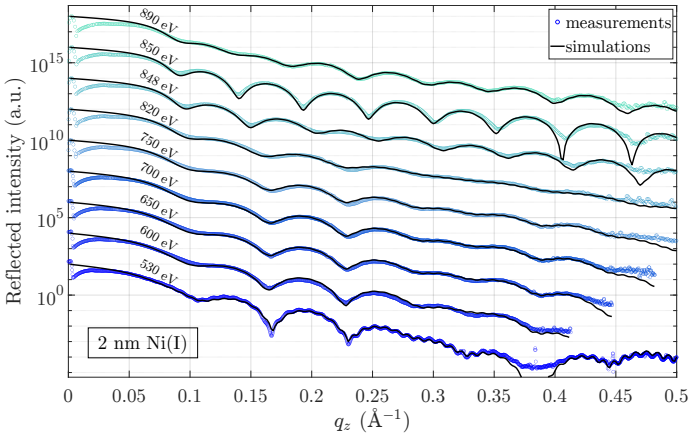

Figure 4.25: X-ray reflectivity measurements between 530 eV and 890 eV and the corresponding *ReMagX* fits for the 2 nm Ni(I) sample. For a better readability of the figure, measurements at different energies are plotted with a vertical offset.

asymmetry is smaller for 2 nm Ni(I). The region of further reduced magnetization which was found in the Fe and Co samples at the Fe/Cr and Co/Cr interface also exists for both Ni samples. Also the magnetization at the SiO_2/Ni interface is slightly reduced.

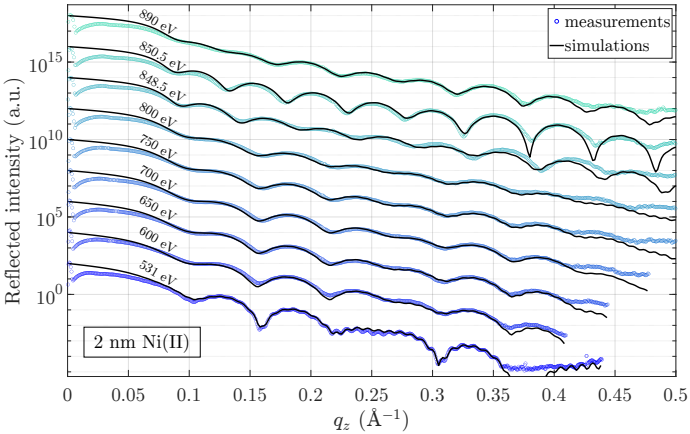

Figure 4.26: X-ray reflectivity measurements between 531 eV and 890 eV and the corresponding *ReMagX* fits for the 2 nm Ni(II) sample. For a better readability of the figure, measurements at different energies are plotted with a vertical offset.

Table 4.3: Structural parameters of the 2 nm Ni(I) and 2 nm Ni(II) samples determined from XRR measurements. The up and down arrows denote the roughness at the top and bottom interface of each layer.

	Layer	Thickness (nm)	Roughness (nm)	
Ni(I):	Au	8.3	↑ 0.27	↓ 0.43
	Cr	1.1	↑ 0.41	↓ 0.54
	Ni	1.9	↑ 0.56	↓ 0.24
	SiO_2	58.8	↑ 0.10	↓ 0.10
Ni(II):	Au	8.6	↑ 0.35	↓ 0.34
	Cr	1.4	↑ 0.23	↓ 0.54
	Ni	2.2	↑ 0.71	↓ 0.34
	SiO_2	59.3	↑ 0.36	↓ 0.10

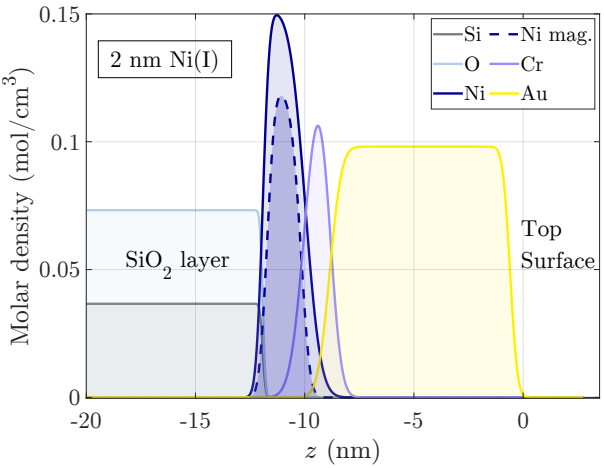

Figure 4.27: Chemical and magnetic depth profile of the 2 nm Ni(I) sample. The magnetic depth profile of the Ni layer is shown with the dashed blue line.

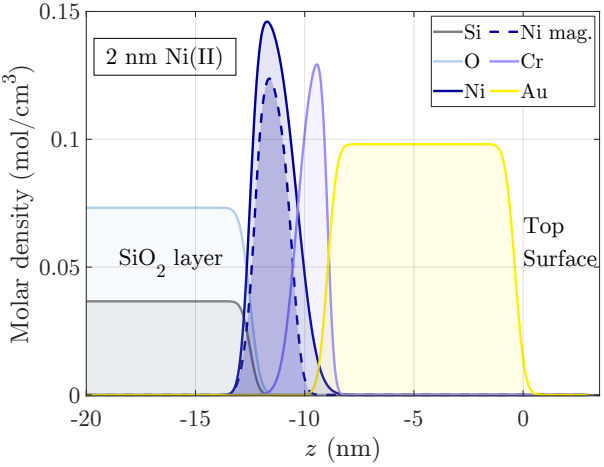

Figure 4.28: Chemical and magnetic depth profile of the 2 nm Ni(II) sample. The magnetic depth profile of the Ni layer is shown with the dashed blue line.

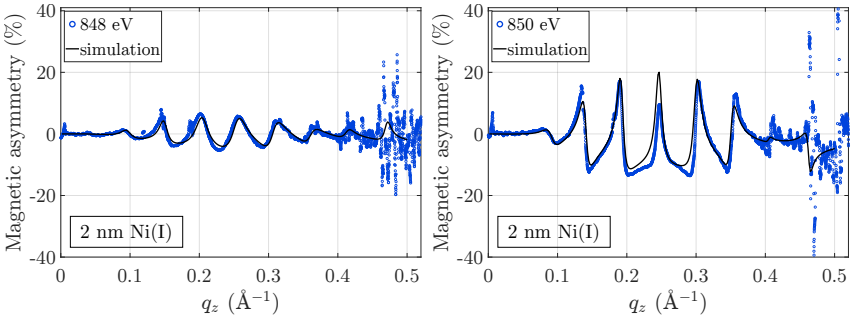

(a) **(b)**

Figure 4.29: Magnetic asymmetries measured at the 2 nm Ni(I) sample with photon energies (a) 2 eV before the maximum and (b) at the maximum of the Ni L_3-edge. The corresponding *ReMagX* fits are plotted in black.

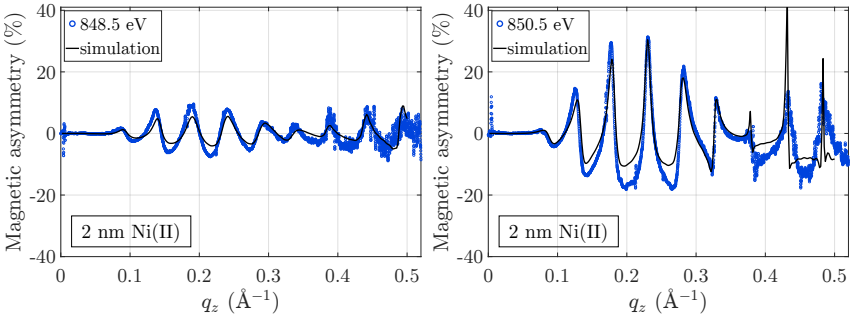

(a) **(b)**

Figure 4.30: Magnetic asymmetries measured at the 2 nm Ni(II) sample with photon energies (a) 2 eV before the maximum and (b) at the maximum of the Ni L_3-edge. The corresponding *ReMagX* fits are plotted in black.

4.4 Magnetometry Measurements – Quantification of Reduced Thin Layer Magnetizations

Temperature and field dependent SQUID measurements were performed at the exact same samples which were previously studied with XRR and XRMR and additionally at samples with a 10 nm thick TM layer instead of 2 nm. This allows the previously obtained magnetic depth profiles to be correlated with total magnetization measurements, thus quantifying the observed magnetization reductions. Temperature dependent magnetization measurements at samples with Fe, Co, and Ni as TM layer are shown in Fig 4.31. In the inset of Fig. 4.31a a full hysteresis loop at room temperature of the 2 nm Fe is plotted, which reveals that 117 mT is well enough to saturate the film.

By comparing the temperature dependent measurements of the thicker and thinner TM layers for Fe, Co, and Ni it becomes apparent that the magnetization decreases faster with temperature for the thinner samples. This behavior indicates that the 2 nm films have a lower effective Curie Temperature, thus the magnetization at room temperature is lower compared to thicker films or even bulk samples. A reduction of magnetization and Curie temperature for thin layers is not unexpected [63,64], since the magnetic ion coordination and related effective molecular exchange fields are reduced. It is not feasible to determine the actual Curie temperature of the samples by measuring the temperature dependent magnetization curves up to higher temperatures, as this would change the chemical structure and irreversibly alter the properties of the samples during the heating process.

From the chemical depth profiles, which were determined in section 4.3, and the known area of the samples, the exact number of TM atoms in the layers can be determined. Together with the temperature dependent

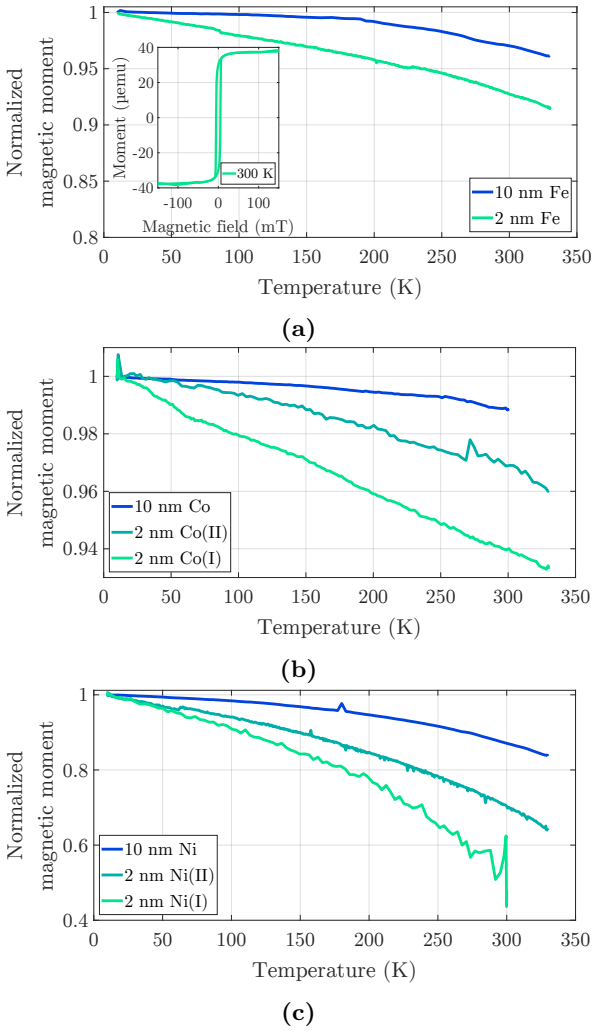

Figure 4.31: Temperature dependent magnetization measurements at samples with 10 nm and 2 nm thick (a) Fe, (b) Co, and (c) Ni layers. For all measurements an in-plane field of 117 mT was applied to saturate the samples. Each measurement is normalized to its measured magnetic moment at 10 K. The inset in (a) shows a full hysteresis loop at 300 K for the sample with a 2 nm Fe layer.

SQUID measurements this gives the opportunity to calculate the magnetic moment per TM atom at each temperature and compare the results to literature bulk values [91,92]. The measured saturation magnetization in μ_B/atom at 10 K and 300 K for each 2 nm sample is listed in table 4.4 together with the literature values. The last column of the table shows how much the saturation magnetization of each sample is reduced at room temperature when compared to literature bulk values. A comparison of the two Co samples shows that the magnetization of 2 nm Co(I) is more reduced than that of 2 nm Co(II). The same is true for the two Ni samples, where the magnetization of 2 nm Ni(I) is more reduced than that of 2 nm Ni(II). This confirms the results obtained from the magnetic depth profiles in sections 4.3.2 and 4.3.3, where the 2 nm Co(I) and 2 nm Ni(I) samples also showed a greater magnetization reduction.

The saturation magnetization values at 10 K for each sample still show a slight reduction on magnetization when compared with the literature bulk values. This originates most likely from the lower magnetic ion coordination and atomic intermixing at the interfaces. The magnetic depth profiles for each sample from section 4.3.1, 4.3.2 and 4.3.3 showed a region of strongly reduced magnetization at the TM/Cr interface.

Table 4.4: Measured saturation magnetic moment at 10 K and 300 K for 2 nm Fe, Co, and Ni films along with literature values according to [91,92], which are based on room temperature XMCD measurements. Together with the amount of magnetization reduction at 300 K retrieved from SQUID measurements when compared to the literature values.

	μ_B/atom			
Sample	10 K	300 K	lit. value	mag. reduct.
2 nm Fe	2.03	1.89	2.066	9 %
2 nm Co(I)	1.34	1.26	1.703	26 %
2 nm Co(II)	1.60	1.55	1.703	9 %
2 nm Ni(I)	0.36	0.19	0.570	67 %
2 nm Ni(II)	0.50	0.35	0.570	39 %

4.5 Discussion

In the previous sections, XRR, XRMR, and SQUID measurements were carried out on thin film systems. The samples consist of ferromagnetic TM layers with a nominal thickness of 2 nm, capped by Cr and Au layers with nominal thicknesses of 1 nm and 10 nm, respectively. They are sputtered onto a Si substrate with a thermally grown SiO_2 layer with a nominal thickness of 50 nm. The ferromagnetic TM layers were namely Fe, Co, and Ni. High resolution depth resolved elemental distribution profiles were retrieved from XRR measurements by fitting them with *ReMagX*. Those chemical depth profiles allow to determine the exact layer thicknesses and quantify the interface roughnesses. The extracted interface roughnesses consist of components related to local intermixing and long ranging roughnesses [157,158]. For the SiO_2 layers thicknesses of 58.8 – 59.3 nm were found, for the Cr layers 0.8 – 1.4 nm, and for the Au layers 7.9 – 8.7 nm. For the ferromagnetic TM layers a deviation of up to 0.4 nm from the nominal thickness was found, which is more than one lattice constant. The roughnesses at the various interfaces in the samples range from 0.10 nm to 0.73 nm, especially at the TM/Cr interfaces the roughnesses are relatively large with 0.44 – 0.73 nm. There are a multitude of studies on layered samples including ferromagnetic TM/Cr interfaces, which show similar roughnesses [159–162], but the final roughness in layered systems always depends on many parameters such as the used materials, the layer structure, the depositing method, and the roughness of the substrate. Especially, the Fe/Cr interface and its roughness received a lot of attention [163–165], since it was used for the discovery of the GMR effect [1,2].

The chemical and magnetic depth profiles shown in Figs. 4.13, 4.19, 4.20, 4.21, 4.27, and 4.28 reveal that the magnetization of the ferromagnetic TM layers at the SiO_2/TM interface is not reduced by the contact to the SiO_2 layer. The slight reduction at the SiO_2/Ni interface simply follows the total magnetic moment reduction due to the reduced effec-

tive Curie temperature, as indicated by the almost identical shape of the magnetic and chemical profiles. This is the first systematic study of interfacial magnetizations at buried SiO_2/TM interfaces. On the other hand, at the ferromagnetic TM/Cr interface, the magnetization of all investigated samples is significantly reduced and even vanishes completely in regions where TM and Cr seem to be strongly mixed. From the chemical depth profiles, the effective depth dependent TM/Cr alloy composition for each sample can be easily extracted. Dividing the magnetic and chemical depth profiles of the ferromagnetic TM layers gives the depth dependent normalized magnetic moment per TM atom, as it has been done previously in other XRMR studies [33]. Combining the two, results in the plots shown in Fig. 4.32, where the normalized magnetic moments per TM atoms are plotted as a function of TM concentration in the interfacial TM/Cr region. However, as mentioned above, the chemical depth profiles, obtained from XRR measurements do not allow to distinguish between local intermixing and roughness effects. The following is an attempt to distinguish between the two by comparing the observed magnetic moments for each TM/Cr ratio in the interface region with literature values of magnetic moments for bulk material of the respective alloys [166–168], also shown in Fig. 4.32.

In general the magnetic moment decreases with increasing Cr concentration in the interfacial region for all investigated samples as well as for the bulk alloy literature values. The magnetic moment in the 2 nm Fe sample is rather constant over a wide range of Cr concentration, similar to the literature values for FeCr alloys, and only starts to decrease significantly when the Fe concentration drops below 40 %. Band structure calculations for Fe/Cr interfaces performed by Uzdin et al. show that the saturation magnetic moment of interfacial Fe atoms is almost not reduced [169], which is consistent with the above observation. For the two 2 nm Co samples, the magnetic moment remains almost constant until the Co concentration in the interfacial region becomes less than 50 % for the Co(I) and 60 % for the Co(II) sample, respectively. The magnetic moment decreases continuously

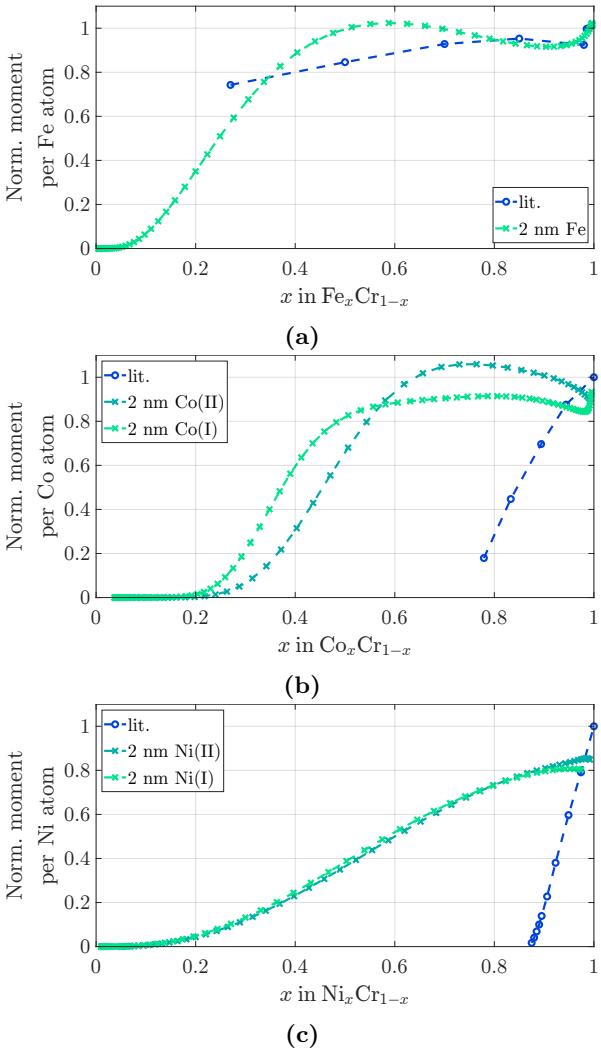

Figure 4.32: Normalized magnetic moment per TM atom in the TM/Cr interface region, where the two elements intermix, as a function of TM concentration for (a) the Fe sample, (b) the Co samples, and (c) the Ni samples. The plotted literature values for FeCr, CoCr, and NiCr bulk alloys are reproduced from [166–168].

for lower Co concentrations. Previous measurement results by Henry et al. at the Co/Cr interface also show a reduction of interfacial Co magnetization [170]. The magnetic moment in the two 2 nm Ni samples, Ni(I) and Ni(II), immediately starts to decrease when Cr is present in the interface region and decreases continuously with increasing Cr concentration. Band structure calculations for the Ni/Cr interface performed by Niklasson et al. show a strong decrease of the Ni magnetic moment when it is in contact with Cr [171]. The magnetic moment in the intermixing region vanishes for all investigated samples when the TM concentration decreases below 10 – 20 %. This region, where the magnetization vanishes, is not sufficient to explain the magnetization reduction, shown in table 4.4, that are obtained from SQUID measurements. The majority of the magnetization reduction originates most likely from the reduced effective Curie temperature, which is also visible in the magnetic depth profiles with the reduced density of the magnetic layer.

The comparison of the literature magnetic moments per TM atom in CoCr and NiCr bulk alloys with the magnetic moments of Co and Ni at the studied interfaces in Figs. 4.32b and 4.32c show a large differences. The magnetic moments of the bulk alloys decrease immediately when small amounts of Cr are present and drop to almost zero at Cr concentration of $\approx 25\,\%$ in CoCr and of $\approx 10\,\%$ in NiCr, while the magnetic moment stays constant over a wide range of Cr concentration for bulk FeCr. This indicates that the magnetic moments of Ni and Co are a lot more sensitive to the presence of Cr than the magnetic moment of Fe. Since the magnetic atoms in the studied samples obviously have a different coordination because of their thin layered structure compared to bulk samples it is not surprising that the studied samples do not behave like the bulk alloys. However, the strong difference between experimental and literature data in Fig. 4.32 might also indicate that ferromagnetic TM and Cr atoms are actually not that much intermixed as suggested by the chemical depth profiles. Since the lateral resolution of XRR is limited by the used x-ray

spot size, which in this study was approximately 900 µm, roughnesses on different length scales can not be distinguished [158]. Thus, the roughness retrieved from *ReMagX* simulations can be related to local intermixing on atomic length scales and long ranging roughness over up to several µm. The TEM image in Fig. 4.15 does show a longer ranging roughness that carries through all layers, which also indicates that the local interface might be sharper than the chemical depth profiles suggest at a first glance.

The detailed analysis of the chemical and magnetic depth profiles obtained from XRMR measurements, together with the complementary TEM measurement reveals that the roughness at the TM/Cr interface in the investigated samples is dominated by structural roughness instead of local intermixing. There is only a narrow region where the ferromagnetic TM atoms become non magnetic at the interface. Thus, the effect of the reduced magnetization of the ferromagnetic TM layers has to be dominated by the reduced effective Curie temperature.

4.6 Summary

In this chapter, the structural and magnetic properties of 2 nm thick magnetic TM layers that are sandwiched between SiO_2 and Cr were studied by means of XRR, XRMR, and SQUID magnetometry. Actual layer thicknesses and interface roughnesses were determined with high accuracy from reflectometry measurements and compared with results from TEM measurements. The magnetic depth profiles of the TM layers were obtained by fitting the measured XRMR data.

The results demonstrate that the thicknesses of the ion beam sputtered layers deviate significantly from the nominal thicknesses. For the magnetic TM layers, which are supposed to have a thickness of 2 nm, the difference is up to 0.4 nm (20 % of the nominal thickness). If this is not taken into account, when determining absolute saturation magnetizations from SQUID measurements it could introduce errors of the same magnitude. Large interface roughnesses are found, particularly at the TM/Cr interface, where it is up to 30 % of the layer thickness. The roughness at the TM/Cr interface is about twice that of the SiO_2/TM interface.

In general, the magnetic depth profiles of the TM layers follow the chemical depth profiles in all samples, but the magnetization of the whole layer is reduced. The amount of magnetization reduction was found to be extremely sensitive to tiny structural variations. With SQUID measurements the magnetization reduction was quantified to be up to 67 % when compared to bulk values from literature. Temperature dependent SQUID measurements showed that this magnetization reduction is mainly due to a reduced effective Curie temperature of the 2 nm magnetic TM layers.

The magnetic depth profiles show a marginal reduction in magnetization at the SiO_2/TM interface. However, at the TM/Cr interface the magnetization reduction is more significant. A detailed analysis of the chemical and magnetic depth profiles showed that the magnetic moment per TM atom decreases in the interfacial region, where TM and Cr are in

contact. With decreasing TM concentration in the interfacial region the magnetic moment per TM atom decreases, until it vanishes when the TM concentrations decreases below 10 – 20 %. However, this region, where the TM layers become non magnetic, plays a marginal role in the magnetization reduction of the whole layer. A comparison of the magnetization dependence in bulk alloys on the TM/Cr ratio (from literature) with the magnetization dependence in the interfacial region on the TM/Cr ratio (determined from XRMR measurements) reveals that a large part of the observed interfacial roughness is based on structural contributions, with only a narrow intermixing region.

The insight into thin film magnetic systems gained in this chapter by means of XRR, XRMR, and SQUID measurements is essential for a fundamental understanding of the magnetic properties in such thin film systems and in particular of the interfacial magnetism. This knowledge could help to design new spintronic devices and improve the functionality of existing ones. The accurate knowledge of the chemical and magnetic depth profiles is also necessary in order to properly analyze the VXRR data in the following chapter.

Experimental Part III

Chapter 5

Voltage X-Ray Reflectometry: A Method to Study Electric-Field-Induced Changes in Interfacial Electronic Structures

The experimental realization of voltage x-ray reflectometry (VXRR) measurements as well as the development of a scheme to simulate VXRR data with *ReMagX* was the central goal of this thesis. The method of VXRR and first experimental results have been recently published [172]. Details about the experimental realization, processing and interpretation of VXRR data, and the very first experimental results are shown in this chapter. This measurement method allows for the first time to retrieve element-specific information about voltage related changes in the interfacial electronic structure at buried oxide/metal interfaces.

At the beginning of the chapter, an introduction to electric-field-induced effects in thin magnetic layers is given. Then, the modifications to the hardware and software of ERNSt that were necessary to enable interface

sensitive, element-specific VXRR measurements are described. The preliminary electrical characterization of the phase and amplitude responses of the experimental setup, which was needed before first actual measurements were possible, are shown. A detailed step by step explanation is given of how a final measurement point is retrieved from raw data and how measurement data are simulated with *ReMagX*. The measurement results for Ni[172] and O atoms at the interface are presented and discussed together with the *ReMagX* simulation results.

5.1 Introduction

Electric-field-induced effects at buried interfaces in multilayered systems play an important role for modern technology. In devices such as spintronic tunnel junctions, MOS-FETs, capacitors, solid-state electrolyte lithium batteries, and in general all kind multilayered systems including an insulating layer, electric-field-induced effects at interfaces play an important role. One prominent example for such an effect is the voltage control of magnetic anisotropy (VCMA), which is interesting to study from both a technological and a fundamental research point of view, since it is well established in various technological applications but a thorough understanding of the microscopic origin from the electronic structure is still missing. First experimental reports of the electric field control of ferromagnetism date back to the early 2000s[173–175] and the first observation of VCMA in 3d transition ferromagnetic layers was reported in 2007[176]. Utilizing the VCMA effect in spintronic devices offers the possibility for magnetization switching with a much higher energy efficiency compared to switching with magnetic fields or via STT. This way the power consumption of such devices can be reduced drastically, which has been shown in several studies, and first designs to include this effect in technological devices have been

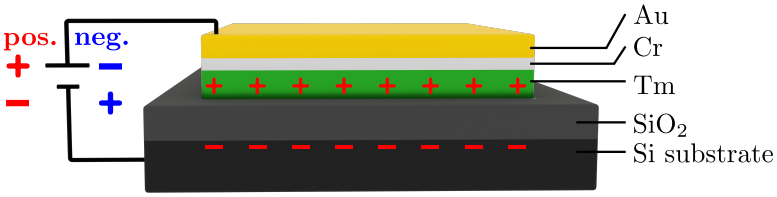

Figure 5.1: Schematic of the sample design for VXRR measurements throughout this chapter. The orientation of a positive (negative) voltage is shown in red (blue). For a positive voltage holes accumulate at the TM/SiO_2 and electrons at the SiO_2/Si interface.

proposed [25,112,113,177]. As mentioned before, a complete description of the origin of the effect is still missing and especially experimental evidence for theoretical models is lacking. A first theoretical approach to explain the underlying physics of the VCMA effect was proposed by Bruno in 1989 [69]. Since then, numerous theoretical studies have been conducted to further improve our understanding of this phenomenon [178–182]. Direct experimental evidence for the proposed models, however, still remains elusive. The main reason for this is the scarcity of experimental techniques that can yield information about buried interfaces.

First attempts to directly measure electric-field-induced changes to the XAS and XMCD signal of iron at the L_2 and L_3-edges were carried out by Miwa et al. in 2015 [105]. Since no voltage-induced change to the spectrum was measurable they estimated the effect to be less than 1.2 %. After modifications to their experimental set-up, they successfully measured voltage-induced changes to the amplitude of the XMCD signal in Ni, Co and Fe thin films at the L_2 and L_3-edges of those materials [106–108]. For Pt/Fe multilayers they were able to measure a spectrum of the electric-field-induced changes at the Pt L-edge [183]. But full spectra of the electric-

field-induced changes for 3d transition metals are still missing.

XRR and XRMR measurements are sensitive to exactly the information needed to study interfacial voltage effects. Precise chemical and magnetic depth profiles of layered samples can be retrieved, including exact layer thicknesses, interface roughnesses and magnetic properties of buried layers (see chapter 4). In order to advance XRR to VXRR, an electric field is applied across a layered sample with a TM layer in contact with SiO_2 as an insulating layer. The same samples as in the previous chapter will be studied in this chapter. The exact knowledge of the chemical and magnetic depth profile of these samples, determined in the previous chapter, is a prerequisite for the analysis of VXRR data. The sample design and the orientation of the applied electric field is shown in Fig. 5.1. Electrons are pushed (pulled) to (from) the TM/SiO_2 interface and populate (depopulate) states of atoms at the interface. This changes the x-ray optical properties slightly, and hence the measured reflected x-ray intensity changes. The change in reflected x-ray intensity is the voltage-induced signal that will be measured in this chapter, and retrieving the electric-field-induced change in x-ray optical properties Δf_1^{V} and Δf_2^{V} from these measurements is the main purpose of VXRR. Δf_1^{V} and Δf_2^{V} are directly related to the change in electronic structure of the atoms affected by the electric field. A schematic and, for better visibility, exaggerated representation of the voltage-induced changes of the atomic scattering factor f_2 is shown in Fig. 5.2. The voltage x-ray optical properties Δf_1^{V} and Δf_2^{V} are the voltage dependent analogues of the magnetic components of the x-ray optical properties $\Delta f_1^{\mathrm{mag}}$ and $\Delta f_2^{\mathrm{mag}}$.

The white line intensity of transition metal L-edges is proportional to the number of 3d holes[56,79] and hence this intensity will change slightly when the occupation of 3d states at the interface is changed by means of an electrical field. This changes the resonant x-ray optical properties and therefore the (de)population of interfacial states determines the strength

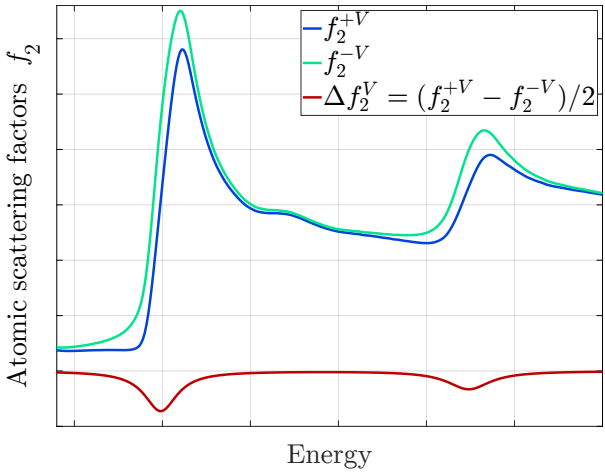

Figure 5.2: A schematic of the electric-field-induced changes to the atomic scattering factor f_2 together with the corresponding difference $\Delta f_{2,V}$.

of the measured signal. A rough estimate of the expected signal strength for TMs can be made by calculating the electric-field-induced change of 3d holes and divide this by the number of TM atoms present at the interface. For a sample with Ni as TM layer, an insulating layer SiO_2 of $d = 50\,\text{nm}$ thickness with an ϵ_r of 3.9[184], and an applied voltage of $U = \pm 12\,\text{V}$, the maximum change of 3d holes per area at the interface Δn_h can be calculated via the number of moved electrons per area N_{e^-}. The number of moved electrons per area N_{e^-} can be calculated via:

$$N_{\text{e}^-} = \frac{D}{e} = \frac{\epsilon_0 \epsilon_\text{r}}{e} E, \tag{5.1}$$

with the electric displacement field D, the elementary charge e, the vacuum and relative permittivity ϵ_0 and ϵ_r, respectively, and the electric field E that is given by[185]:

$$E = \frac{U}{d}, \tag{5.2}$$

since the sample resembles a plate capacitor. With this, the maximum change of 3d holes per area at the interface Δn_h when changing the voltage from $-U$ to $+U$ can be calculated:

$$\Delta n_\mathrm{h} = 2N_{\mathrm{e}^-} = \frac{2U\epsilon_\mathrm{r}\epsilon_0}{ed} = 1.03 \cdot 10^{17}\,\frac{1}{\mathrm{m}^2}, \tag{5.3}$$

The face-centered cubic unit cell of Ni has a lattice constant of $a_0 = 352.4\,\mathrm{pm}$ [186], where two Ni atoms are within an area of a_0^2. This results in a Ni area density at the interface of

$$\rho_\mathrm{Ni} = \frac{2}{a_0^2} = 1.61 \cdot 10^{19}\,\frac{\mathrm{Ni}}{\mathrm{m}^2}. \tag{5.4}$$

A rough estimate of the expected magnitude of the voltage-induced measurement signal is then the ratio of Δn_h and ρ_Ni, which represents the electric-field-induced change of 3d holes per interfacial Ni atom:

$$\Delta n_\mathrm{h,Ni} = \frac{\Delta n_\mathrm{h}}{\rho_\mathrm{Ni}} = 0.0064\,\frac{1}{\mathrm{Ni}}. \tag{5.5}$$

So the signal is expected to be in the low ‰ region, which makes it necessary to implement a lock-in based measurement setup for the voltage-induced signal. This experimental setup is explained in section 5.2.1.

5.2 Experimental Methods

5.2.1 Modifications to ERNSt for Voltage-Induced Measurements

A lock-in setup to measure the electric-field-induced intensity changes of reflected x-rays had to be implemented in ERNSt as the signal is expected to be in the low ‰ range, as described above. An alternating voltage is applied to the samples in the reflectometer which moves electrons away from (towards) the TM/SiO_2 interface, respectively, which results in slight changes of the x-ray optical properties and consequently changes of the reflected x-ray intensity. These changes oscillate with the same frequency as the applied electrical field. Thus the amplitude and phase response of the whole experimental setup needs to be known before the actual experiments are carried out at the synchrotron.

A *Keithley 6517B Electrometer* is used to measure the photocurrent of the reflectometry detector (a *Hamamatsu* GaAsP photodiode (*G1116* type)). Since the electrometer is not built to measure AC, but rather DC signals, the amplitude and phase response in the different sensitivity ranges (200 µA, 200 nA, and 200 pA) has to be determined. For this, the alternating voltage of the reference signal of the *SR 830 Lock-In Amplifier* is scaled down with a voltage divider and with an appropriate resistance, an alternating current within the respective range (200 µA, 200 nA, or 200 pA) is fed to the electrometer. The *PREAMP OUT* signal of the electrometer is then fed to the lock-in to measure the amplitude and phase of the signal, which is shown in Fig. 5.3. The three ranges show different cut-off frequencies, namely 0.07 Hz, 80 Hz, and 700 Hz for the pA, nA, and µA-range, respectively. The amplitude and phase response shown in Fig. 5.3 is only the response of the *Keithley 6517B Electrometer*, however, in the real experiment, the measured current comes from a photodiode and has

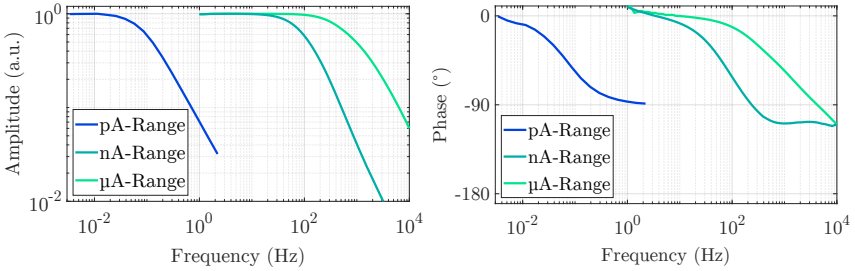

(a) **(b)**

Figure 5.3: Amplitude (a) and phase (b) response of the *Keithley 6517B Electrometer* when an AC signal is measured with the 200 µA, 200 nA, and 200 pA-range, respectively.

a DC offset from the total reflected x-ray intensity. A DC driven light-emitting diode (LED) with its intensity modulated by a small AC signal is used in order to simulate a realistic measurement signal in the laboratory without actually using x-rays. The visible light emitted by the LED illuminates the reflectometry detector while the AC frequency is tuned from 1 Hz to 2000 Hz. The intensity of the LED is controlled by the DC voltage and tuned in a way that the photocurrent has a suitable value for the different measurement ranges of the electrometer. Figure 5.4a and 5.4b show the amplitude and phase response of the full experimental setup (photodiode and electrometer serially connected), as it is used at the synchrotron. The measurements show the typical response of a damped harmonic oscillator for all three measurement ranges, due to an internal electric resonance. The resonance is most pronounced in the nA-range, where the amplitude has a maximum at 59 Hz with a phase of $-70°$. Typical photocurrents measured with ERNSt on the samples in this thesis lie between 10 nA and 10 pA. Thus, the µA-range of the electrometer is not suitable. The pA-range on the other hand has a cut-off frequency around 2 Hz, which is too low for optimal lock-in performance. Hence, the lock-in frequency of choice for the experiments at the synchrotron is 59 Hz, and the electrometer range

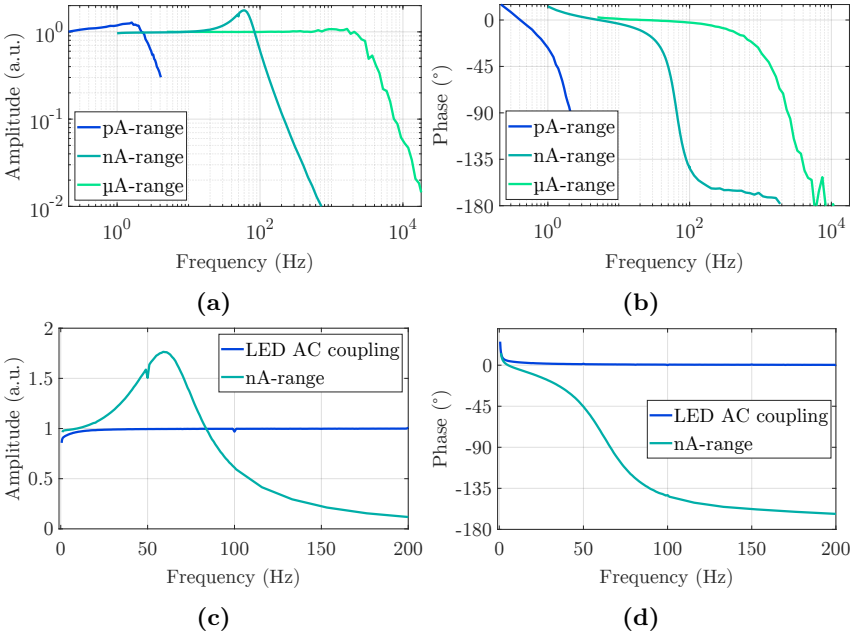

Figure 5.4: Amplitude (a) and phase (b) response of the experimental setup when an AC signal is measured with the 200 µA, 200 nA, and 200 pA-range, respectively. In (c) and (d) a zoom-in on the resonance for the 200 nA-range is shown, together with the response of the electric circuit used to couple the AC into the LED. The electric circuit used to drive the LED does not provide an additional amplitude or phase variation.

is fixed to 200 nA. In Fig. 5.4c and 5.4d a zoom-in of the amplitude and phase response between 1 Hz and 200 Hz of the experimental setup in the nA-range is shown, together with the amplitude and phase response of the voltage in the electric circuit used to drive the LED. The response of the LED-AC coupling is examined to make sure that there is no additional amplitude or phase variation coming from this part of the electrical setup. At the maximum of the resonance (59 Hz), the amplitude of the signal is increased by a factor of 1.76. Any measured VXRR signal, measured at this frequency has and will be corrected by this factor. In appendix A, it

is shown that the amplitude of a real VXRR measurement signal indeed follows the same frequency dependence as measured here.

In the 200 nA-range the *PREAMP OUT* output of the electrometer provides 1 V per 1 nA. Since the *SR 830 Lock-In Amplifier* tolerates only 50 V at the input, a 1 µF capacitor is put at the input, which, together with the 10 MΩ input impedance of the amplifier, acts as a high-pass filter with a cutoff frequency of 0.016 Hz. This way, the DC component of the signal which results from the reflected x-ray intensity can be blocked from the lock-in. The maximum output voltage of the lock-in is $5\,V_{rms}$. In order to apply higher voltages than that in the experiment, a *HP 6826 A Bipolar Power Supply/Amplifier* was used. The default *SR 830 Lock-In Amplifier* settings for electric field dependent reflectivity measurements are the following:

- 1 µF capacitor at the lock-in signal input.
- Reference frequency of 59 Hz and a predefined phase of $-70°$.
- A time constant of 300 ms.
- The sensitivity is set to 100 mV and the reserve to normal.
- The signal input is set to float and AC coupled.
- No line filter is used.

The amplitude of the noise measured with the lock-in with the described settings and the LED as a light source is around $0.04 - 0.05\,pA_{rms}$.

The experimental control software of ERNSt is written in *LabVIEW*. In the context of this thesis, the control software was complemented by scripts that control the lock-in amplifier and read out measured data automatically.

Measurement Procedure for Voltage-Induced Measurements

In order to measure the voltage asymmetry A_V, an alternating electric field has to be applied to a sample. Figure 5.5a shows the bottom of the sample manipulator of ERNSt with an omicron sample holder (without sample) and the copper contact which is used to guide the electric field to the sample [187]. The copper contact is electrically isolated from the sample manipulator. An image of a sample prepared for VXRR measurements on an omicron sample holder is shown in Fig. 5.5b. When sliding the sample holder into the sample manipulator, the copper clad laminate (CCL) wedge will close the contact with the copper contact. The copper wire connects the top of the sample to the applied electric field, while the bottom of the sample is connected to ground via the omicron sample holder and the sample manipulator.

The averaged reflected x-ray intensity I is measured in the same way as for regular XRR and XRMR measurements, with the detector for specular reflection. However, the intensity variations that are induced by the electric field are measured with the lock-in. The resulting voltage asymmetry ratio A_V is calculated via [172]

$$A_\mathrm{V} = \frac{I_{V+} - I_{V-}}{I_{V+} + I_{V-}} = \frac{I_\text{lock-in}}{2I}, \tag{5.6}$$

where I_{V+}, and I_{V-} are the reflected x-ray intensities with positive and negative applied voltage, respectively. The difference of these two intensities is the measured lock-in signal $I_\text{lock-in}$, and their sum is the same as two times the averaged measured reflected intensity I.

There are two different measurement modes for VXRR. The constant energy mode, where the energy is kept fix and the angle Θ, and therefor q_z, is swept, and the constant q_z mode, where q_z is kept constant and energy and angle are swept synchronously in order to maintain a constant

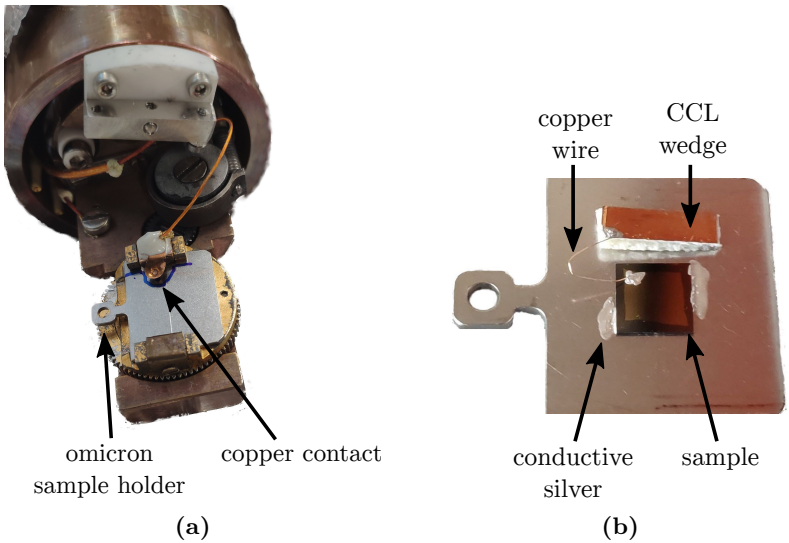

Figure 5.5: (a) Bottom of the sample manipulator of ERNSt with the copper contact for VXRR measurements and an omicron sample holder without sample. (b) Omicron sample holder with a sample for VXRR measurements mounted. The single-sided CCL wedge together with the copper wire serve to contact the top of the sample with the copper contact of the sample manipulator and hence to the voltage source[187]. The conductive silver contacts the bottom of the sample with the omicron sample holder and hence with ground.

q_z. For each data point of a voltage asymmetry measurement, the incoming x-ray intensity I_0, the reflected intensity I_{Det}, and the lock-in signal is measured over a time period of 10 s and then averaged, with 3 s delay time between neighboring data points. Figures 5.6a and 5.6b show the reflected intensity I_{Det} and the voltage signal, respectively, of a typical constant q_z measurement. In Figs. 5.6c and 5.6d, the raw data of the x-ray intensity reference I_0 and the voltage signal are shown, which give rise to the data points marked with the red cross. The down spike in I_0 arises from an unavoidable injection of electrons in the electron storage ring BESSY II. This

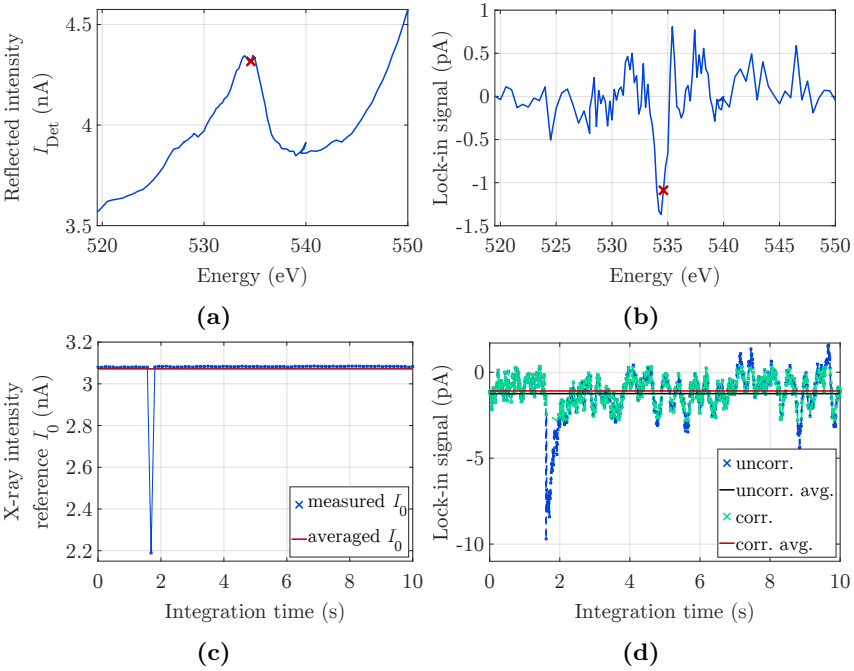

Figure 5.6: (a) and (b) show the reflected x-ray intensity and voltage signal, respectively, of a typical constant q_z scan. (c) and (d) display the measured I_0 and lock-in raw data, respectively, within the 10 s integration interval for the data point marked with a red cross in (a) and (b). In (c) the uncorrected and corrected raw data with the corresponding average values are shown.

short drop of incoming x-ray intensity disturbs the lock-in measurement, which can be seen in Fig. 5.6d. In the normal top-up mode, these injections occur approximately every 90 s, thus roughly every 7th data point will be affected by this event. In order to correct for this effect, a software-based noise filter is implemented. The filter calculates the standard deviation of the lock-in raw data within the 10 s integration interval. In a next step, all data points whithin the integration interval that are more than 1.3 times the standard deviation away from the uncorrected average will be

ignored for averaging. In Fig. 5.6d, the corrected and uncorrected lock-in raw data and averages are shown. In order to further reduce the noise, each measurement is then repeated up to 14 times, depending on the signal strength, the desired accuracy of the measurement, and also the available measurement time.

The routines for the different VXRR measurement modes were written in *LabVIEW* and integrated to the ERNSt control software.

5.2.2 Processing Voltage X-Ray Reflectometry Data

The fitting of voltage asymmetries follows a similar scheme as fitting magnetic asymmetries, which is described in section 4.2.4. After the regular fitting procedure, an artificial layer is introduced, which represents the interfacial region that is affected by the applied electric field. This layer will be referred to as the *voltage layer* from now on. Since the technique of VXRR studies the effect of populating and depopulating of interfacial states with charges that are moved to the interface by an electric field, the voltage layer has to be located at interfaces where an electrical insulator is at one side of the interface. However, the exact location, width and density of this layer are potentially free parameters for the voltage asymmetry fit. Physically meaningful boundaries for those parameters are automatically given by the interface roughness and chemical depth profiles retrieved from XRR measurements.

The important difference between fitting a voltage asymmetry and a magnetic asymmetry is that voltage x-ray optical parameters are unknown and cannot be measured in advance (unlike the magnetic x-ray optical parameters, which can be determined with XMCD measurements). Quite the opposite, in fact one of the main goals of VXRR measurements is to retrieve those voltage x-ray optical parameters. Thus, they are free parameters for the fit. In order to fit voltage asymmetries measured in

constant energy mode, where the energy is kept fix and the angle Θ, and therefor q_z, is swept, Δf_1^V and Δf_2^V can be fitted completely freely and independently of each other. This is not the case when fitting voltage asymmetries measured in constant q_z mode, where q_z is kept constant and the energy is swept, since Δf_1^V and Δf_2^V are not constant, but energy dependent. Thus, they need to be fitted as a function of energy. Furthermore, Δf_1^V and Δf_2^V are not independent of each other but are related via Kramers-Kronig relations. Therefore, Lorentzian functions are used to model Δf_1^V and Δf_2^V. In the following analytical form, Δf_1^V and Δf_2^V are always Kramers-Kronig related, which has the advantage that Δf_1^V does not have to be calculated from Δf_2^V via the Kramers-Kronig relation or vice versa[188]:

$$\Delta f_1^{\mathrm{V}}(E) = \frac{\alpha E^2(E^2 - E_0^2)}{(E_0^2 - E^2)^2 + \beta^2 E^2} \tag{5.7}$$

$$\Delta f_2^{\mathrm{V}}(E) = \frac{\alpha\beta E^3}{(E_0^2 - E^2)^2 + \beta^2 E^2}. \tag{5.8}$$

Here, E_0 is the energy position, α the amplitude, and β the width of the Lorentzian functions. Those three are also the free fit parameters in order to fit voltage asymmetries measured in constant q_z mode. Values of Δf_1^{V} and Δf_2^{V}, which were retrieved from constant energy fits, can be used as a guide, since the energy dependent voltage optical parameters should include those points. Usually a superposition of up to four Lorentzian curves is used to model the voltage x-ray optical parameter Δf_1^{V} and Δf_2^{V}.

5.2.3 Sample Preparation

The samples studied in this chapter are the same samples which were studied in chapter 4. Thus, a description of the sample preparation can

be found in section 4.2.7. The marker pen lithography [156] described there was used in order to prevent an electrical connection between the sputtered layers and the Si substrate, since for VXRR measurements the voltage needs to drop at the capacitor consisting of the Si/SiO_2/TM stack (see Fig. 5.1). In preparation of VXRR measurements with ERNSt, a copper clad laminate (CCL) wedge is glued to a omicron sample holder. Since the CCL is one-sided, there is no electrical contact between the top of the wedge and the sample holder. Then a sample is glued to the sample holder (see Fig. 5.5b) with conductive silver paint. The conductive silver ensures a good electrical contact between the omicron sample holder and the Si substrate. Using a copper wire and conductive silver paint, the CCL wedge and the top Au layer of the sample are then electrically contacted. When sliding the sample holder into the sample manipulator of ERNSt, the CCL wedge will contact with the copper contact (see Fig. 5.5), which in turn is connected to the AC voltage source.

5.3 Sample Pre-Characterization

The exact structure, i.e. layer thicknesses, interface roughnesses, and magnetic depth profiles are required in order to analyze and simulate VXRR measurements with *ReMagX*. Again, due to the fact that the same samples are used throughout chapter 4 and 5, the corresponding structural details can be found in section 4.3.

5.3.1 Breakdown Voltages

A sufficient breakdown voltage of the SiO_2 layer is crucial for the success of VXRR experiments, since the measured signal will be higher when the

(a) **(b)**

Figure 5.7: (a) Si substrate with SiO_2 coating with conductive silver droplets as contacts in order to determine the breakdown voltage of the SiO_2 layer at various positions. (b) Sample holder which was designed to contact the studied samples and measure their resistive properties.

applied electric field is higher. As a first test, the break down voltage of the blank wafer with the (50 ± 30) nm thermally oxidized SiO_2 layer was tested. In order to do that, conductive silver paint droplets were put onto the surface as a contact (see Fig. 5.7a). They were then contacted with needles from a probe station setup, and a DC voltage was applied to the sample, where breakdown voltages between 37 V and 62 V were found. The large distribution of breakdown voltages can be attributed to the uncertainty in SiO_2 thickness as well as the difficulties in contacting the sample with the needles.

In a next step, gold contacts were sputtered on top of the SiO_2 interface, the samples glued to an omicron sample and contacted in the same way as for VXRR measurements (see section 5.2.3). A sample holder, similar to the one used in ERNSt (see Fig. 5.5a), was designed and can be seen in Fig. 5.7b. A DC voltage was then applied to the gold contacts. When applying only 1 mV, some of the samples showed initially a relatively low

resistance of $\sim 1\,\mathrm{k\Omega}$. However, after applying a short 10 V pulse without a current limit the resistance usually increased to $\sim 1\,\mathrm{M\Omega}$, seemingly burning through weak spots. Those gold contact samples showed breakdown voltages between 15 V and 27 V.

First VXRR measurements showed that for the present sample design, voltages of at least $10-12\,\mathrm{V_{rms}}$ are needed for a reasonable signal strength. The previous breakdown voltage measurements showed that the distribution among different samples is rather high and some samples might already break down at voltages too low for reasonable VXRR measurements. Thus, in preparation for beamtime, each sample was produced at least 4 times to make sure that at least one sample does not break down below $10\,\mathrm{V_{rms}}$. The resistance to an applied voltage of those samples was tested under the same conditions as the final VXRR measurement, i.e. an AC voltage with 59 Hz. Each sample was tested whether it could withstand a voltage of and $10\,\mathrm{V_{rms}}$. When more than one sample of a set survived, higher voltages (up to $15\,\mathrm{V_{rms}}$) were tested. This procedure ensured that only samples capable of withstanding voltages high enough to provide VXRR signals of reasonable strength were taken to beamtime.

5.3.2 Capacitance and Relative Permittivity

Having a look at the sample design in Fig. 5.1, it becomes obvious that it resembles a parallel-plate capacitor with the sputtered metallic layers and silicon substrate as top and bottom plate, respectively, separated by the insulating SiO_2 layer which acts as dielectric. The capacitance C of a plate capacitor is given by[185]:

$$C = \epsilon_0 \epsilon_\mathrm{r} \frac{A}{d}, \tag{5.9}$$

with the area A, the thickness of the insulating layer d, and the vacuum and relative permittivity ϵ_0 and ϵ_r, respectively. The area A of the sample can be retrieved from images, and the thickness d of the insulating layer was retrieved from XRR measurements in chapter 4. The relative permittivity ϵ_r can be determined after measuring the capacitance C, which was done in three different ways:

- Direct measurement of the capacitance with an *Amprobe AM 530 EUR multimeter*.
- AC current measurement through sample at different frequencies and calculating the capacitance from the impedance.
- Building an oscillating circuit with a known inductance and the sample as capacitance. By fitting the measured frequency response and comparing it to the model of a simple LRC circuit, the capacitance can be retrieved.

The corresponding results for the 2 nm Ni(II) sample are listed in table 5.1. Including the samples that were studied in chapter 4, an averaged value of $\epsilon_r = 3.88$ is determined, which is in good agreement with literature values of ϵ_r that lie between 3.7 and 3.9 [184,189]. With the thickness of the SiO_2 layer, the applied AC voltage U_{rms}, and the relative permittivity ϵ_r, the electric field E_{rms} and the electric displacement field D_{rms} can be calculated via:

$$E_{rms} = \frac{U_{rms}}{d} \tag{5.10}$$

$$D_{rms} = \epsilon_0 \epsilon_r E_{rms} = \frac{\epsilon_0 \epsilon_r U_{rms}}{d}. \tag{5.11}$$

The electric displacement field D_{rms} is a measure for the charge accumulating at the SiO_2 interface under the applied electric field E_{rms}. Dividing it by the elementary charge e gives the number of electrons per area accumulating at the interface.

Table 5.1: Measured capacitance (with three different methods) of the 2 nm Ni(II) sample and the resulting relative permittivity ϵ_{r}.

Sample	capacitance in nF measured via			resulting ϵ_{r}
	multimeter	impedance	oscillating circuit	
2 nm Ni(II)	5.19	5.16	5.29	3.96 ± 0.06

5.4 VXRR Measurements – Interfacial Electric-Field-Induced Effects

The experimental realization of VXRR measurements as well as the development of a scheme to simulate VXRR data with *ReMagX* was the central goal of this thesis. In this section, the very first experimental VXRR data, the corresponding analysis and the interpretation of the data is presented. Figure 5.8 shows a schematic of the measurement geometry. VXRR measurements at the Ni L_3-edge on a sample with Ni as a magnetic TM layer are presented [172], as well as measurements at the O K-edge on samples with different elements at the SiO_2 interface.

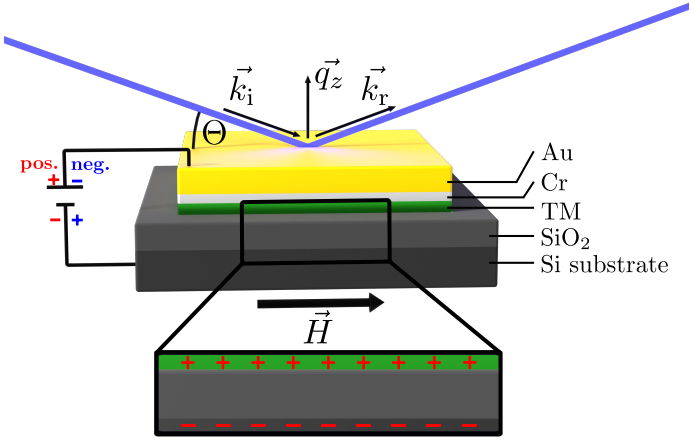

Figure 5.8: Schematic of the sample design and measurement geometry for VXRR measurements. The incident and reflected x-rays are shown in blue with the wave vectors $\vec{k}_i$ and $\vec{k}_r$, respectively. The momentum transfer $\vec{q}_z$ is defined as the difference between $\vec{k}_r$ and $\vec{k}_i$. A magnetic field $\vec{H}$ is applied parallel to the plane of incidence and the sample surface. The electric field is applied perpendicular to the layer stack with the Au layer and the Si substrate acting as contacts. Charges accumulate at the Si/SiO_2 and SiO_2/TM interfaces.

5.4.1 Voltage Effect for Interfacial Nickel Atoms

The structural parameters as well as the chemical and magnetic depth profiles of the 2 nm Ni(II) sample, which is studied in this section, were determined in chapter 4 and can be found in table 4.3 and Fig. 4.28, respectively. For all measurements, an AC voltage of $U_{\mathrm{rms}} = 12\,\mathrm{V}$ is applied to the sample and with the 59.3 nm thick SiO_2 layer, using equation 5.10, this corresponds to an electric field of $E_{\mathrm{rms}} = 0.2\,\frac{\mathrm{V}}{\mathrm{nm}}$. Using the averaged relative permittivity $\epsilon_{\mathrm{r}} = 3.88$ from section 5.3.2, the displacement field D_{rms} is calculated using equation 5.11 to be $D_{\mathrm{rms}} = 0.007\,\frac{\mathrm{C}}{\mathrm{m}^2}$, which represents (when divided by the elementary charge e) the number of electrons per area moved by the electric field $N_{\mathrm{e}^-} = 4.34 \cdot 10^{16}\,\frac{\mathrm{e}^-}{\mathrm{m}^2}$ (or alternatively in units of $\frac{\mathrm{mol}}{\mathrm{cm}^2}$: $N_{\mathrm{e}^-} = 7.21 \cdot 10^{-12}\,\frac{\mathrm{mol}}{\mathrm{cm}^2}$).

Constant Energy q_z-Scans

Figures 5.9 and 5.10 show constant energy q_z-scans of the electric-field-induced variations of reflected x-ray intensity measured at 849.8 eV (which is at the onset of the Ni L_3-edge) and 850.5 eV (which is at the maximum of the Ni L_3-edge), respectively (see Fig. 3.9a). The shown data measured at 849.8 eV and 850.5 eV are obtained by averaging over 8 and 2 repeated measurements, respectively. The voltage asymmetry ratio A_{V}, shown in the right column of the figures, is calculated via equation 5.6. The left column shows the measured lock-in signal $I_{\text{lock-in}}$, which is the difference in measured photo current when the electric field is switched from positive to negative. The top and bottom row of the figures show measurements with antiparallel and parallel orientation of sample magnetization and photon helicity, respectively. The voltage asymmetry ratio A_{V} is, as expected, in the low ‰ range and does not exceed 0.5 ‰ within the measured range (see Figs. 5.10b, 5.10d, 5.9b and 5.9d). The actual measured reflected photo

current difference $I_{\text{lock-in}}$ between positive and negative applied voltage is lower than 0.5 pA for low q_z values and decreases quickly with increasing q_z (see Figs. 5.10a, 5.10c, 5.9a and 5.9c). Similar to magnetic asymmetries A_{mag} (see chapter 4) the voltage asymmetry ratio A_{V} increases with increasing q_z because the reflected intensity I decreases faster with q_z than $I_{\text{lock-in}}$. The voltage asymmetry ratios measured at the onset of the Ni L_3-edge have a higher amplitude than the voltage asymmetry ratios measured at the maximum of the Ni L_3-edge. The black lines in Figs. 5.9 and 5.10 show the *ReMagX* simulation results, which are in good agreement with the measurements. The details of these simulations will be explained later.

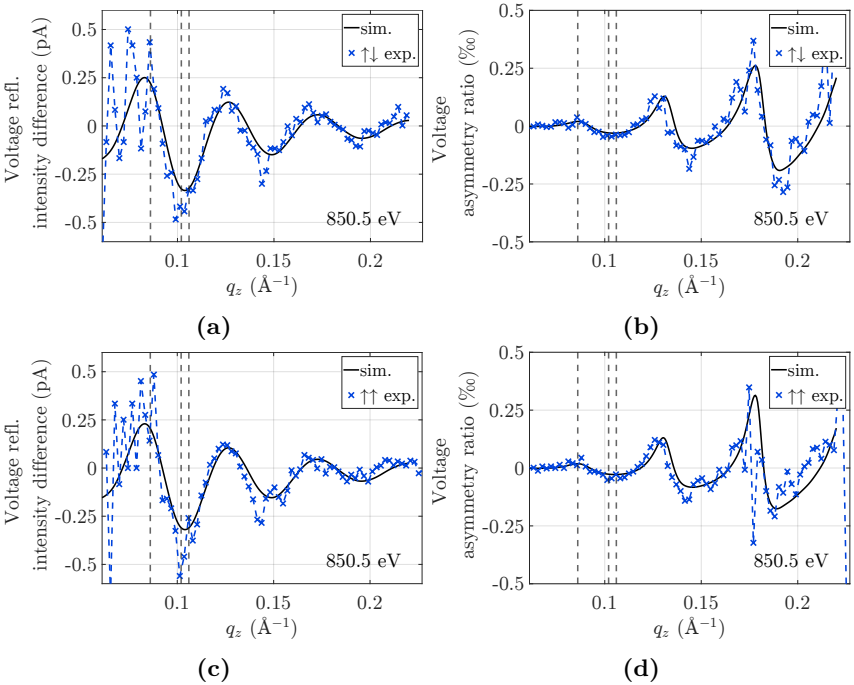

Figure 5.9: VXRR constant energy q_z-scans at 850.5 eV, which is at the maximum of the Ni L_3-edge. (a) and (c) show the difference in reflected photo current $I_{\text{lock-in}}$ between positive and negative applied voltage for antiparallel and parallel configuration of sample magnetization and photon helicity, respectively. (b) and (d) show the voltage asymmetry ratio A_V for antiparallel and parallel configuration, respectively. The corresponding *ReMagX* fits are shown as black lines. The dashed lines indicate the q_z values at which constant q_z scans were performed (shown below).

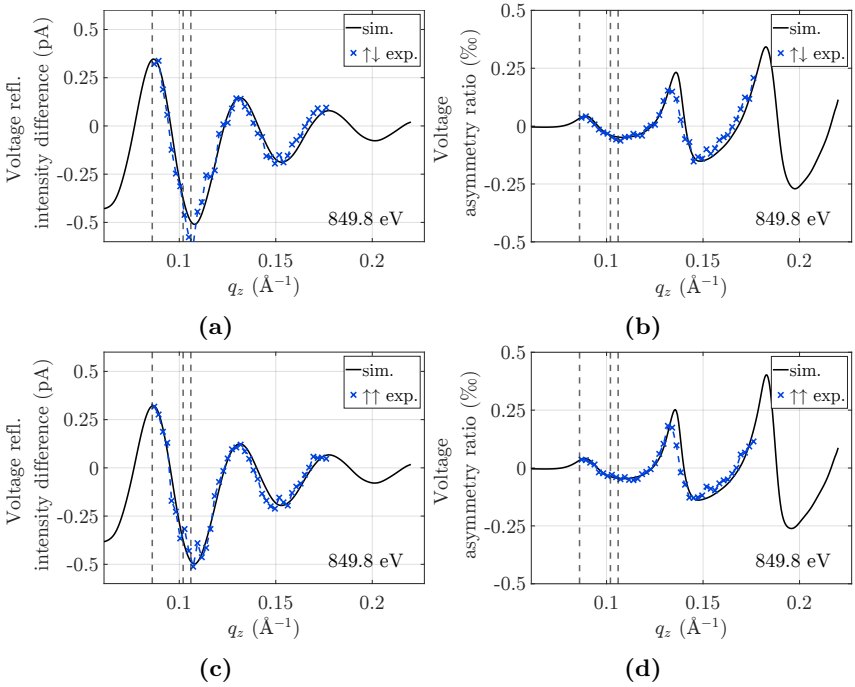

Figure 5.10: VXRR constant energy q_z-scans at 849.8 eV, which is at the onset of the Ni L_3-edge. (a) and (c) show the difference in reflected photo current $I_{\text{lock-in}}$ between positive and negative applied voltage for antiparallel and parallel configuration of sample magnetization and photon helicity, respectively. (b) and (d) show the voltage asymmetry ratio A_V for antiparallel and parallel configuration, respectively. The corresponding *ReMagX* fits are shown as black lines. The dashed lines indicate the q_z values at which constant q_z scans were performed (shown below).

Constant q_z Energy-Scans

Constant q_z energy-scans are necessary in order to study the energy dependence of the voltage-induced changes to the x-ray optical properties. Figures 5.11, 5.12, and 5.13 show measurements at $q_z = 0.106\,\text{Å}^{-1}$ (average of 14 repeated measurements), $q_z = 0.086\,\text{Å}^{-1}$ (average of 4 repeated measurements), and $q_z = 0.102\,\text{Å}^{-1}$ (average of 2 repeated measurements), respectively. The q_z values $0.106\,\text{Å}^{-1}$ and $0.102\,\text{Å}^{-1}$ were chosen since the measured reflected x-ray intensity difference has a maximum there for the measurements at 850.5 eV and 849.8 eV, respectively (see Fig. 5.9 and Fig. 5.10). The measurement at $q_z = 0.086\,\text{Å}^{-1}$ was performed since the voltage signal has the opposite sign here. In all three figures, the left column shows the measured lock-in signal $I_{\text{lock-in}}$ and the right column the voltage asymmetry A_{V} and in Figs. 5.11 and 5.12, the top and bottom row show measurements with antiparallel and parallel orientation of sample magnetization and photon helicity, respectively. At $q_z = 0.102\,\text{Å}^{-1}$, only measurements with antiparallel orientation were performed. The constant q_z energy-scans at the three different q_z values all show a sharp edge between 849.0 eV and 849.8 eV, where the voltage asymmetry ratio raises to about $0.04 - 0.06\,‰$. Above 849.8 eV, the voltage signal decreases again and returns to zero at 854 eV. The maximum of the voltage asymmetry ratio is at 849.8 eV for measurements at all three q_z values, which is at the onset of the Ni L_3-edge. The measurement in Fig. 5.13 at $q_z = 0.102\,\text{Å}^{-1}$ scans over the whole Ni L-edge energy range. At the L_3-edge, a clear voltage signal is visible, at the L_2-edge, no clear signal that is above the background signal is detectable.

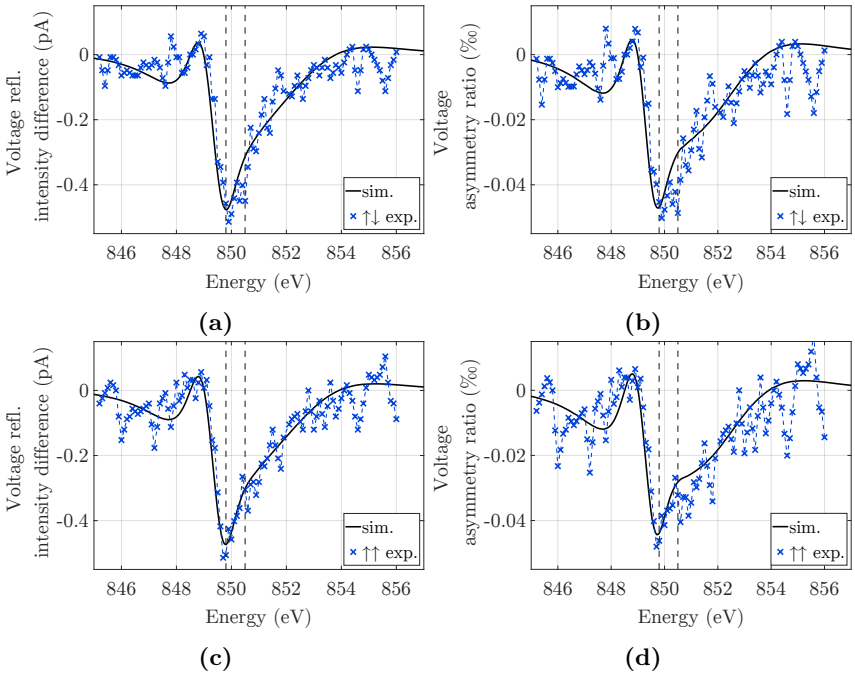

Figure 5.11: VXRR constant q_z energy-scans at $q_z = 0.106\,\text{Å}^{-1}$. (a) and (c) show the difference in reflected photo current $I_{\text{lock-in}}$ between positive and negative applied voltage for antiparallel and parallel configuration of sample magnetization and photon helicity, respectively. (b) and (d) show the voltage asymmetry ratio A_{V} for antiparallel and parallel configuration, respectively. The corresponding *ReMagX* fits are shown as black lines. The dashed lines indicate the photon energy values at which constant energy q_z-scans were performed (shown above).

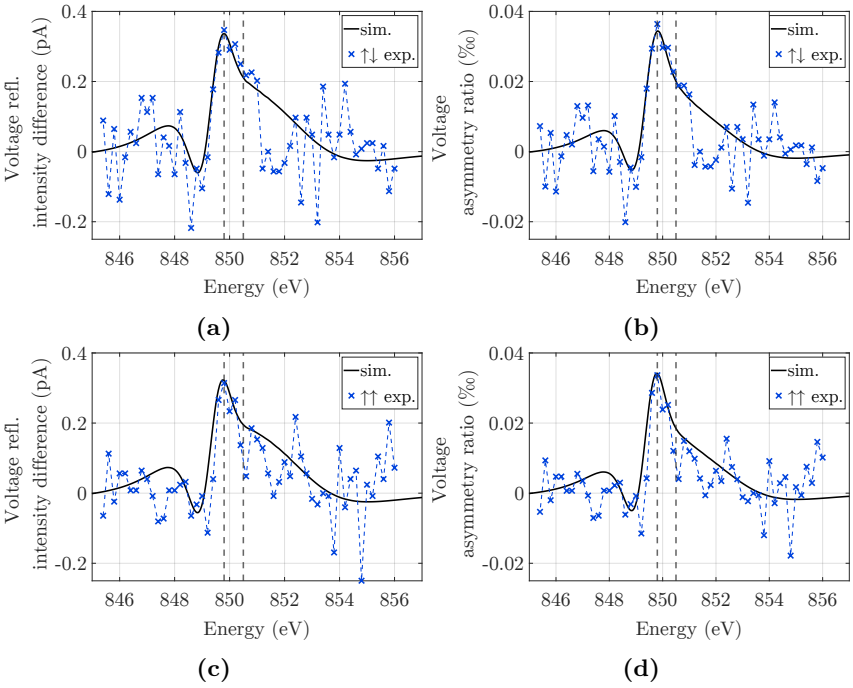

Figure 5.12: VXRR constant q_z energy-scans at $q_z = 0.086\,\text{Å}^{-1}$. (a) and (c) show the difference in reflected photo current $I_{\text{lock-in}}$ between positive and negative applied voltage for antiparallel and parallel configuration of sample magnetization and photon helicity, respectively. (b) and (d) show the voltage asymmetry ratio A_{V} for antiparallel and parallel configuration, respectively. The corresponding *ReMagX* fits are shown as black lines. The dashed lines indicate the photon energy values at which constant energy q_z-scans were performed (shown above).

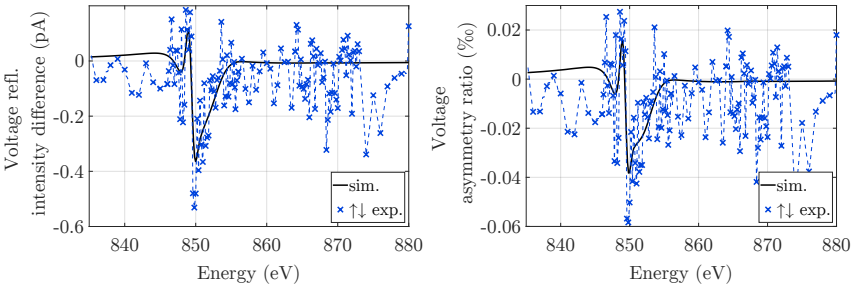

(a) **(b)**

Figure 5.13: VXRR constant q_z energy-scans at $q_z = 0.102\,\text{Å}^{-1}$. (a) shows the difference in reflected photo current $I_{\text{lock-in}}$ between positive and negative applied voltage for antiparallel configuration of sample magnetization and photon helicity. (b) shows the corresponding voltage asymmetry ratio A_{V}. The corresponding *ReMagX* fits are shown as black lines.

Fitting of VXRR Measurements

Extracting physically meaningful results from those measurements is not straightforward, and sophisticated simulations with *ReMagX* are required. The exact chemical and magnetic depth profile of the sample was retrieved from the XRR and XRMR measurements presented in chapter 4. Those profiles are kept unchanged during the simulations of VXRR data. As described in section 5.2.2, an artificial layer at the SiO_2/Ni interface is introduced which carries the voltage optical properties Δf_1^{V} and Δf_2^{V}. This layer reflects the position where the charges which are moved by the applied electric field populate interfacial states. The black lines in Figs. 5.9, 5.10, 5.11, 5.12, and 5.13 show the *ReMagX* fits, which are in almost perfect agreement with the experimental data. The position of the voltage layer strongly affects the periodicity of the fits for measurements in constant energy mode (Figs. 5.10 and 5.9). Thus, the position can be determined with an accuracy of $\pm 0.3\,\text{nm}$ (details on how this accuracy is determined are explained later). In Fig. 5.14, the chemical and magnetic depth pro-

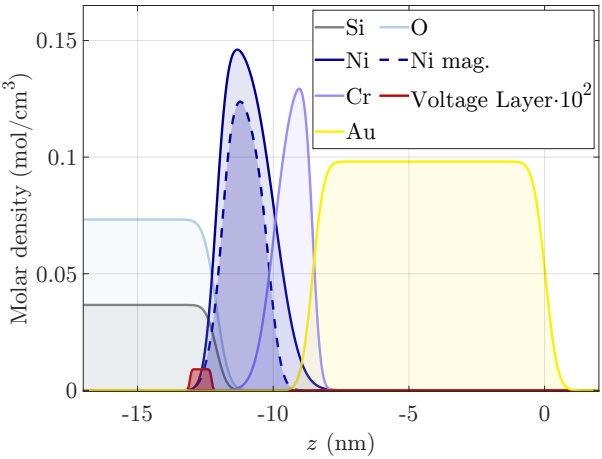

Figure 5.14: Elemental and magnetic depth profile of the 2 nm Ni(II) sample (see chapter 4 for details on how they are retrieved). The voltage layer, which indicates the Ni atoms that are affected by the applied electric field, is shown in red. The density of the voltage layer in the plot is multiplied by 100 since it would not be visible otherwise. The voltage layer has a density of $9.03 \cdot 10^{-5}\ \frac{\text{mol}}{\text{cm}^3}$ and a thickness of 0.8 nm.

file of the sample is shown together with the voltage layer in red. The position of the voltage layer suggests that only the Ni atoms which have the smallest distance to the Si substrate are affected by the applied electric field. This is reasonable since the electric field is highest for those Ni atoms, especially at peak positions where the distance between Ni atoms and the Si substrate is even smaller. The product of voltage layer width and its density represents the number of Ni atoms per area N_{Ni} which are affected by the electric field. It was set to a value of $7.21 \cdot 10^{-12}\ \frac{\text{mol}}{\text{cm}^2}$, which is derived by division of the applied electric displacement field D_{rms} by the Avogadro constant N_{A} and the elementary charge e. This way, N_{Ni} is directly connected to the applied voltage and takes the same value as the number of moved electrons per area N_{e^-}, thus assuming that as many Ni atoms are affected by the voltage as there are moved electrons (i.e.

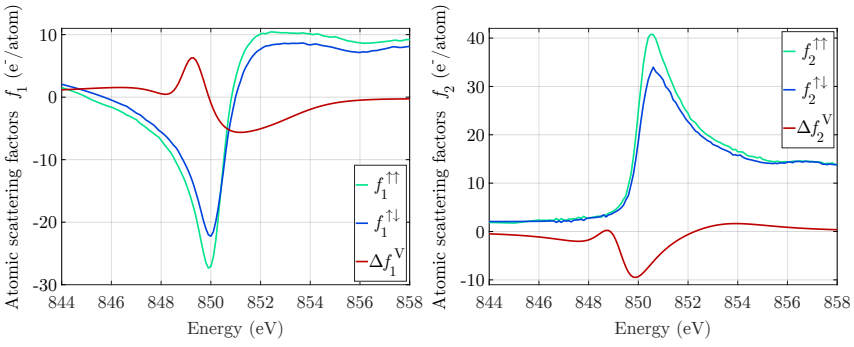

(a) **(b)**

Figure 5.15: (a) Real (f_1) and (b) imaginary (f_2) part of the atomic scattering factor at the Ni L_3-edge. The optical properties for parallel and antiparallel orientation of sample magnetization and photon helicity are shown in green and blue, respectively. The voltage x-ray optical properties Δf_1^V and Δf_2^V are shown in red.

one electron per affected Ni atom is moved). However, the choice of N_{Ni} does not change the main results of the analysis, as will be shown later. For a constant product of voltage layer width and its density, changing the roughness, width or density of the voltage layer does not affect the fit quality, except when the roughness exceeds physically meaningful values (e.g. becoming much larger than the roughness in the chemical profile).

As described in section 5.2.2, when fitting constant energy VXRR data, the position of the voltage layer, its width and density, and the voltage optical x-ray properties Δf_1^V and Δf_2^V at the corresponding energy are free parameters for the fit. However, for constant q_z-energy scans the energy dependence of the voltage optical x-ray properties is needed, and Δf_1^V and Δf_2^V need to be related via Kramers-Kronig relation. Thus, Δf_1^V and Δf_2^V are modeled via a superposition of Lorentzians of the form shown in equations 5.7 and 5.8. The position, width and amplitude of the Lorentzians, together with the position, width and density of the voltage layer, are the free fitting parameters. Those parameters are varied until the

Table 5.2: Amplitude α, width β, and energy postion E_0 of the three Lorentzians used to model the voltage x-ray optical parameters Δf_1^{V} and Δf_2^{V} at the Ni L_3-edge.

α (e^-/atom)	β (eV)	E_0 (eV)
0.2244	2.06775	849.109
-0.2543	2.26278	849.194
0.0176	5.2014	853.329

ReMagX fits reproduce all the performed measurements (constant energy and constant q_z-scans) as well as possible. For all fits shown in Figs. 5.9, 5.10, 5.11, 5.12, and 5.13, the same voltage optical x-ray properties Δf_1^{V} and Δf_2^{V} were used. They are shown in Fig. 5.15 together with the atomic scattering factors for parallel and antiparallel orientation of sample magnetization and photon helicity, respectively. The parameters used for the three Lorentzians which are superimposed to model the voltage x-ray optical properties are listed in table 5.2. The shown voltage optical properties in Fig 5.15 are the electric-field-induced equivalent to the magneto optical properties that are retrieved from XMCD measurements (shown for Ni in Fig. 3.9a). The difference is that the voltage optical properties arise from a difference in absorption between positive and negative applied voltage, while the magneto optical properties arise from a difference in absorption between parallel and antiparallel orientation of magnetization and photon helicity.

Voltage-Induced Oxidation State Changes of Interfacial Ni Atoms

The imaginary component of the voltage x-ray optical properties Δf_2^{V} is shown in Fig. 5.15b. It has its maximum negative value at an energy of 849.9 eV, which is at the onset of the Ni L_3-edge. The negative value of

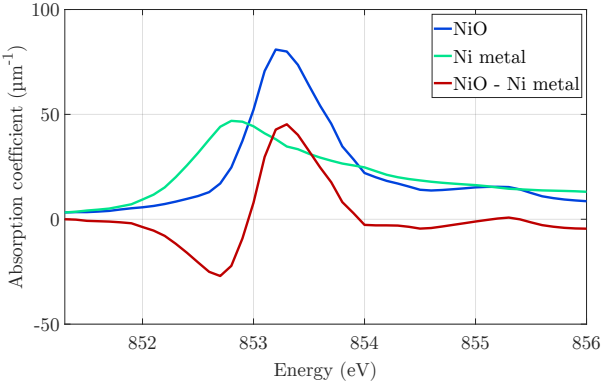

Figure 5.16: Reproduced absorption coefficient of NiO (blue) and Ni (green) at the L_3-edge from Figure 8 in [85]. The difference between the NiO and the Ni spectrum is shown in red.

Δf_2^{V} at the onset of the Ni L_3-edge means that a positive voltage basically shifts the edge to slightly higher energies. In the present experimental setup, a positive voltage accumulates holes at the SiO_2/Ni interface, which means that the interfacial Ni atoms have, on average, a slightly higher oxidation state for a positive applied voltage. When comparing the absorption spectra at the L_3-edge of Ni atoms with different oxidation states [85–87], it becomes apparent that the edge shifts to higher energies for higher oxidation states. Thus, the present result, indicating that interfacial Ni atoms slightly change their oxidation state in an electric field, and that therefore the L_3-edge shifts to slightly higher energies for a positive applied voltage, seems reasonable. In Fig. 5.16, the difference between a NiO and Ni absorption spectrum is shown (the spectra are reproduced from [85]), which shows in general a roughly comparable shape as Δf_2^{V} in Fig. 5.15b. Both have a negative sign at the onset of the L_3-edge and a positive sign after the edge. This further supports the finding of a varying oxidation state of interfacial Ni atoms induced by an applied voltage.

Interfacial Spin Polarization of Ni Atoms

All VXRR measurements at the Ni sample were performed with both parallel and antiparallel orientation of sample magnetization and photon helicity (except the constant q_z energy-scan at $0.102\,\text{Å}^{-1}$ in Fig. 5.13, which was only measured for antiparallel orientation). Comparing the corresponding parallel and antiparallel measurements, no significant difference could be observed. Also, the same Δf_1^{V} and Δf_2^{V} were used for fitting the parallel and antiparallel measurements, different voltage optical parameters were not necessary to obtain good fit results. This suggests that there is either no magnetic component in the voltage x-ray optical properties or the component is too small, and the effect on the measurements is below noise level. This in turn suggests that the interfacial Ni states at the Fermi energy at a SiO_2/Ni interface have a rather low spin polarization, which is consistent with new results obtained by voltage dependent magneto-optical Kerr effect (VMOKE) measurements on similar samples [190].

Quantitative Analysis of the VXRR Signal

For 3d TMs, the intensity $I(f_2)$ of their non-magnetic optical properties at the L_3-edge is proportional to the number of 3d holes n_{h} [56,79] (see also section 3.2.1). Since the voltage x-ray optical properties represents how much the non-magnetic optical properties are changed by an electric field, the intensity of the voltage optical property $I(\Delta f_2^{\text{V}})$ is proportional to the electric-field-induced change in the number of 3d holes Δn_{h}. Taking the ratio $I(\Delta f_2^{\text{V}})/I(f_2)$ and multiplying it by the number of 3d holes per Ni atom (for Ni $n_{\text{h}} = 1.66$ in bulk [191]) then represents the measured electric-field-induced change in the number of 3d holes per Ni atom Δn_{h}:

$$\Delta n_{\text{h}} = n_{\text{h}} \cdot \frac{I(\Delta f_2^{\text{V}})}{I(f_2)}. \tag{5.12}$$

Values for $I(f_2)$ and $I(\Delta f_2^{\mathrm{V}})$ can be estimated by either integrating over the respective spectra or by taking their maximum values. This results in $\Delta n_{\mathrm{h}} = 0.39$ and 0.42 when integrating over the spectra or taking their maximum, respectively. The average of the two values is $\Delta n_{\mathrm{h}} = 0.405 \pm 0.015$, which represents the average change of 3d holes in the Ni atoms that are affected by the voltage in the simulation.

From the number of moved electrons N_{e^-} and the number of electric field affected Ni atoms N_{Ni} in the simulation, the maximum possible change in number of 3d holes per Ni atom $\Delta n_{\mathrm{h}}^{\mathrm{max}}$ can be calculated. As described above, $N_{\mathrm{e}^-} = 7.21 \cdot 10^{-12}\ \frac{\mathrm{mol}}{\mathrm{cm}^2}$ is calculated from the electric displacement field D_{rms}, and N_{Ni} is assumed to be the same value for the present simulations. The ratio of N_{e^-} to N_{Ni} then represents the maximum possible change in number of 3d holes per Ni atom:

$$\Delta n_{\mathrm{h}}^{\mathrm{max}} = \frac{N_{\mathrm{e}^-}}{N_{\mathrm{Ni}}} = 1. \tag{5.13}$$

However, the experimental results showed that $\Delta n_{\mathrm{h}} = 0.405 \pm 0.015$, which suggests that only about 40 % of the moved electrons (de)populate Ni states and consequential 60 % of the electrons (de)populate oxygen and silicon states.

Independence of the results on the chosen voltage layer area density

One might assume that the choice of $N_{\mathrm{Ni}} = N_{\mathrm{e}^-} = 7.21 \cdot 10^{-12}\ \frac{\mathrm{mol}}{\mathrm{cm}^2}$ for the simulations has a great impact on the results and their implications. However, the result that only about 40 % of the moved electrons (de)populate Ni states is independent of N_{Ni}, as will be shown in this section.

As described above, the measured change of Ni 3d holes Δn_{h} is calcu-

lated via:

$$\Delta n_{\mathrm{h}} = n_{\mathrm{h}} \cdot \frac{I(\Delta f_2^{\mathrm{V}})}{I(f_2)}. \tag{5.14}$$

The simulations with *ReMagX* showed that $I(\Delta f_2^{\mathrm{V}})$ is proportional to the inverse of the number of interfacial Ni atoms N_{Ni} that are affected by the electric field, which is given by the product of width and density of the voltage layer. $I(\Delta f_2^{\mathrm{V}})$ does also scale linearly with the applied electric field D_{rms}(see next section):

$$I(\Delta f_2^{\mathrm{V}}) = k \cdot \frac{D_{\mathrm{rms}}}{N_{\mathrm{Ni}}}, \tag{5.15}$$

with the proportionality constant k. With equation 5.14 and 5.15 Δn_{h} can be calculated via:

$$\Delta n_{\mathrm{h}} = n_{\mathrm{h}} \cdot \frac{k \cdot D_{\mathrm{rms}}}{I(f_2) \cdot N_{\mathrm{Ni}}}. \tag{5.16}$$

On the other hand, the maximum possible change of Ni 3d holes $\Delta n_{\mathrm{h}}^{\mathrm{max}}$ would be achieved when all moved electrons $N_{\mathrm{e^-}}$ would populated states of electric field affected Ni atoms N_{Ni} and is calculated via their ratio (as described above):

$$\Delta n_{\mathrm{h}}^{\mathrm{max}} = \frac{N_{\mathrm{e^-}}}{N_{\mathrm{Ni}}} = \frac{D_{\mathrm{rms}}}{e \cdot N_{\mathrm{A}} \cdot N_{\mathrm{Ni}}}, \tag{5.17}$$

where the number of moved electrons $N_{\mathrm{e^-}}$ can be determined from the applied displacement field D_{rms}, the elementary charge e, and the Avogadro constant N_{A} via:

$$N_{\mathrm{e^-}} = \frac{D_{\mathrm{rms}}}{eN_{\mathrm{A}}}. \tag{5.18}$$

In order to calculate how many of the moved electrons actually (de)populate Ni states, the ratio of Δn_{h} to $\Delta n_{\mathrm{h}}^{\mathrm{max}}$ has to be calculated. From equa-

tions 5.16 and 5.17 follows:

$$\frac{\Delta n_{\mathrm{h}}}{\Delta n_{\mathrm{h}}^{\max}} = n_{\mathrm{h}} \cdot \frac{k \cdot D_{\mathrm{rms}}}{I(f_2) \cdot N_{\mathrm{Ni}}} \cdot \frac{e \cdot N_{\mathrm{A}} \cdot N_{\mathrm{Ni}}}{D_{\mathrm{rms}}} = \frac{e \cdot N_{\mathrm{A}} \cdot n_{\mathrm{h}} \cdot k}{I(f_2)} \tag{5.19}$$

Since N_{Ni} and D_{rms} cancel out in the above equation, the fraction of moved electrons which (de)populate Ni atoms is independent of the choice of N_{Ni} in the simulations and independent of the applied electric field. By choosing $N_{\mathrm{Ni}} = N_{\mathrm{e^-}}$, the intensity of the voltage optical x-ray properties $I(\Delta f_2^{\mathrm{V}})$ is normalized to the applied voltage and the results for $I(\Delta f_2^{\mathrm{V}})$ for different elements at the interface or for different samples become comparable.

Another physically reasonable choice for N_{Ni} would be to set it to the area density of a Ni monolayer, thus assuming that exactly one Ni monolayer at the SiO_2/Ni interface is affected by the voltage (see [172]). As shown above, this does not change the result that only about 40 % of the moved electrons (de)populate Ni states. However, the average change of Ni 3d holes of the voltage affected Ni atoms does change when changing N_{Ni} (see equation 5.15). The difference between the two choices of N_{Ni} is that for $N_{\mathrm{Ni}} = N_{\mathrm{e^-}}$ it is assumed that each moved electron can (de)populate exactly one Ni atom while the other interfacial Ni atoms remain unaffected, while for the assumption that N_{Ni} represents a Ni monolayer the voltage effect is averaged over all interfacial Ni atoms. Thus, $I(\Delta f_1^{\mathrm{V}})$ and $I(\Delta f_2^{\mathrm{V}})$ are normalized to the applied field for $N_{\mathrm{Ni}} = N_{\mathrm{e^-}}$, or normalized to the interface when N_{Ni} represents a Ni monolayer.

Voltage dependent measurements

To prove the linearity of the VXRR effect, voltage dependent measurements have been performed. Figure 5.17 shows the value of the voltage asymmetry ratio A_{V} measured at a photon energy of 849.8 eV and a q_z-

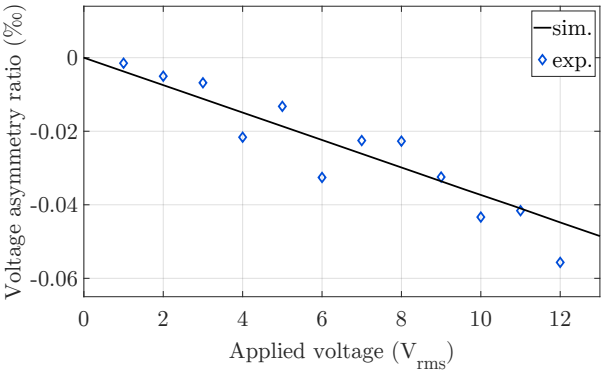

Figure 5.17: Amplitude of the voltage asymmetry ratio as a function of applied voltage V_{rms}, measured at the Ni sample at a photon energy of 849.8 eV and at a q_z value of 0.106 $Å^{-1}$. The simulated values were achieved by scaling down the voltage x-ray optical properties linearly, corresponding to the applied voltage.

value of 0.106 $Å^{-1}$ as a function of applied voltage. The measurements are done between 1 V_{rms} and 12 V_{rms} in 1 V_{rms} steps. The corresponding *ReMagX* fit was achieved by linearly scaling down the voltage x-ray optical properties Δf_1^V and Δf_2^V. For an applied voltage of 1 V_{rms}, Δf_1^V and Δf_2^V, which are shown in Fig. 5.15, are scaled by a factor of $\frac{1}{12}$ and for a voltage of 12 V_{rms} the scaling factor is 1. The voltage signal shows a linear dependence on the applied voltage.

Error estimation of voltage layer position

The quality of all shown *ReMagX* fits is quantified by the sum of squared errors χ^2 [192]:

$$\chi^2 = \sum_i (A_{V_{i,\text{exp.}}} - A_{V_{i,\text{sim.}}})^2, \tag{5.20}$$

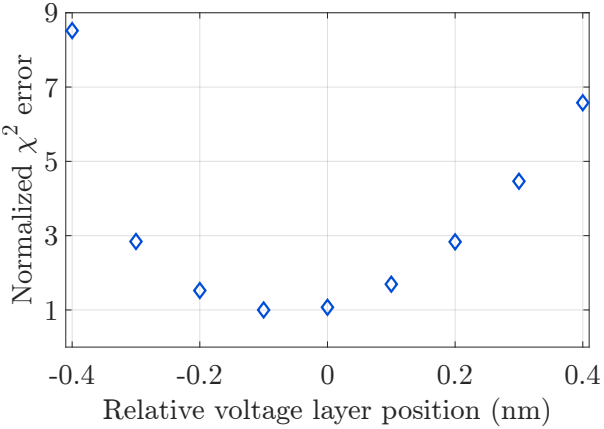

Figure 5.18: Normalized χ^2-error for the fit shown in Fig. 5.10c as a function of relative voltage layer position.

with the measured and simulated voltage asymmetry ratios $A_{V_{i,\mathrm{exp.}}}$ and $A_{V_{i,\mathrm{sim.}}}$, respectively. The smaller the value of χ^2, the better the quality of the fit. In order to determine the accuracy of the voltage layer position, the voltage layer is shifted relative to the position shown in Fig. 5.14 and χ^2 is calculated. Figure 5.18 shows the χ^2 value normalized to its minimum as a function of relative voltage layer position. The voltage layer is shifted from a relative position of -0.4 nm to 0.4 nm in 0.1 nm steps. The quality of the respective fits, quantified by χ^2, decrease drastically when the voltage layer is shifted from its original position. The sum of squared errors χ^2 is already tripled for a shift of ± 0.3 nm, thus the accuracy of the position of the voltage layer is conservatively assumed to be ± 0.3 nm. Figure 5.18 shows the evolution of χ^2 as a function of relative voltage position exemplarily for the fit shown in Fig. 5.10c. For the fits to the other shown measurements χ^2 behaves similarly under variation of the voltage layer position. The final position, as shown in Fig 5.14, has been derived by taking all measurements into account.

5.4.2 Voltage Effect for Interfacial Oxygen Atoms

The VXRR measurements at the Ni L_3-edge in the previous sections showed that only about 40 % of the electrons which are moved to the SiO_2/Ni interface by the electric field populate Ni states. Thus, the other 60 % of the electrons have to populate O and/or Si states at the SiO_2/Ni interface. Electrons are also moved by the electric field to and from the Si/SiO_2 interface of the sample, where they potentially (de)populate O and/or Si states. Therefore, VXRR measurements with an applied voltage of $12\,V_{rms}$ at the O K-edge are performed and the corresponding data together with *ReMagX* fit results are presented in this section.

VXRR Measurements at O K-Edge on Ni sample

In Figs. 5.19 and 5.20, constant energy q_z-scans of the electric-field-induced variations of reflected x-ray intensity for various photon energies around the O K-edge are shown. The VXRR signal at the O K-edge was found to be significantly stronger than the signal at the Ni L_3-edge. Thus, single measurements already provide a decent signal-to-noise ratio and it is not necessary to average over several measurements as was the case for measurements at the Ni L_3-edge. The voltage asymmetry ratio A_V, shown in the right column of the figures, is calculated via equation 5.6. The left column shows the measured lock-in signal $I_{\text{lock-in}}$, which is the difference in measured photo current when the electric field is switched from positive to negative. Measurements were performed at photon energies of 531 eV, 534 eV, 534.7 eV, 535.4 eV, and 537.8 eV. The overall VXRR signal for all energies at the O K-edge is higher than the signal that was measured at the Ni L_3-edge. Here, the voltage asymmetry A_V shows maximum values of almost 2 ‰ (for Ni it was less than 0.5 ‰), and the lock-in signal $I_{\text{lock-in}}$ shows values of almost 2 pA (for Ni it was lower than 0.5 pA). The

measured voltage asymmetry shows a superposition of a short and long periodic signal with a periodicity of $\Delta q_z = 0.0086\,\text{Å}^{-1}$ and $\Delta q_z = 0.05\,\text{Å}^{-1}$, respectively. From the periodicities, a first intuitive and rough estimate of the O based voltage layer positions p can be made via [35](see also equation 4.4)

$$p = \frac{2\pi}{\Delta q_z}. \tag{5.21}$$

For the short and long periodic signal, this results in a voltage position of approximately 73 nm and 12.6 nm from the sample surface. Comparing these values with the structural parameters of the sample in table 4.3, it can be seen that the two voltage layers producing the measured signal are located at the Si/SiO_2 and at the SiO_2/Ni interfaces. This is physically reasonable since the SiO_2 layer is electrically insulating, thus charges will accumulate at those interfaces. Those charges (de)populate electronic states of atoms at the interfaces and thereby change the local x-ray optical properties, which is the origin of the measured signal. For the constant energy q_z-scan at 537.8 eV in Fig. 5.20c, the long periodic contribution in the VXRR signal, which arises at the SiO_2/Ni interface, dominates. This is due to the high absorption of the O atoms in the SiO_2 layer at 537.8 eV (see Fig. 3.11), which reduces the reflected intensity from the Si/SiO_2 interface. On the other hand, in the measurement at 531 eV (see Fig. 5.19a) the short periodic signal, which arises at the Si/SiO_2 interface, dominates. Thus, fitting all the q_z-scans in Figs. 5.19 and 5.20 simultaneously, will result in detailed information about the electric-field-induced changes in electronic structure at both interfaces.

As described in sections 5.2.2 and 5.4.1, in order to fit the individual measurements shown in Figs. 5.19 and 5.20, the position of the voltage layer and the voltage x-ray optical parameters Δf_1^{V} and Δf_2^{V} at the respective photon energy are free fitting parameters. In Fig. 5.21, the chemical and magnetic layer profile, together with the voltage layers of the O atoms that are affected by the electric field are shown. Similar to the approach for measurements at the Ni L_3-edge, the densities and widths

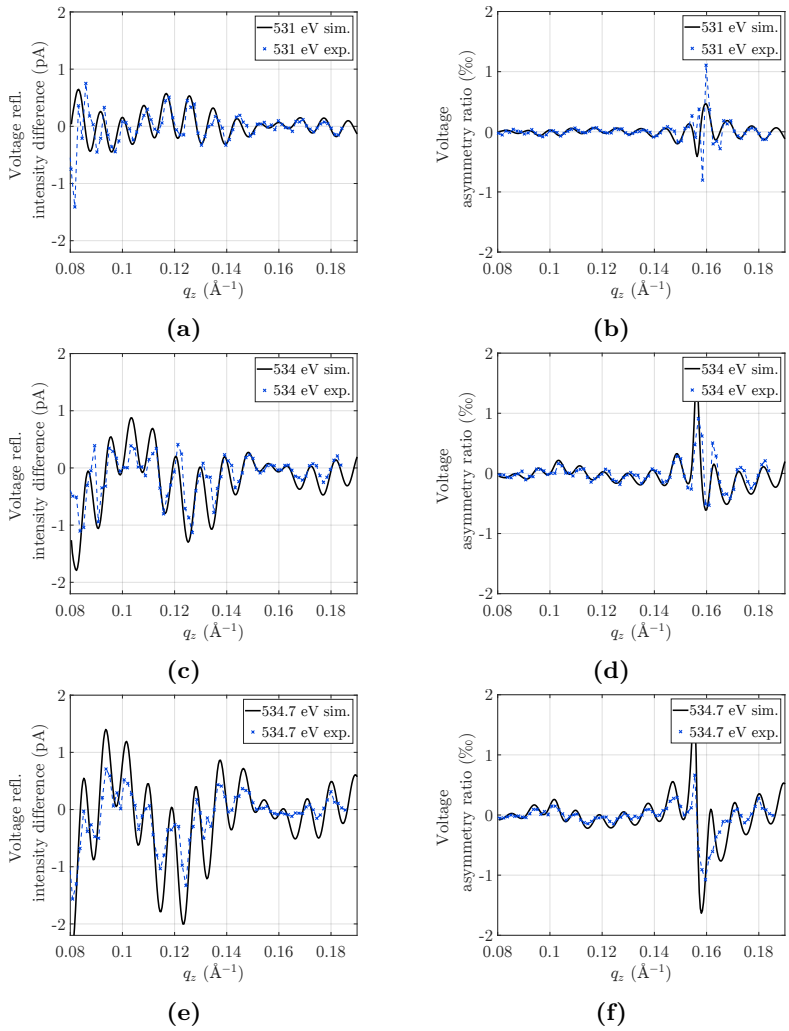

Figure 5.19: VXRR constant energy q_z-scans at various photon energies around the O K-edge measured at the 2 nm Ni(II) sample. The left column shows the difference in reflected photo current $I_{\text{lock-in}}$ between positive and negative applied voltage and the right column shows the voltage asymmetry ratio A_{V}. The corresponding *ReMagX* fits are shown as black lines.

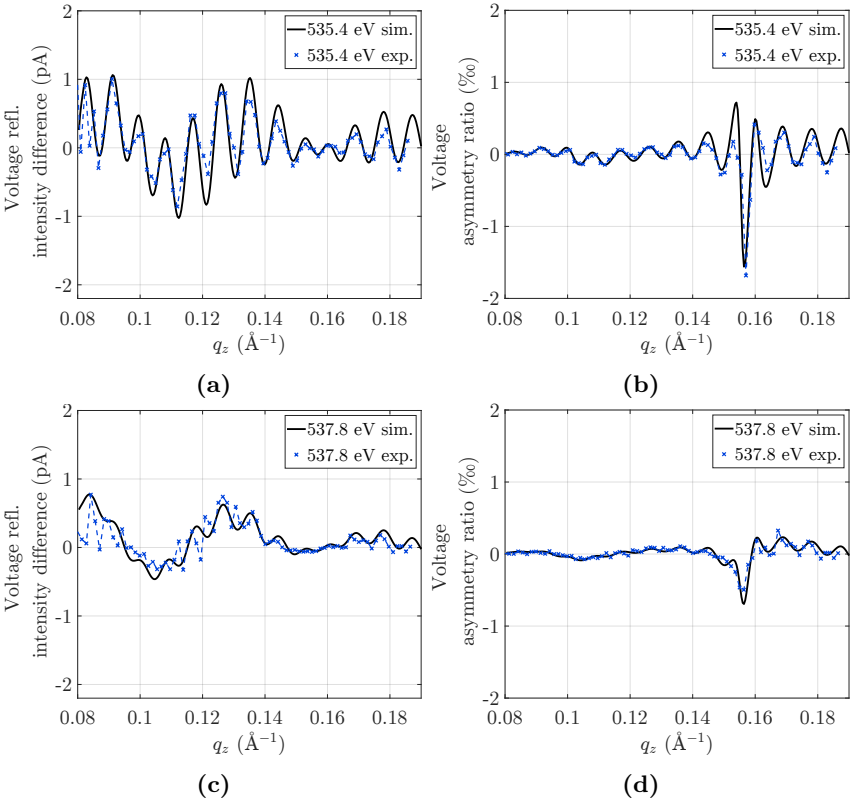

Figure 5.20: VXRR constant energy q_z-scans at various photon energies around the O K-edge measured at the 2 nm Ni(II) sample. The left column shows the difference in reflected photo current $I_{\text{lock-in}}$ between positive and negative applied voltage and the right column shows the voltage asymmetry ratio A_{V}. The corresponding *ReMagX* fits are shown as black lines.

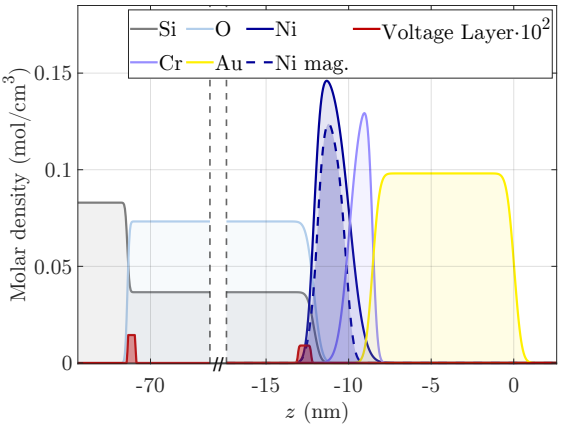

Figure 5.21: Elemental and magnetic depth profile of the 2 nm Ni(II) sample (see chapter 4 for details on how they are retrieved). The voltage layers, which indicates the O atoms that are affected by the applied electric field, are shown in red. The densities of the voltage layers in the plot are multiplied by 100 since it would not be visible otherwise. The upper voltage layer has a density of $9.03 \cdot 10^{-5}\ \frac{\text{mol}}{\text{cm}^3}$ and a thickness of 0.8 nm, and the lower one a density of $1.44 \cdot 10^{-4}\ \frac{\text{mol}}{\text{cm}^3}$ and a thickness of 0.5 nm.

of the voltage layers are chosen in a way that their product (which represents the number of O atoms per area N_{O} that are affected by the applied field) takes the same value as the number of moved electrons per area $N_{\text{e}^-} = 7.21 \cdot 10^{-12}\ \frac{\text{mol}}{\text{cm}^2}$. This way, the results for Δf_1^{V} and Δf_2^{V} will be automatically normalized to the applied voltage and results from different samples where different voltages were applied can be directly compared.

In Fig. 5.22, an energy-scan measured at a constant q_z value of $0.127\ \text{Å}^{-1}$ is shown. Again, on the left is the measured lock-in signal $I_{\text{lock-in}}$ and on the right the voltage asymmetry ratio A_{V}. Several distinct peaks are visible in the measurement. In order to fit the shown energy-scan, the energy dependence of the voltage optical x-ray properties Δf_1^{V} and Δf_2^{V} is needed, and they need to be related via the Kramers-Kronig relation. Similar to the fits at the Ni L_3-edge, Δf_1^{V} and Δf_2^{V} are modeled via a superposition

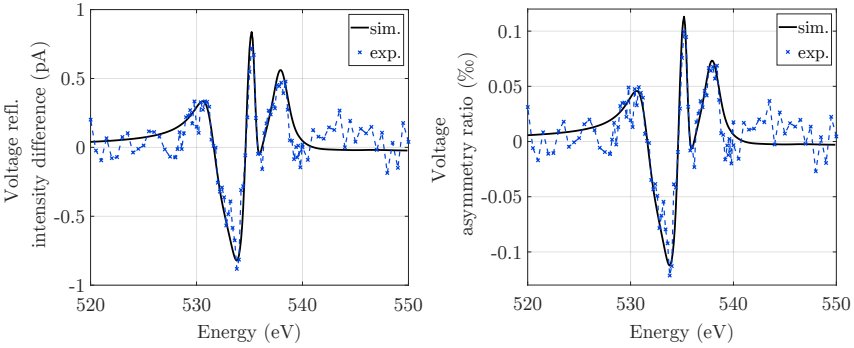

Figure 5.22: VXRR constant q_z energy-scan at $q_z = 0.127\,\text{Å}^{-1}$ over the O K-edge measured on the 2 nm Ni(II) sample. (a) The difference in reflected photo current $I_{\text{lock-in}}$ between positive and negative applied voltage and (b) the voltage asymmetry ratio A_{V}. The corresponding *ReMagX* fits are shown as black lines.

of Lorentzians of the form shown in equations 5.7 and 5.8. The parameters of the Lorentzians are then varied until the fits for energy-scan as well as the q_z-scans are in good agreement with the measurements. The sign of the voltage optical properties for the lower and upper voltage layer at the Si/SiO_2 and SiO_2/Ni interface, respectively, has to be opposite since the charges accumulating at the two interfaces have opposite signs. Thus, for a positive voltage, states at the upper interface are depopulated while states at the lower interface are populated. The results for Δf_1^{V} and Δf_2^{V} at the O K-edge for the Si/SiO_2 and the SiO_2/Ni interface are shown in Figs. 5.23 and 5.24, respectively.

Voltage Optical Parameters at O K-Edge

For the fits shown in Figs. 5.19, 5.20, and 5.22, a superposition of 4 Lorentzians is used to model the voltage x-ray optical properties Δf_1^{V}

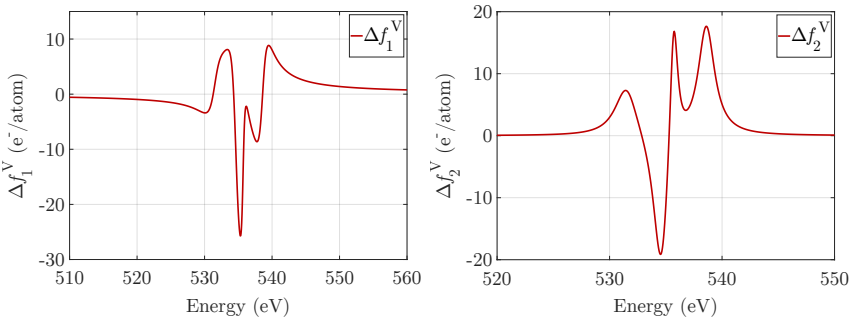

Figure 5.23: (a) Real (Δf_1^V) and (b) imaginary (Δf_2^V) part of the voltage x-ray optical properties at the O K-edge, for the lower voltage layer, which is located at the Si/SiO_2 interface.

and Δf_2^V. They are shown in Fig. 5.23 and 5.24 for the lower and upper interface, respectively. The corresponding parameters for the Lorentzians are listed in table 5.3. As expected, the voltage x-ray optical properties have opposite signs for the lower and upper voltage layer, since for a given voltage sign, opposing charges accumulate at the Si/SiO_2 and SiO_2/Ni interfaces. For both interfaces similar spectral features are found, with different spectral weight. The small differences between them presumably originate from the fact that O atoms at the two different interfaces have different neighboring atoms. At the lower interface, only Si atoms are in the vicinity of O atoms, while at the upper interface also Ni atoms are present. Because of that, the electronic structure of the O atoms at the two different interface potentially differs slightly from each other.

It is noticeable that the amplitude of the voltage x-ray optical properties is a lot lower for the upper interface. This suggests that more of the moved electrons have to (de)populate O state at the lower interface than at the upper interface. By integrating over the absolute value of the two spectra in Figs. 5.23b and 5.24b and taking their ratio, the ratio between the number of electrons (de)populating O states at the respective interface

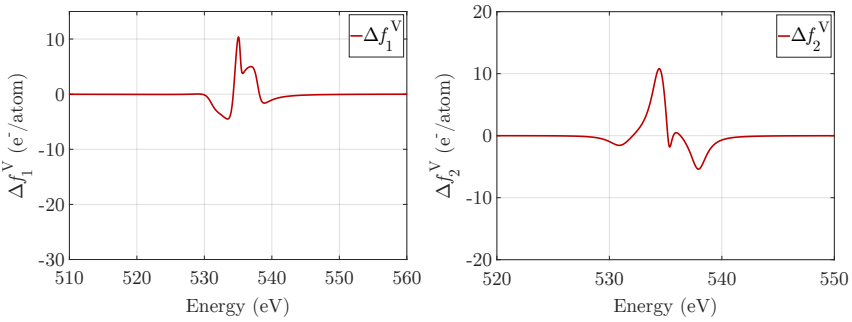

Figure 5.24: (a) Real (Δf_1^V) and (b) imaginary (Δf_2^V) part of the voltage x-ray optical properties at the O K-edge, for the upper voltage layer located at the SiO_2/Ni interface.

can be estimated. The ratio of the two integrals is 0.3, which means that at the upper interface only about a third of the O states are (de)populated, compared to the lower interface.

In Fig. 5.25, different O K-edge XAS spectra are shown and compared to Δf_2^V from the SiO_2/Ni interface. The O K-edge spectrum measured with ERNSt at a blank SiO_2 surface is shown, as well as from literature reproduced O K-edge spectra measured at SiO_2 glass, at bulk SiO_2 and at a Si/SiO_2 interface, and at a NiO sample. Since the literature spectra originate from different sources, slight deviations of the photon energy calibration might be possible. The main features of Δf_2^V coincide with features of the shown O K-edge spectra (e.g. the O K pre-edge peak around 531 eV, the rising edge around 535 eV and on top of the O K-edge around 538 eV). However, the exact interfacial x-ray optical properties of O atoms in the studied sample are unknown and can vary strongly from any known bulk oxide optical properties. For example, the two spectra in Fig. 5.25(b) show the O K-edge of bulk SiO_2 (dark blue line) and at the Si/SiO_2 interface (dashed dark blue line), revealing that the interfacial oxygen spectrum varies strongly from the bulk spectrum. The edge of the interfacial spec-

Table 5.3: Amplitude α, width β, and energy postion E_0 of the four Lorentzians used to model the voltage x-ray optical parameters Δf_1^{V} and Δf_2^{V} at the O K-edge for the upper and lower voltage layer.

	α (e^-/atom)	β (eV)	E_0 (eV)
upper interface	-0.01	2.5	531
	0.0412	1.75	534.5
	-0.01	0.7	535.3
	-0.02	1.8	537.9
lower interface	0.04	2.5	531.5
	-0.08	1.75	534.6
	0.04	0.9	535.7
	0.06	1.8	538.6

trum is shifted by about 4 eV to lower energies and the resonance is a lot less prominent. Since Δf_2^{V} represents the voltage-induced changes to the interfacial x-ray optical properties, but the exact interfacial x-ray optical properties are not known, it is difficult to attribute the features of Δf_2^{V} to the (de)population of actual O states. However, the peak at 531 eV of Δf_2^{V} coincides with the pre-peak in NiO and the rising edge of interfacial SiO_2, and the main peak of Δf_2^{V} coincides with the onset of SiO_2 edge. This suggests that the electronic states that correspond to the respective features in the shown XAS spectra are (de)populated when a voltage is applied.

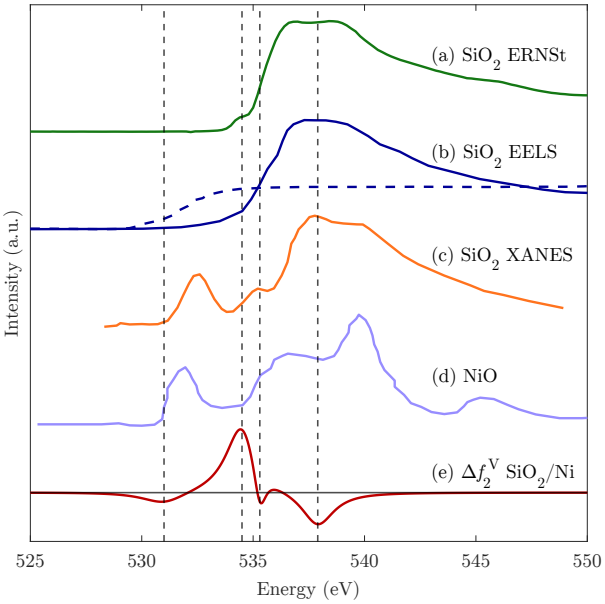

Figure 5.25: Comparsion between O K-edge spectra at different samples and with different measurement techniques. (a) SiO_2 O K-edge spectra measured with ERNSt in TEY mode, (b) SiO_2 bulk (solid) and Si/SiO_2 interface (dashed) O K-edge spectra measured with EELS (reproduced from [48]), (c) SiO_2 glass O K-edge measured with XANES (reproduced from Fig. 24(b) in [111]), (d) NiO O K-edge measured with EELS (reproduced from Fig. 34 in [89]), and (e) Δf_2^{V} at the SiO_2/Ni interface. The vertical dashed lines indicate the position of the 4 Lorentzians used to model Δf_2^{V}.

VXRR Measurements at O K-Edge on different samples

VXRR measurements at the O K-edge were also performed on the 2 nm Fe and on the 2 nm Co(II) sample (which were already studied in chapter 4), on a sample with Cr(2 nm)/Au(10 nm), and on a sample with only 10 nm Au on top of the Si/SiO_2(50 nm) substrate. The corresponding VXRR measurements, fits and layer profiles are shown in appendix B. Since the Si/SiO_2 interface is the same for all samples, the same voltage x-ray optical properties as shown in Fig. 5.23 need to be used for the lower voltage layer in each sample. However, the voltage x-ray optical properties for the upper voltage layer can differ slightly between the samples, since the chemical composition of the upper interface is different in each sample and thus the electronic structure of the O atoms might be different. Using the same voltage optical properties for the lower voltage layer in each sample and slightly varying them at the upper voltage layer results indeed in good fits (as can be seen in appendix B). That the same voltage optical properties for the lower interface result in goods fits for all samples supports the robustness of the model.

Figure 5.26 shows the results for Δf_2^{V} at the upper interface for the different studied samples, the corresponding plots for Δf_1^{V} can be seen in the appendix B. The peak around 530 eV for the sample with Fe and Ni on top of the SiO_2, might be related to the typical TM 3d/O 2p hybridized pre-edge states that are (de)populated by the applied voltage. XAS peaks corresponding to TM 3d/O 2p hybridized states usually appear a few eV before the main O K-edge (see for example Fig. 5.25(d) or [89]). Surprisingly, this peak does not appear for the samples with Cr and Co on top of the SiO_2. Any further detailed interpretation of the voltage x-ray optical properties at the O K-edge needs detailed theoretical calculations, including interface phenomena.

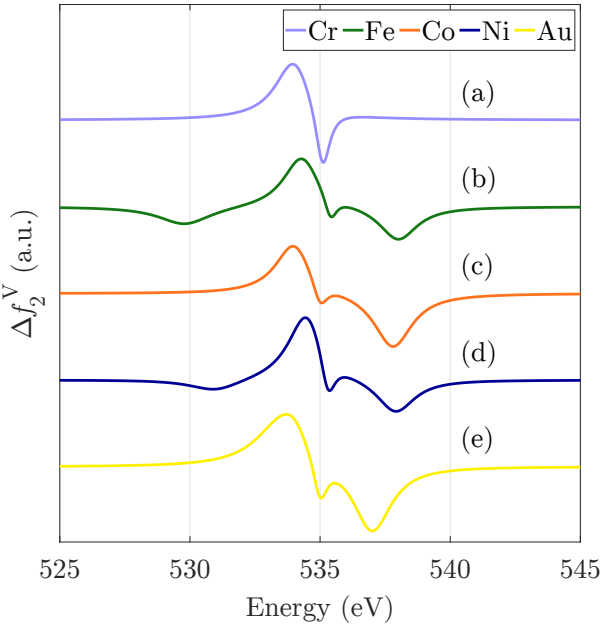

Figure 5.26: Comparison of Δf_2^V at the O K-edge for the upper interface of different samples. The shown spectra belong to the samples with an upper interface consisting of (a) SiO_2/Cr, (b) SiO_2/Fe, (c) SiO_2/Co, (d) SiO_2/Ni, (e) SiO_2/Au.

5.5 Summary

The new experimental technique of voltage x-ray reflectometry (VXRR) was introduced in this chapter. The upgrade (software and hardware) of ERNSt that was necessary to realize this method is described. A scheme for the treatment of VXRR data with *ReMagX* was developed, which enables the simulation of voltage asymmetries similar to magnetic asymmetries that are measured with XRMR. For the simulations, an artificial voltage layer is introduced that represents the interfacial atoms that are affected by the applied voltage. This voltage layer carries the voltage x-ray optical properties Δf_1^{V} and Δf_2^{V}, which are directly related to the change in electronic structure. The position of this voltage layer for interfacial Ni atoms could be determined with an accuracy of $\pm 0.3\,\mathrm{nm}$.

The energy dependence of Δf_1^{V} and Δf_2^{V} at the L_3-edge for Ni atoms at a SiO_2/Ni interface were retrieved. The analysis of the shape and energy position (and comparing it to Ni L-edge XAS spectra) revealed that on average the interfacial Ni atoms slightly change their oxidation state when an electric field is applied. A positive voltage that accumulates holes at the interface leads on average to a higher oxidation state of the interfacial Ni atoms.

Voltage asymmetries measured at the Ni L_3-edge measured with left and right circular polarized x-rays did not show a significant difference, which led to the conclusion that there is (almost) no magnetic component in the voltage x-ray optical properties for Ni at a SiO_2/Ni interface. This result suggests that the interfacial Ni states at the Fermi energy have no or a rather low spin polarization.

A quantitative analysis of the Ni voltage spectra revealed that only about 40 % of the electrons that are moved to (from) the interface by the applied voltage populated (depopulate) Ni states. Thus, the other 60 % of the electrons have to (de)populate states of the other elements at the interface, which in this case are Si and O.

VXRR measurements as function of applied voltage showed a linear response of the sample.

Voltage asymmetry measurements performed at the O K-edge showed a strong signal consisting of two contributions, originating from the Si/SiO_2 and the SiO_2/Ni interface, respectively. The corresponding voltage x-ray properties Δf_1^V and Δf_2^V at the O K-edge have opposite signs for the two interfaces since for a given voltage opposing charges accumulate at those interfaces. However, the general shape of Δf_1^V and Δf_2^V for both interfaces are quite similar. The small differences between them presumably originate from the different chemical surrounding of the O atoms which results in a different electronic structure. The amplitude of the voltage x-ray optical properties is a lot higher for the Si/SiO_2 interface, suggesting that more of the moved electrons (de)populate O states at this interface. The comparison of Δf_2^V with different O K-edge XAS spectra helped to identify how the electronic structure of interfacial O atoms changes by an applied voltage.

VXRR measurements at samples where the Ni layer at the SiO_2/Ni interface was exchanged by different elements (namely Au, Cr, Fe, and Co), revealed similar results for Δf_1^V and Δf_2^V at the O K-edge as the ones obtained for the SiO_2/Ni interface. The small differences that are visible between the spectra obtained from the different samples originate from the different chemical composition at the interfaces, which results in a slight variation of the electronic structure of interfacial O atoms. However, the voltage optical properties for the Si/SiO_2 interface are the same for every sample, which highlights the robustness of the model.

The new experimental method of VXRR has extensive potential for the research of electric-field-induced interfacial effects. For example, by retrieving the voltage x-ray optical parameters of a magnetic TM at the L_3 and L_2-edge with left and right circular polarized light, one could possibly do a similar analysis as the XMCD sum rule analysis. This way, the spin polarization of interfacial states at the Fermi energy could be retrieved

and analyzed in terms of spin and orbital moments. The obtained knowledge could be helpful in the design of future spintronic devices. VXRR is also interesting for devices like MOS-FETs and capacitors since they are inherently built up of interfaces consisting of electrically conducting and non-conducting materials, and electric fields are applied at these interfaces. The knowledge how electrons that move to or from the interface change the electronic structure of interfacial atoms could yield new insights into these systems and help to improve their functionality.

Summary & Outlook

Chapter 6

Summary

In this thesis, current questions regarding depth dependent structural, magnetic, and interfacial properties of magnetic thin film systems were studied. The investigated layered samples, namely sputtered layer stacks of SiO_2/TM/Cr/Au on Si substrates, are similar to systems widely used in typical spintronic devices.

In the first part of the thesis, the resonant (magneto-)optical x-ray parameter of the used materials are retrieved from x-ray absorption spectroscopy (XAS) and x-ray magnetic circular dichroism (XMCD) measurements. Here, the TM L-edges and the O K-edge are of interest for studied samples. The exact knowledge of the resonant optical parameters is a prerequisite for the analysis of the reflectometry data in the second and third part of this thesis.

The second part of the thesis is dedicated to the study of structural and magnetic properties of Si/SiO_2/TM/Cr/Au layer stacks, with the TMs of

interest being Fe, Co, and Ni. XRR and XRMR measurements are utilized in order to retrieve high resolution depth dependent chemical and magnetic properties. The magnetic depth profiles revealed that the magnetization of the nominal 2 nm thick TM layers is reduced at room temperature when compared to quasi bulk 10 nm layers. The magnetization reduction was enhanced at the TM/Cr interface, while the magnetization profile at the SiO_2/TM interface closely followed the chemical depth profile. The overall magnetization reduction showed to be very sensitive to small structural variations that are easily induced by the sputtering process during the sample preparation. The magnetization reduction was quantified by complementary temperature dependent SQUID measurements. A detailed analysis of the measured data revealed different effects leading to the magnetization reduction of the thin layers, namely a reduced effective Curie temperature and intermixing at the interfaces (especially the TM/Cr interface) which results in regions were the magnetization is strongly reduced. The major magnetization reduction effect has its origin in the reduced effective Curie temperature.

In the third and central part of this thesis, the new measurement technique of voltage x-ray reflectometry (VXRR) is presented. VXRR measurements offer the possibility to study element selective electric-field-induced changes in interfacial electronic structures at buried layers. The measurement signal of VXRR experiments are intensity variations of reflected x-rays that are caused by small changes of the x-ray optical parameters at the interface due to electrons (de)populating states at the Fermi energy. The change of x-ray optical properties is directly related to changes in the interfacial electronic structure. Thus, by determining those voltage-induced x-ray optical property changes with VXRR measurement, it becomes possible to measure electric-field-induced changes to interfacial electronic structures.

The first ever VXRR measurements are shown, measured on a sample

with Ni as the TM layer. The electric-field-induced changes to the x-ray optical properties at the Ni L_3-edge and the O K-edge are retrieved. The results at the Ni L_3-edge show that the average oxidation state of interfacial Ni atoms is changed by the applied voltage. Measurements with circular polarized x-rays showed that the interfacial Ni states at the Fermi energy have no measurable spin polarization with the current noise level of the experiment. The quantitative analysis of the obtained voltage x-ray optical properties revealed that only about 40 % of the electrons that are moved to the SiO_2/Ni interface (de)populate Ni states.

A strong electric-field-induced effect in the interfacial electronic structure of O atoms at the Si/SiO_2 and the SiO_2/Ni interface could be measured as well. Furthermore, the retrieved voltage x-ray optical properties at the O K-edge for the Si/SiO_2 interface could be applied to measurements of different samples containing such an interface, demonstrating the universality of the result.

Chapter 7

Outlook

The results obtained from XRMR measurements in this thesis are important to better understand interfacial effects in spintronic devices and might constitute a step towards future devices with improved functionality. Sophisticated interface engineering for such devices could be supported by the detailed knowledge about depth dependent structural and magnetic properties obtained from XRMR measurements. There are plenty of layered systems that are interesting for future XRR and XRMR measurements. For example systematic studies on the CoFeB/MgO interface, which is quite common in spintronic devices. Another possible avenue includes the study of artificial antiferromagnets, where the exact magnetic depth profile of the antiferromagnetically coupled layers could be studied.

The newly developed method of VXRR opens up a completely new way of obtaining information about interfacial electronic structures at buried layers. Following the first studies with VXRR, realized in this thesis, it would be interesting to extend the measurements to other magnetic TMs

such as Fe or Co or multi component magnets as CoFeB. For samples that show spin polarized interfacial states at the Fermi energy, VXRR measurements with circular polarized light at the L_3 and L_2-edges might even allow to separate orbital and spin magnetic moments for those states. This could help to better understand interfacial magnetic effects like PMA and VCMA.

Another interesting path for VXRR would also be to realize measurements where the applied voltage does not oscillate around 0, but rather between 0 and a positive voltage or between 0 and a negative voltage, since the electric-field-induced effect may not be symmetrical. Since adding or removing a charge does not result in the same change in oxidation state, the related changes in the electronic structure are possibly different.

However, VXRR measurements should not be limited to systems that are similar to spintronic devices. There are a variety of systems where VXRR measurements could provide valuable insights into electric-field-induced interfacial effects, for example systems such as MOS-FETs, capacitors, solid-state electrolyte lithium batteries, 2D materials or topological insulators. By further developing VXRR, it may also be possible to study buried interfaces of heavy metals, where the SHE leads to high interfacial spin polarizations when an electric current passes through. Thus, the experimental method of voltage x-ray reflectometry offers a high potential for new insights into many different systems in solid-state research.

Appendix

Appendix A

Frequency dependence of the VXRR Signal Strength

All VXRR measurements shown in this thesis were measured with an AC voltage frequency of 59 Hz. The amplitude response of the experimental setup, shown in Fig.5.4c, showed that there is a amplification of the measured signal of 1.76 at 59 Hz. In order to verify that this amplification actually carries through to the measured VXRR signal, frequency dependent measurements were performed. In Fig. A.1, the normalized frequency dependent VXRR amplitude is shown. It was measured on the 2 nm Ni(II) sample with a photon energy of 534 eV and at a q_z-value of 0.125 $Å^{-1}$. The solid line shows the amplitude response of the experimental setup, as already shown in Fig. 5.4c. The measurements of the VXRR amplitude were done for lock-in frequencies of 10.76 Hz, 40 Hz, 59 Hz, 70 Hz, and 84 Hz, with the corresponding predefined phase at the lock-in, which is shown in Fig. 5.4d. The measured amplitudes are normalized to the values measured at 84 Hz, since for this frequency the amplitude response of

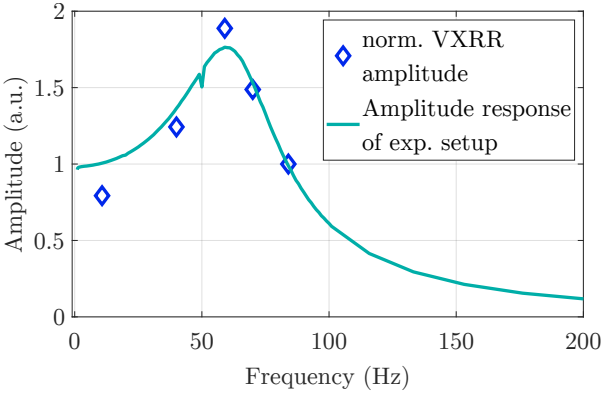

Figure A.1: Frequency dependent VXRR amplitude measured at the Ni sample at a photon energy of 534 eV and a q_z of 0.125 $Å^{-1}$ normalized to the value measured at 84 Hz (blue diamonds). The solid line shows the amplitude response of the experimental setup as shown in Fig. 5.4c.

the experimental setup has a value of 1. The frequency dependent VXRR amplitudes show good agreement with the amplitude response of the experimental setup.

Appendix B

Additional VXRR Data and Fits at the O K-edge for different samples

VXRR measurement results at the O K-edge, the corresponding *ReMagX* fits, the layer profiles including the voltage layers, and the voltage x-ray optical properties for samples which all have an Si/SiO_2 lower interface but different upper interfaces, namely SiO_2/Au, SiO_2/Cr, SiO_2/Fe and SiO_2/Co, are shown below.

Gold Sample

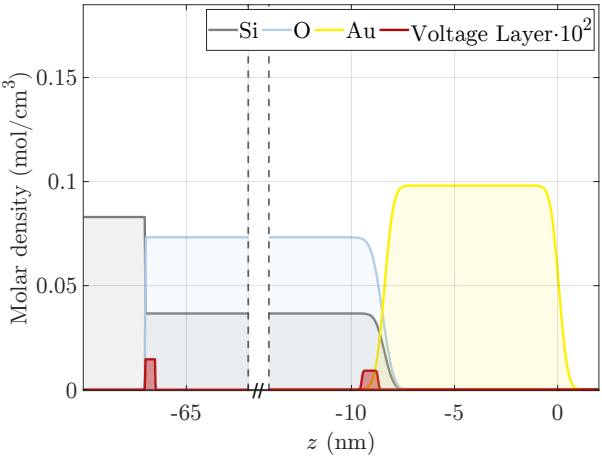

Figure B.1: Elemental depth profile of the sample with only an Au layer on top of the substrate. The voltage layers, which indicates the O atoms that are affected by the applied electric field, are shown in red. The densities of the voltage layers in the plot are multiplied by 100 since it would not be visible otherwise. The upper voltage layer has a density of $9.14 \cdot 10^{-5}\ \frac{\text{mol}}{\text{cm}^3}$ and a thickness of 0.8 nm and the lower one a density of $1.46 \cdot 10^{-4}\ \frac{\text{mol}}{\text{cm}^3}$ and a thickness of 0.5 nm.

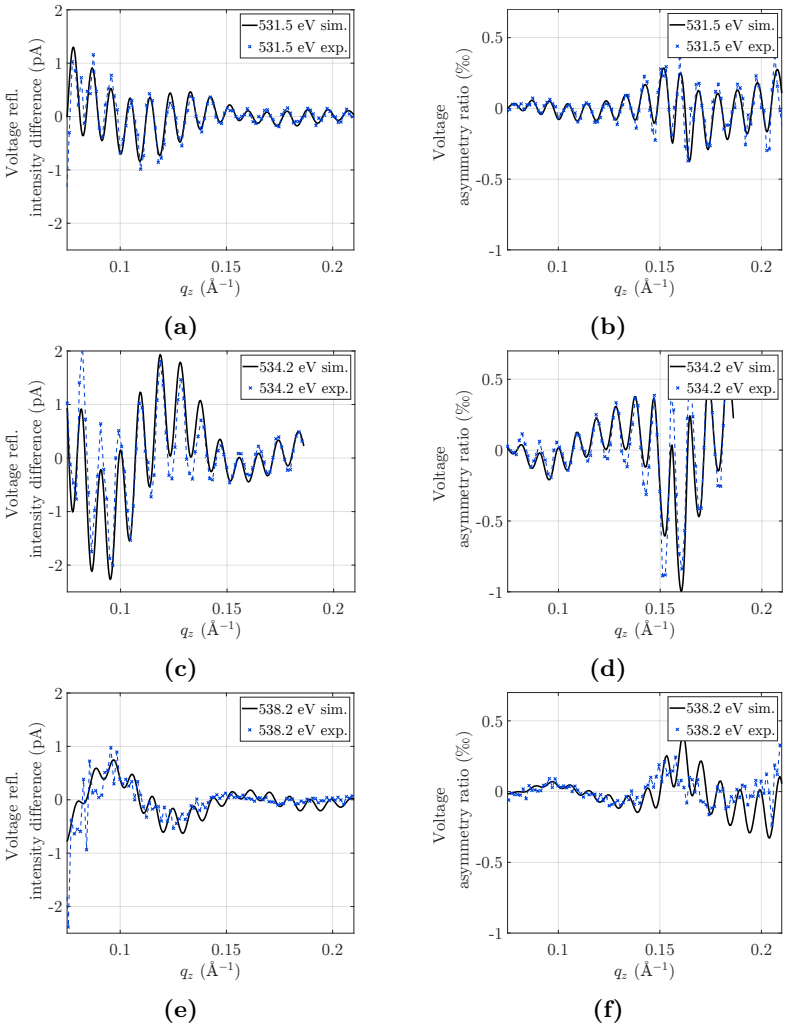

Figure B.2: VXRR constant energy q_z-scans at various photon energies around the O K-edge measured at the sample with only an Au layer on top of the substrate. The left column shows the difference in reflected photo current $I_{\text{lock-in}}$ between positive and negative applied voltage and the right column shows the voltage asymmetry ratio A_{V}. The corresponding *ReMagX* fits are shown as black lines.

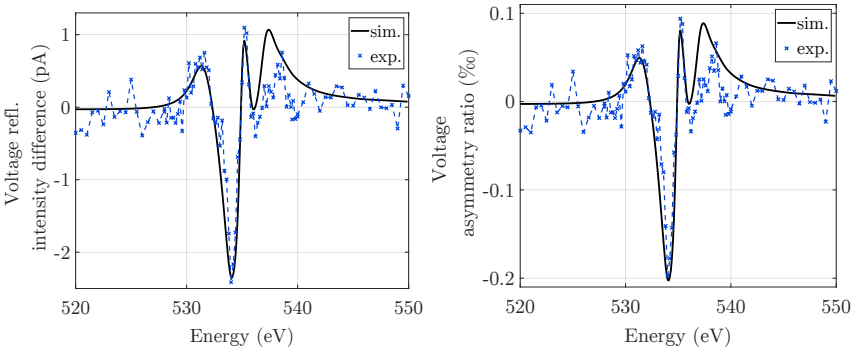

(a) **(b)**

Figure B.3: VXRR constant q_z energy-scan at $q_z = 0.096\,\text{Å}^{-1}$ over the O K-edge measured at the sample with only an Au layer on top of the substrate. The left column shows the difference in reflected photo current $I_{\text{lock-in}}$ between positive and negative applied voltage and the right column shows the voltage asymmetry ratio A_{V}. The corresponding *ReMagX* fits are shown as black lines.

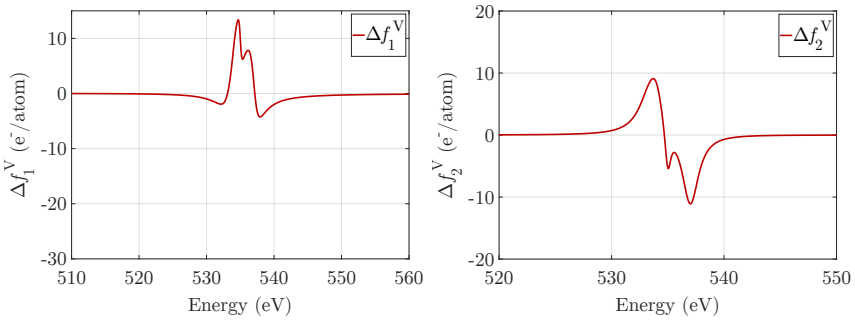

(a) **(b)**

Figure B.4: (a) Real (Δf_1^{V}) and (b) imaginary (Δf_2^{V}) part of the voltage x-ray optical properties at the O K-edge, for the upper voltage layer located at the SiO_2/Au interface.

Chromium Sample

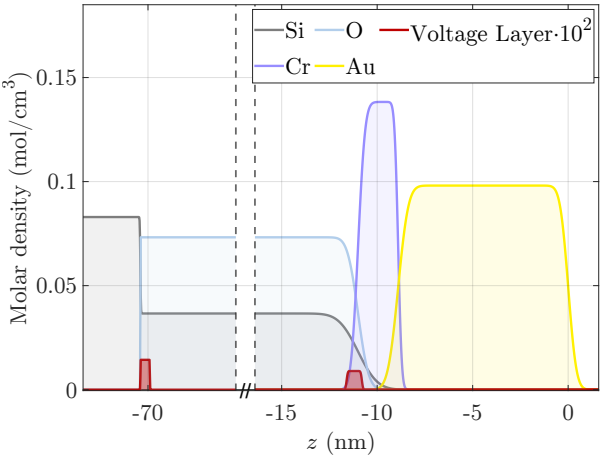

Figure B.5: Elemental depth profile of the sample with a 2 nm Cr and a 10 nm Au layer on top of the substrate. The voltage layers, which indicates the O atoms that are affected by the applied electric field, are shown in red. The densities of the voltage layers in the plot are multiplied by 100 since it would not be visible otherwise. The upper voltage layer has a density of $8.97 \cdot 10^{-5}\ \frac{\text{mol}}{\text{cm}^3}$ and a thickness of 0.8 nm and the lower one a density of $1.44 \cdot 10^{-4}\ \frac{\text{mol}}{\text{cm}^3}$ and a thickness of 0.5 nm.

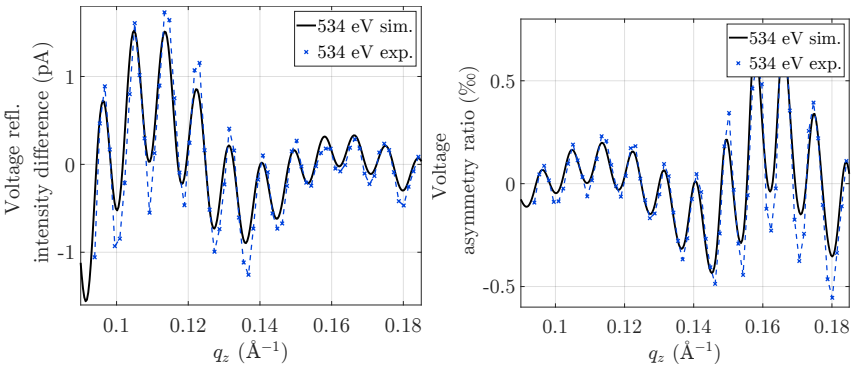

Figure B.6: VXRR constant energy q_z-scans at 534 eV measured at the sample with a 2 nm Cr and a 10 nm Au layer on top of the substrate. On the left the difference in reflected photo current $I_{\text{lock-in}}$ between positive and negative applied voltage is shown and on the right the voltage asymmetry ratio A_{V}. The corresponding *ReMagX* fits are shown as black lines.

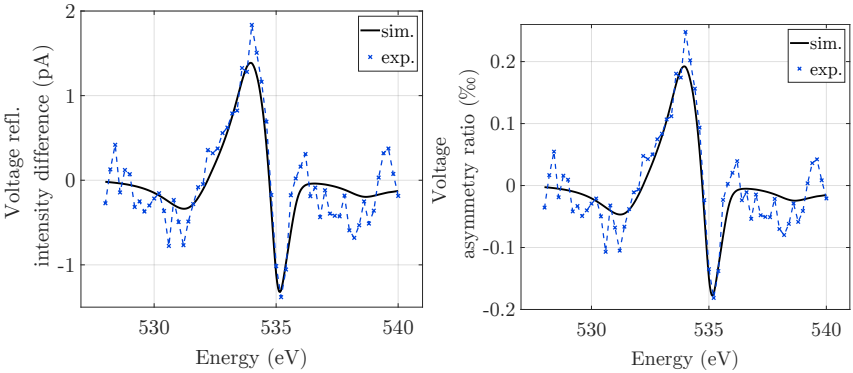

Figure B.7: VXRR constant q_z energy-scan at $q_z = 0.114\,\text{Å}^{-1}$ over the O K-edge measured at the sample with a 2 nm Cr and a 10 nm Au layer on top of the substrate. The left column shows the difference in reflected photo current $I_{\text{lock-in}}$ between positive and negative applied voltage and the right column shows the voltage asymmetry ratio A_{V}. The corresponding *ReMagX* fits are shown as black lines.

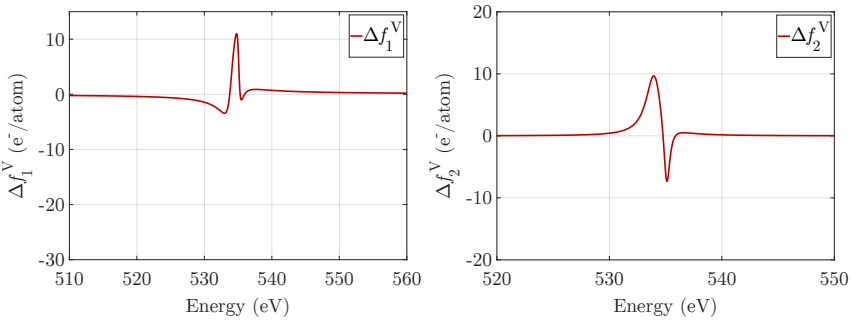

(a) **(b)**

Figure B.8: (a) Real (Δf_1^{V}) and (b) imaginary (Δf_2^{V}) part of the voltage x-ray optical properties at the O K-edge, for the upper voltage layer located at the SiO_2/Cr interface.

Iron Sample

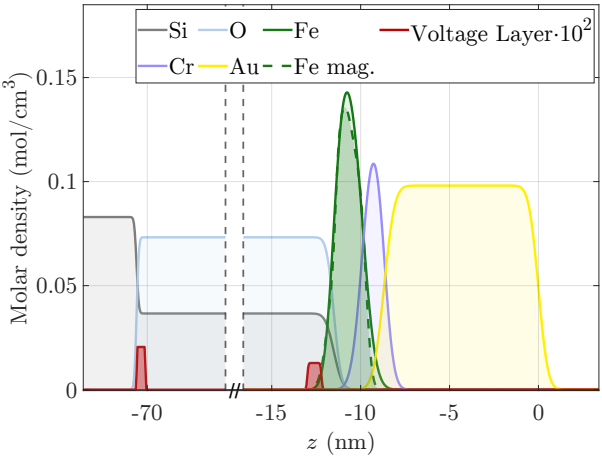

Figure B.9: Elemental and magnetic depth profile of the 2 nm Fe sample (see chapter 4 for details on how they are retrieved). The voltage layers, which indicates the O atoms that are affected by the applied electric field, are shown in red. The densities of the voltage layers in the plot are multiplied by 100 since it would not be visible otherwise. The upper voltage layer has a density of $1.28 \cdot 10^{-4}\ \frac{\text{mol}}{\text{cm}^3}$ and a thickness of 0.8 nm and the lower one a density of $2.05 \cdot 10^{-4}\ \frac{\text{mol}}{\text{cm}^3}$ and a thickness of 0.5 nm.

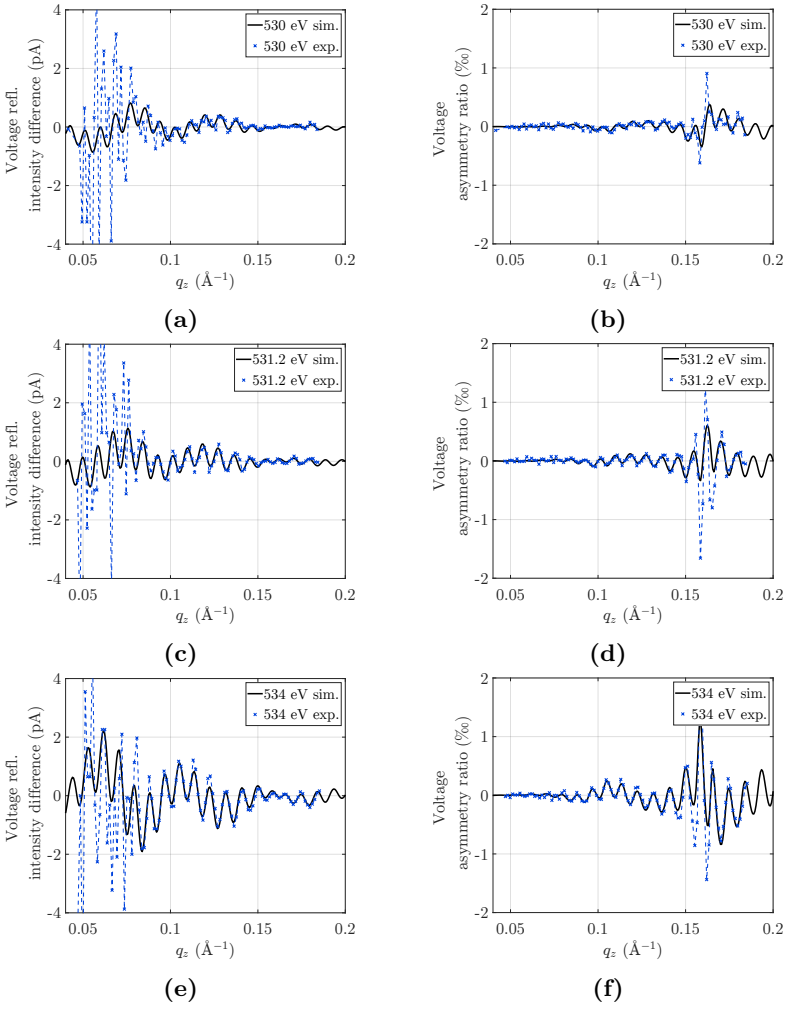

Figure B.10: VXRR constant energy q_z-scans at various photon energies around the O K-edge measured at the 2 nm Fe sample. The left column shows the difference in reflected photo current $I_{\text{lock-in}}$ between positive and negative applied voltage and the right column shows the voltage asymmetry ratio A_{V}. The corresponding *ReMagX* fits are shown as black lines.

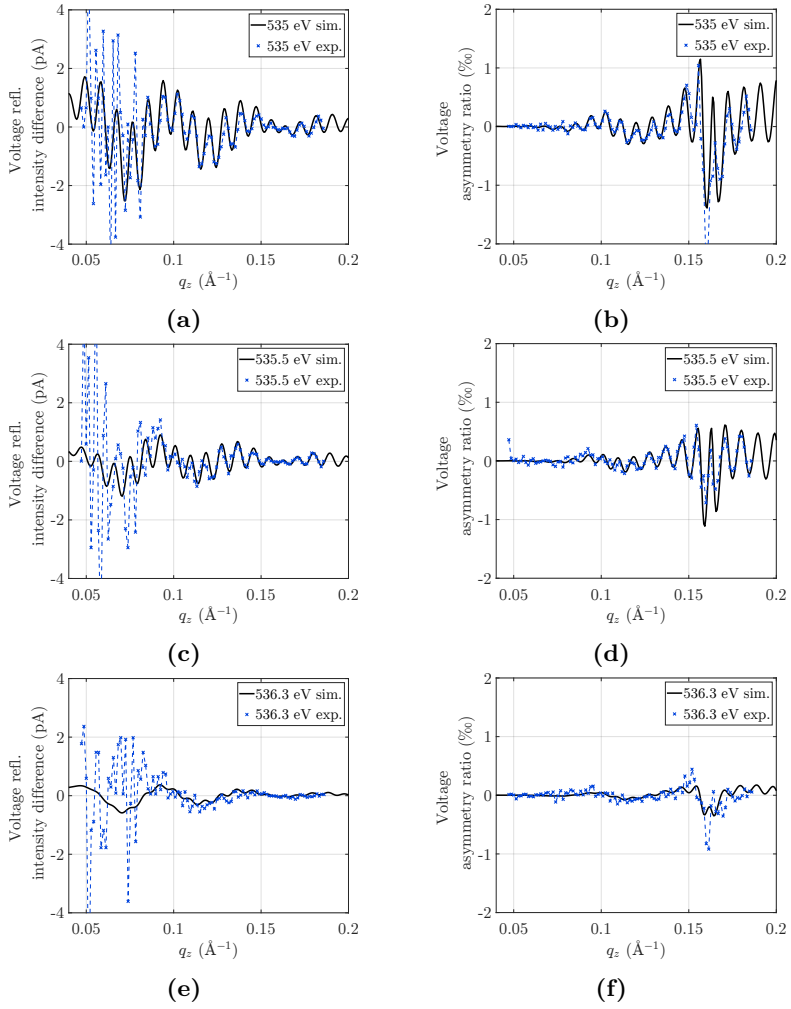

Figure B.11: VXRR constant energy q_z-scans at various photon energies around the O K-edge measured at the 2 nm Fe sample. The left column shows the difference in reflected photo current $I_{\text{lock-in}}$ between positive and negative applied voltage and the right column shows the voltage asymmetry ratio A_{V}. The corresponding *ReMagX* fits are shown as black lines.

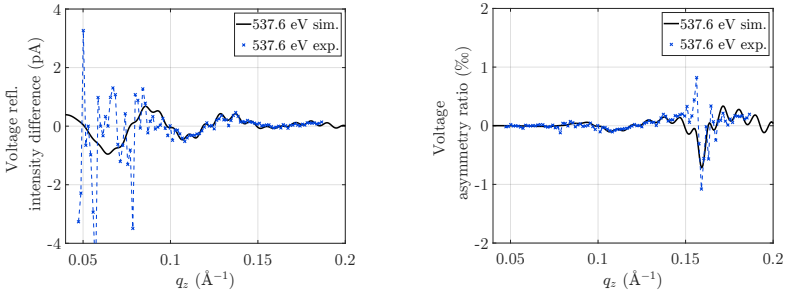

Figure B.12: VXRR constant energy q_z-scans at various photon energies around the O K-edge measured at the 2 nm Fe sample. The left column shows the difference in reflected photo current $I_{\text{lock-in}}$ between positive and negative applied voltage and the right column shows the voltage asymmetry ratio A_{V}. The corresponding *ReMagX* fits are shown as black lines.

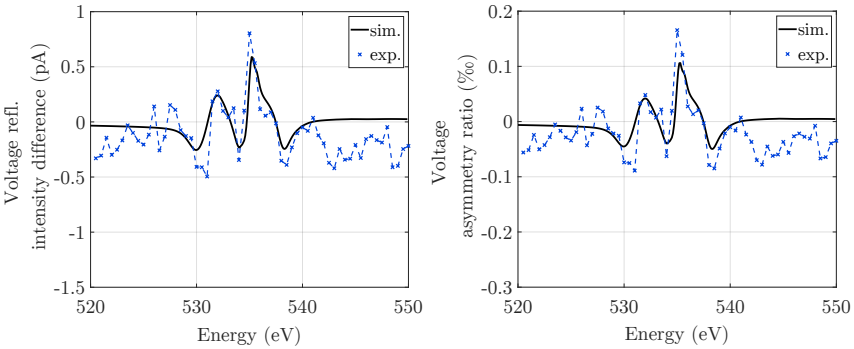

Figure B.13: VXRR constant q_z energy-scan at $q_z = 0.100\,\text{Å}^{-1}$ over the O K-edge measured at the 2 nm Fe(II) sample. The left column shows the difference in reflected photo current $I_{\text{lock-in}}$ between positive and negative applied voltage and the right column shows the voltage asymmetry ratio A_{V}. The corresponding *ReMagX* fits are shown as black lines.

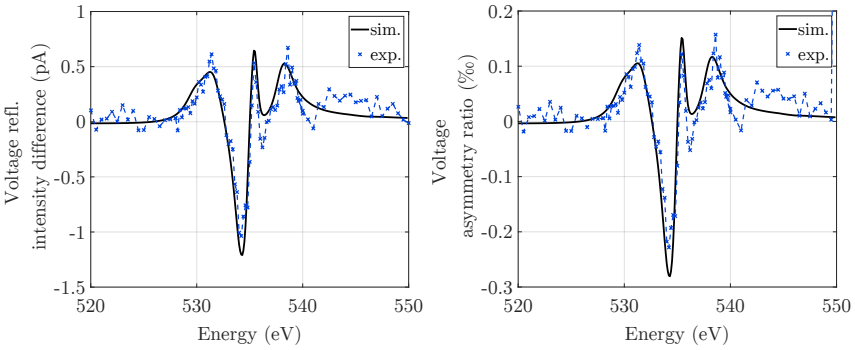

(a) **(b)**

Figure B.14: VXRR constant q_z energy-scan at $q_z = 0.127\,\text{Å}^{-1}$ over the O K-edge measured at the 2 nm Ni(II) sample. The left column shows the difference in reflected photo current $I_{\text{lock-in}}$ between positive and negative applied voltage and the right column shows the voltage asymmetry ratio A_{V}. The corresponding *ReMagX* fits are shown as black lines.

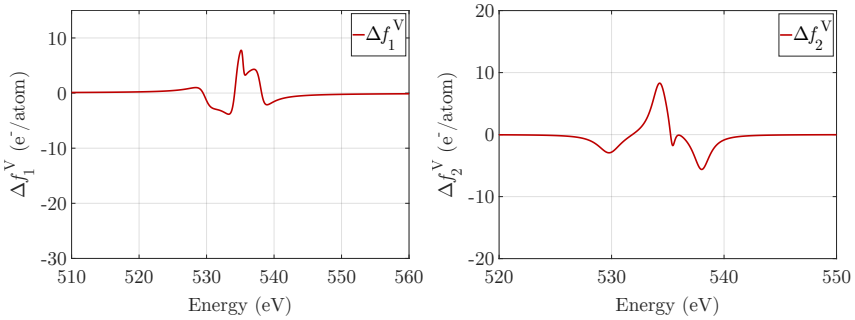

(a) **(b)**

Figure B.15: (a) Real (Δf_1^{V}) and (b) imaginary (Δf_2^{V}) part of the voltage x-ray optical properties at the O K-edge, for the upper voltage layer located at the SiO_2/Fe interface.

Cobalt Sample

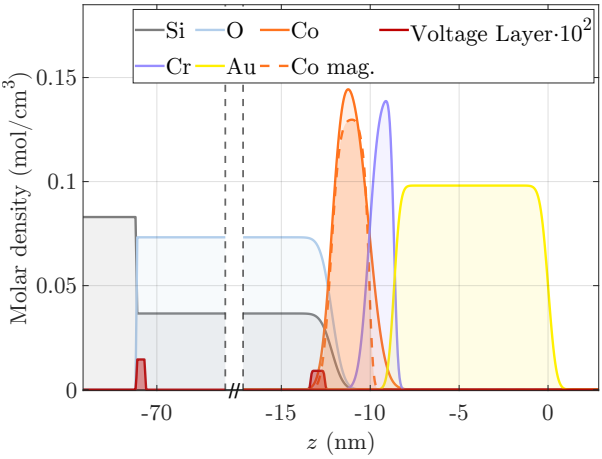

Figure B.16: Elemental and magnetic depth profile of the 2 nm Co(II) sample (see chapter 4 for details on how they are retrieved). The voltage layers, which indicates the O atoms that are affected by the applied electric field, are shown in red. The densities of the voltage layers in the plot are multiplied by 100 since it would not be visible otherwise. The upper voltage layer has a density of $9.08 \cdot 10^{-5}\ \frac{\text{mol}}{\text{cm}^3}$ and a thickness of 0.8 nm and the lower one a density of $1.45 \cdot 10^{-4}\ \frac{\text{mol}}{\text{cm}^3}$ and a thickness of 0.5 nm.

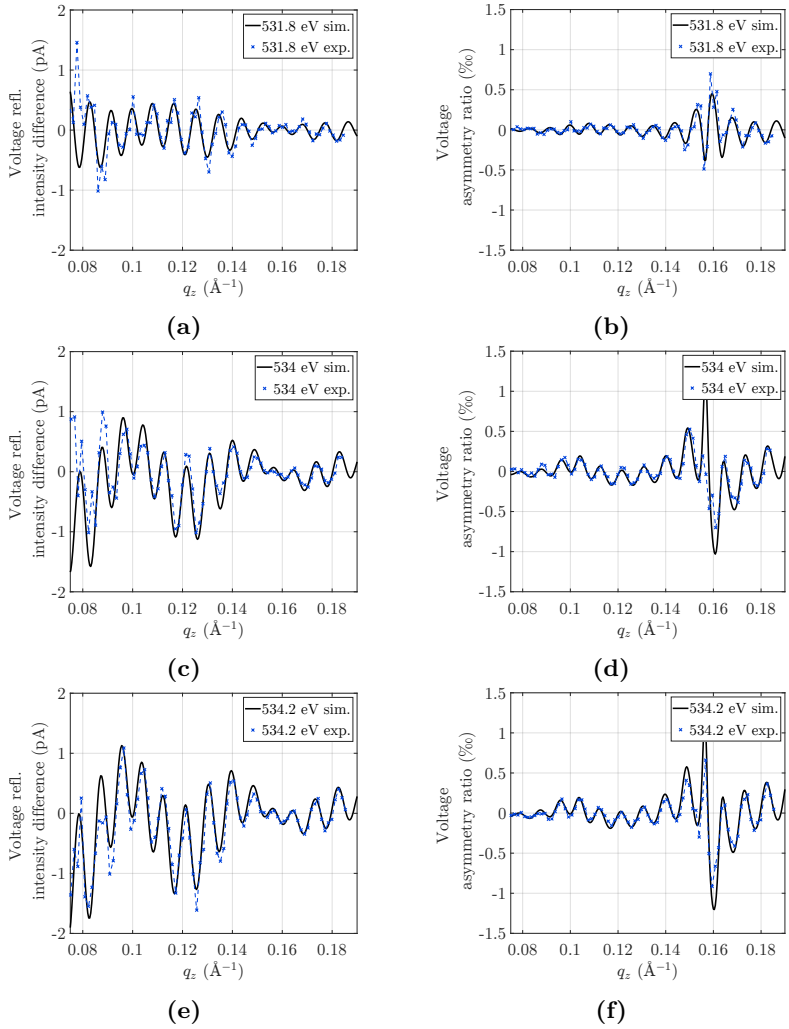

Figure B.17: VXRR constant energy q_z-scans at various photon energies around the O K-edge measured at the 2 nm Co(II) sample. The left column shows the difference in reflected photo current $I_{\text{lock-in}}$ between positive and negative applied voltage and the right column shows the voltage asymmetry ratio A_{V}. The corresponding *ReMagX* fits are shown as black lines.

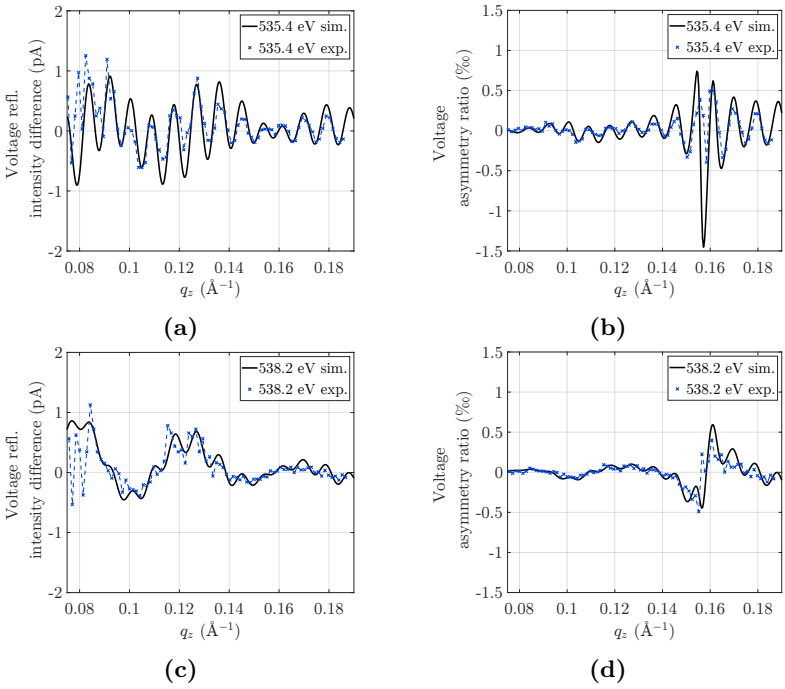

Figure B.18: VXRR constant energy q_z-scans at various photon energies around the O K-edge measured at the 2 nm Co(II) sample. The left column shows the difference in reflected photo current $I_{\text{lock-in}}$ between positive and negative applied voltage and the right column shows the voltage asymmetry ratio A_{V}. The corresponding *ReMagX* fits are shown as black lines.

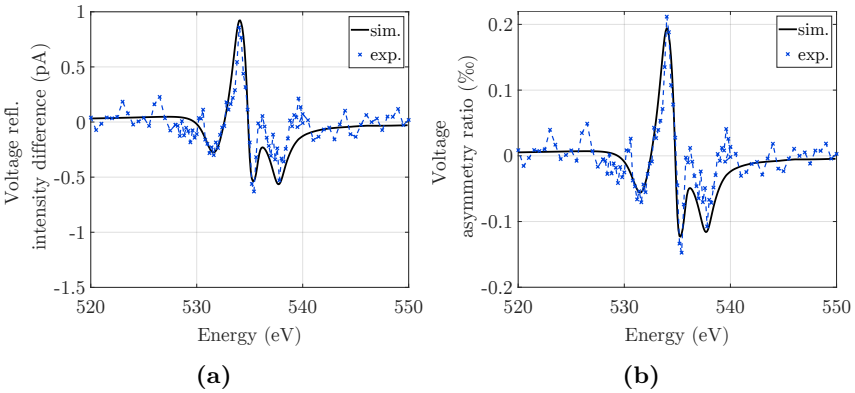

(a) **(b)**

Figure B.19: VXRR constant q_z energy-scan at $q_z = 0.104\,\text{Å}^{-1}$ over the O K-edge measured at the 2 nm Co(II) sample. The left column shows the difference in reflected photo current $I_{\text{lock-in}}$ between positive and negative applied voltage and the right column shows the voltage asymmetry ratio A_{V}. The corresponding *ReMagX* fits are shown as black lines.

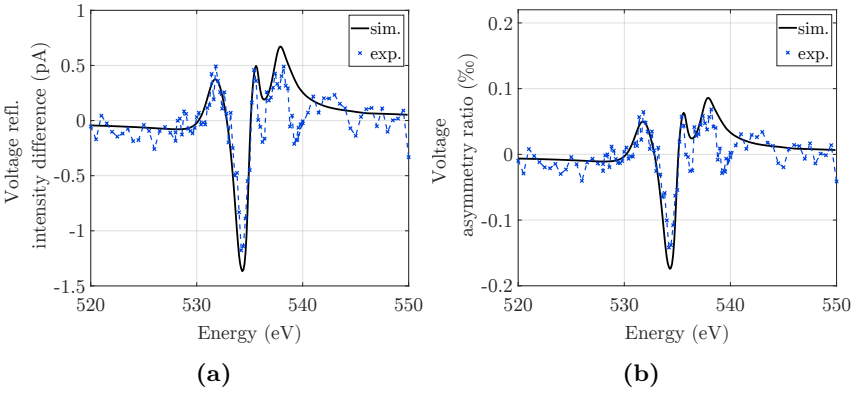

(a) **(b)**

Figure B.20: VXRR constant q_z energy-scan at $q_z = 0.125\,\text{Å}^{-1}$ over the O K-edge measured at the 2 nm Co(II) sample. The left column shows the difference in reflected photo current $I_{\text{lock-in}}$ between positive and negative applied voltage and the right column shows the voltage asymmetry ratio A_{V}. The corresponding *ReMagX* fits are shown as black lines.

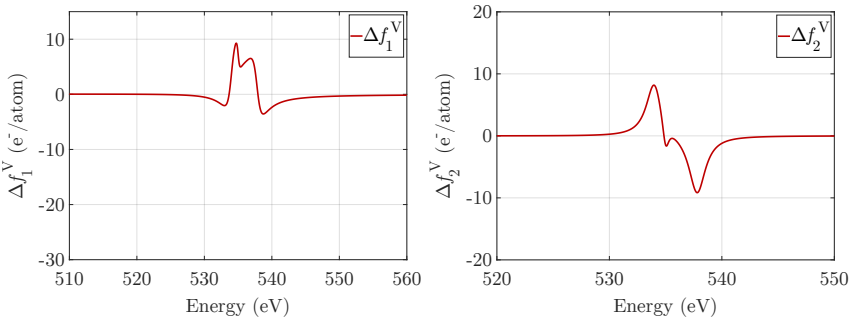

(a) **(b)**

Figure B.21: (a) Real (Δf_1^{V}) and (b) imaginary (Δf_2^{V}) part of the voltage x-ray optical properties at the O K-edge, for the upper voltage layer located at the SiO_2/Co interface.

List of Figures

List of Tables

Bibliography

[1] G. Binasch, P. Grünberg, F. Saurenbach, and W. Zinn, Enhanced magnetoresistance in layered magnetic structures with antiferromagnetic interlayer exchange, Phys. Rev. B **39**, 4828(R) (1989).

[2] M. N. Baibich, J. M. Broto, A. Fert, F. N. Van Dau, F. Petroff, P. Eitenne, G. Creuzet, A. Friederich, and J. Chazelas, Giant magnetoresistance of (001)Fe/(001)Cr magnetic superlattices, Phys. Rev. Lett. **61**, 2472–2475 (1988).

[3] M. Julliere, Tunneling between ferromagnetic films, Phys. Lett. A **54**, 225–226 (1975).

[4] T. Miyazaki and N. Tezuka, Giant magnetic tunneling effect in Fe/Al2O3/Fe junction, J. Magn. Magn. Mater. **139**, L231–L234 (1995).

[5] I. Žutić, J. Fabian, and S. Das Sarma, Spintronics: Fundamentals and applications, Rev. Mod. Phys. **76**, 323–410 (2004).

[6] D. D. Awschalom and M. E. Flatté, Challenges for semiconductor spintronics, Nat. Phys. **3**, 153–159 (2007).

[7] S. D. Bader and S. S. Parkin, Spintronics, Annu. Rev. Condens. Matter Phys. **1**, 71–88 (2010).

[8] J. Sinova and I. Žutić, New moves of the spintronics tango, Nat. Mater. **11**, 368–371 (2012).

[9] A. Hirohata and K. Takanashi, Future perspectives for spintronic devices, J. Phys. D. Appl. Phys. **47**, 193001 (2014).

[10] T. Jungwirth, X. Marti, P. Wadley, and J. Wunderlich, Antiferromagnetic spintronics, Nat. Nanotechnol. **11**, 231–241 (2016).

[11] A. Hirohata, K. Yamada, Y. Nakatani, I.-L. Prejbeanu, B. Diény, P. Pirro, and B. Hillebrands, Review on spintronics: Principles and device applications, J. Magn. Magn. Mater. **509**, 166711 (2020).

[12] M. Dyakonov and V. Perel, Current-induced spin orientation of electrons in semiconductors, Phys. Lett. A **35**, 459–460 (1971).

[13] J. E. Hirsch, Spin Hall Effect, Phys. Rev. Lett. **83**, 1834–1837 (1999).

[14] Z. Wen, H. Sukegawa, T. Seki, T. Kubota, K. Takanashi, and S. Mitani, Voltage control of magnetic anisotropy in epitaxial Ru/Co2FeAl/MgO heterostructures, Sci. Rep. **7**, 45026 (2017).

[15] T. Nozaki, A. Kozioł-Rachwał, M. Tsujikawa, Y. Shiota, X. Xu, T. Ohkubo, T. Tsukahara, S. Miwa, M. Suzuki, S. Tamaru, H. Kubota, A. Fukushima, K. Hono, M. Shirai, Y. Suzuki, and S. Yuasa, Highly efficient voltage control of spin and enhanced interfacial perpendicular magnetic anisotropy in iridium-doped Fe/MgO magnetic tunnel junctions, NPG Asia Mater. **9**, e451 (2017).

[16] D. Ralph and M. Stiles, Spin transfer torques, J. Magn. Magn. Mater. **320**, 1190–1216 (2008).

[17] M. A. Khan, J. Sun, B. Li, A. Przybysz, and J. Kosel, Magnetic sensors-A review and recent technologies, Eng. Res. Express **3**, 022005 (2021).

[18] Sining Mao, Yonghua Chen, Feng Liu, Xingfu Chen, Bin Xu, Puling Lu, M. Patwari, Haiwen Xi, Clif Chang, B. Miller, D. Menard, B. Pant, J. Loven, K. Duxstad, Shaoping Li, Zhengyong Zhang, A. Johnston, R. Lamberton, M. Gubbins, T. McLaughlin, J. Gadbois, Juren Ding, B. Cross, Song Xue, and P. Ryan, Commercial TMR heads for hard disk drives: characterization and extendibility at 300 gbit 2, IEEE Trans. Magn. **42**, 97–102 (2006).

[19] H. Maehara, H. Kubota, Y. Suzuki, T. Seki, K. Nishimura, Y. Nagamine, K. Tsunekawa, A. Fukushima, H. Arai, T. Taniguchi, H. Imamura, K. Ando, and S. Yuasa, High Q factor over 3000 due to out-of-plane precession in nano-contact spin-torque oscillator based on magnetic tunnel junctions, Appl. Phys. Express **7**, 023003 (2014).

[20] W. A. Borders, H. Akima, S. Fukami, S. Moriya, S. Kurihara, Y. Horio, S. Sato, and H. Ohno, Analogue spin–orbit torque device for artificial-neural-network-based associative memory operation, Appl. Phys. Express **10**, 013007 (2017).

[21] M. Zahedinejad, A. A. Awad, S. Muralidhar, R. Khymyn, H. Fulara, H. Mazraati, M. Dvornik, and J. Åkerman, Two-dimensional mutually synchronized spin Hall nano-oscillator arrays for neuromorphic computing, Nat. Nanotechnol. **15**, 47–52 (2020).

[22] S. S. P. Parkin, M. Hayashi, and L. Thomas, Magnetic Domain-Wall Racetrack Memory, Science, **320**, 190–194 (2008).

[23] S. Parkin and S.-H. Yang, Memory on the racetrack, Nat. Nanotechnol. **10**, 195–198 (2015).

[24] S. Bhatti, R. Sbiaa, A. Hirohata, H. Ohno, S. Fukami, and S. N. Piramanayagam, Spintronics based random access memory: a review, Mater. Today **20**, 530–548 (2017).

[25] S. Ikegawa, F. B. Mancoff, J. Janesky, and S. Aggarwal, Magnetoresistive Random Access Memory: Present and Future, IEEE Trans. Electron Devices **67**, 1407–1419 (2020).

[26] J. Åkerman, Toward a universal memory, Science, **308**, 508–510 (2005).

[27] M. Kac, A. Dobrowolska, A. Polit, J. Żukrowski, and M. Marszalek, The influence of the atomic scale interface roughness on the GMR effect in Fe/Cr multilayers, J. Alloys Compd. **824**, 153877 (2020).

[28] L. C. Nagamine, A. Biondo, L. G. Pereira, A. Mello, J. E. Schmidt, T. W. Chimendes, J. B. Cunha, and E. B. Saitovitch, Effect of interface intermixing on giant magnetoresistance in NiFe/Cu and Co/NiFe/Co/Cu multilayers, J. Appl. Phys. **94**, 5881–5890 (2003).

[29] L. O'Brien, M. J. Erickson, D. Spivak, H. Ambaye, R. J. Goyette, V. Lauter, P. A. Crowell, and C. Leighton, Kondo physics in nonlocal metallic spin transport devices, Nat. Commun. **5**, 3927 (2014).

[30] J. Bass and W. P. Pratt, Spin-diffusion lengths in metals and alloys, and spin-flipping at metal/metal interfaces: An experimentalist's critical review, J. Phys. Condens. Matter **19**, 183201 (2007).

[31] B. Dieny, Giant magnetoresistance in spin-valve multilayers, J. Magn. Magn. Mater. **136**, 335–359 (1994).

[32] J. Liu, T. Ohkubo, S. Mitani, K. Hono, and M. Hayashi, Correlation between the spin Hall angle and the structural phases of early 5 d transition metals, Appl. Phys. Lett. **107**, 10.1063/1.4937452 (2015).

[33] J. Geissler, E. Goering, M. Justen, F. Weigand, G. Schütz, J. Langer, D. Schmitz, H. Maletta, and R. Mattheis, Pt magnetization profile in a Pt/Co bilayer studied by resonant magnetic x-ray reflectometry, Phys. Rev. B **65**, 020405(R) (2001).

[34] H. L. Meyerheim, J. M. Tonnerre, L. Sandratskii, H. C. N. Tolentino, M. Przybylski, Y. Gabi, F. Yildiz, X. L. Fu, E. Bontempi, S. Grenier, and J. Kirschner, New model for magnetism in ultrathin fcc Fe on Cu(001), Phys. Rev. Lett. **103**, 267202 (2009).

[35] S. Macke and E. Goering, Magnetic reflectometry of heterostructures, J. Phys. Condens. Matter **26**, 363201 (2014).

[36] S. Macke, A. Radi, J. E. Hamann-Borrero, A. Verna, M. Bluschke, S. Brück, E. Goering, R. Sutarto, F. He, G. Cristiani, M. Wu, E. Benckiser, H. U. Habermeier, G. Logvenov, N. Gauquelin, G. A. Botton, A. P. Kajdos, S. Stemmer, G. A. Sawatzky, M. W. Haverkort, B. Keimer, and V. Hinkov, Element specific monolayer depth profiling, Adv. Mater. **26**, 6554–6559 (2014).

[37] J. Bertinshaw, S. Brück, D. Lott, H. Fritzsche, Y. Khaydukov, O. Soltwedel, T. Keller, E. Goering, P. Audehm, D. L. Cortie, W. D. Hutchison, Q. M. Ramasse, M. Arredondo, R. Maran, V. Nagarajan, F. Klose, and C. Ulrich, Element-specific depth profile of magnetism and stoichiometry at the La0.67 Sr0.33 MnO3/ BiFeO3 interface, Phys. Rev. B **90**, 041113(R) (2014).

[38] P. Audehm, M. Schmidt, S. Brück, T. Tietze, J. Gräfe, S. Macke, G. Schütz, and E. Goering, Pinned orbital moments-A new contribution to magnetic anisotropy, Sci. Rep. **6**, 25517 (2016).

[39] D. Graulich, J. Krieft, A. Moskaltsova, J. Demir, T. Peters, T. Pohlmann, F. Bertram, J. Wollschläger, J. R. Jose, S. Francoual, and T. Kuschel, Quantitative comparison of the magnetic proximity

effect in Pt detected by XRMR and XMCD, Appl. Phys. Lett. **118**, 012407 (2021).

[40] S. Brück, M. Paul, H. Tian, A. Müller, D. Kufer, C. Praetorius, K. Fauth, P. Audehm, E. Goering, J. Verbeeck, G. Van Tendeloo, M. Sing, and R. Claessen, Magnetic and electronic properties of the interface between half metallic Fe3O4 and semiconducting ZnO, Appl. Phys. Lett. **100**, 081603 (2012).

[41] E. Benckiser, M. W. Haverkort, S. Brück, E. Goering, S. Macke, A. Frañó, X. Yang, O. K. Andersen, G. Cristiani, H. U. Habermeier, A. V. Boris, I. Zegkinoglou, P. Wochner, H. J. Kim, V. Hinkov, and B. Keimer, Orbital reflectometry of oxide heterostructures, Nat. Mater. **10**, 189–193 (2011).

[42] P. Radhakrishnan, B. Geisler, K. Fürsich, D. Putzky, Y. Wang, S. E. Ilse, G. Christiani, G. Logvenov, P. Wochner, P. A. Van Aken, E. Goering, R. Pentcheva, and E. Benckiser, Orbital engineering in YVO_3-LaAl O_3 superlattices, Phys. Rev. B **104**, L121102 (2021).

[43] M. Wu, E. Benckiser, P. Audehm, E. Goering, P. Wochner, G. Christiani, G. Logvenov, H. U. Habermeier, and B. Keimer, Orbital reflectometry of $PrNiO_3/PrAlO_3$ superlattices, Phys. Rev. B **91**, 195130 (2015).

[44] E. Benckiser, Y. Khaydukov, L. Guasco, K. Fürsich, P. Radhakrishnan, G. Kim, and B. Keimer, Complementary Insights from Neutron and Resonant X-Ray Reflectometry for the Study of Perovskite Transition Metal Oxide Heterostructures, Phys. Status Solidi Basic Res. **259**, 2100253 (2022).

[45] C. Zhan, C. Lian, Y. Zhang, M. W. Thompson, Y. Xie, J. Wu, P. R. C. Kent, P. T. Cummings, D. Jiang, and D. J. Wesolowski, Computational Insights into Materials and Interfaces for Capacitive Energy Storage, Adv. Sci. **4**, 1700059 (2017).

[46] H. Luo, X. Zhou, C. Ellingford, Y. Zhang, S. Chen, K. Zhou, D. Zhang, C. R. Bowen, and C. Wan, Interface design for high energy density polymer nanocomposites, Chem. Soc. Rev. **48**, 4424–4465 (2019).

[47] H. Deuling, E. Klausmann, and A. Goetzberger, Interface states in Si-SiO_2 interfaces, Solid. State. Electron. **15**, 559–571 (1972).

[48] D. A. Muller, T. Sorsch, S. Moccio, F. H. Baumann, K. Evans-Lutterodt, and G. Timp, The electronic structure at the atomic scale of ultrathin gate oxides, Nature **399**, 758–761 (1999).

[49] S. Dimitrijev and P. Jamet, Advances in SiC power MOSFET technology, Microelectron. Reliab. **43**, 225–233 (2003).

[50] J. Haruyama, K. Sodeyama, L. Han, K. Takada, and Y. Tateyama, Space–Charge Layer Effect at Interface between Oxide Cathode and Sulfide Electrolyte in All-Solid-State Lithium-Ion Battery, Chem. Mater. **26**, 4248–4255 (2014).

[51] M. Sumita, Y. Tanaka, M. Ikeda, and T. Ohno, Charged and Discharged States of Cathode/Sulfide Electrolyte Interfaces in All-Solid-State Lithium Ion Batteries, J. Phys. Chem. C **120**, 13332–13339 (2016).

[52] Z. Gao, H. Sun, L. Fu, F. Ye, Y. Zhang, W. Luo, and Y. Huang, Promises, Challenges, and Recent Progress of Inorganic Solid-State Electrolytes for All-Solid-State Lithium Batteries, Adv. Mater. **30**, 1705702 (2018).

[53] J. E. Moore, The birth of topological insulators, Nature **464**, 194–198 (2010).

[54] Y. Tokura, K. Yasuda, and A. Tsukazaki, Magnetic topological insulators, Nat. Rev. Phys. **1**, 126–143 (2019).

[55] P. Miró, M. Audiffred, and T. Heine, An atlas of two-dimensional materials, Chem. Soc. Rev. **43**, 6537–6554 (2014).

[56] J. Stöhr and H. C. Siegmann, *Magnetism: From fundamentals to nanoscale dynamics*, Vol. 152 (Springer Berlin Heidelberg, 2006) pp. 1–822.

[57] E. C. Stoner, Collective electron specific heat and spin paramagnetism in metals, Proc. R. Soc. A Math. Phys. Sci. **154**, 656–678 (1936).

[58] E. C. Stoner, Collective electron ferronmagnetism, Proc. R. Soc. A Math. Phys. Sci. **165**, 372–414 (1938).

[59] P. Weiss, L'hypothèse du champ moléculaire et la propriété ferromagnétique, J. Phys. **6**, 661–690 (1907).

[60] W. Heisenberg, Zur Theorie des Ferromagnetismus, Zeitschrift für Phys. **49**, 619–636 (1928).

[61] S. Blundell, *Magnetism in condensed Matter* (Oxford University Press, 2001).

[62] D. Mauri, D. Scholl, H. C. Siegmann, and E. Kay, Observation of the Exchange Interaction at the Surface of a Ferromagnet, Phys. Rev. Lett. **61**, 758–761 (1988).

[63] C. A. Vaz, J. A. Bland, and G. Lauhoff, Magnetism in ultrathin film structures, Reports Prog. Phys. **71**, 056501 (2008).

[64] U. Gradmann, Chapter 1 Magnetism in ultrathin transition metal films, in *Handb. Magn. Mater.*, Vol. 7 (Elsevier, 1993) pp. 1–96.

[65] P. Srivastava, F. Wilhelm, A. Ney, M. Farle, H. Wende, N. Haack, G. Ceballos, and K. Baberschke, Magnetic moments and Curie temperatures of Ni and Co thin films and coupled trilayers, Phys. Rev. B **58**, 5701–5706 (1998).

[66] P. J. Jensen, H. Dreyssé, and K. H. Bennemann, Thickness dependence of the magnetization and the Curie temperature of ferromagnetic thin films, Surf. Sci. **269-270**, 627–631 (1992).

[67] J. A. Osborn, Demagnetizing Factors of the General Ellipsoid, Phys. Rev. **67**, 351 (1945).

[68] M. Sato and Y. Ishii, Simple and approximate expressions of demagnetizing factors of uniformly magnetized rectangular rod and cylinder, J. Appl. Phys. **66**, 983–985 (1989).

[69] P. Bruno, Tight-binding approach to the orbital magnetic moment and magnetocrystalline anisotropy of transition-metal monolayers, Phys. Rev. B **39**, 865(R) (1989).

[70] D. Weller, J. Stöhr, R. Nakajima, A. Carl, M. G. Samant, C. Chappert, R. Mégy, P. Beauvillain, P. Veillet, and G. A. Held, Microscopic origin of magnetic anisotropy in Au/Co/Au probed with X-ray magnetic circular dichroism, Phys. Rev. Lett. **75**, 3752–3755 (1995).

[71] E. Goering, A. Bayer, S. Gold, G. Schütz, M. Rabe, U. Rüdiger, and G. Güntherodt, Strong Anisotropy of Projected 3d Moments in Epitaxial CrO_2 Films, Phys. Rev. Lett. **88**, 207203 (2002).

[72] C. Chappert, K. L. Dang, P. Beauvillain, H. Hurdequint, and D. Renard, Ferromagnetic resonance studies of very thin cobalt films on a gold substrate, Phys. Rev. B **34**, 3192–3197 (1986).

[73] M. Stampanoni, A. Vaterlaus, M. Aeschlimann, and F. Meier, Magnetism of epitaxial bcc iron on Ag(001) observed by spin-polarized photoemission, Phys. Rev. Lett. **59**, 2483–2485 (1987).

[74] D. Chantler, C.T., Olsen, K., Dragoset, R.A., Chang, J., Kishore, A.R., Kotochigova, S.A., and Zucker, X-Ray Form Factor, Attenuation and Scattering Tables (version 2.1) (2005).

[75] B. L. Henke, E. M. Gullikson, and J. C. Davis, X-ray interactions: Photoabsorption, scattering, transmission, and reflection at E = 50-30, 000 eV, Z = 1-92 (1993).

[76] J. Yano and V. K. Yachandra, X-ray absorption spectroscopy, Photosynth. Res. **102**, 241–254 (2009).

[77] C. Ahn, *Transmission Electron Energy Loss Spectrometry in Materials Science and the EELS Atlas* (John Wiley & Sons, 2006).

[78] E. Stavitski and F. M. de Groot, The CTM4XAS program for EELS and XAS spectral shape analysis of transition metal L edges, Micron **41**, 687–694 (2010).

[79] G. van der Laan, Line shape of 2p magnetic-x-ray-dichroism spectra in 3d metallic systems, Phys. Rev. B **55**, 8086–8089 (1997).

[80] B. K. Agarwal and L. P. Verma, A rule for chemical shifts of X-ray absorption edges, J. Phys. C Solid State Phys. **3**, 535–537 (1970).

[81] J. S. Kang, G. Kim, H. J. Lee, D. H. Kim, H. S. Kim, J. H. Shim, S. Lee, H. Lee, J. Y. Kim, B. H. Kim, and B. I. Min, Soft x-ray absorption spectroscopy and magnetic circular dichroism study of the valence and spin states in spinel $MnFe_2O_4$, Phys. Rev. B **77**, 035121 (2008).

[82] G. Cressey, C. M. Henderson, and G. van der Laan, Use of L-edge X-ray absorption spectroscopy to characterize multiple valence states of 3 d transition metals; a new probe for mineralogical and geochemical research, Phys. Chem. Miner. **20**, 111–119 (1993).

[83] H. Tan, J. Verbeeck, A. Abakumov, and G. Van Tendeloo, Oxidation state and chemical shift investigation in transition metal oxides by EELS, Ultramicroscopy **116**, 24–33 (2012).

[84] L. A. Garvie, A. J. Craven, and R. Brydson, Use of electron-energy loss near-edge fine structure in the study of minerals, Am. Mineral. **79**, 411–425 (1994).

[85] T. J. Regan, H. Ohldag, C. Stamm, F. Nolting, J. Lüning, J. Stöhr, and R. L. White, Chemical effects at metal/oxide interfaces studied by x-ray-absorption spectroscopy, Phys. Rev. B **64**, 214422 (2001).

[86] H. Wang, D. S. Patil, W. Gu, L. Jacquamet, S. Friedrich, T. Funk, and S. P. Cramer, L-edge X-ray absorption spectroscopy of some Ni enzymes: Probe of Ni electronic structure, J. Electron Spectros. Relat. Phenomena **114-116**, 855–863 (2001).

[87] H. Liu, M. Bugnet, M. Z. Tessaro, K. J. Harris, M. J. Dunham, M. Jiang, G. R. Goward, and G. A. Botton, Spatially resolved surface valence gradient and structural transformation of lithium transition metal oxides in lithium-ion batteries, Phys. Chem. Chem. Phys. **18**, 29064–29075 (2016).

[88] S. Gota, F. Jollet, J. P. Crocombette, Z. Y. Wu, M. Pollak, N. Thromat, M. Gautier-Soyer, and C. R. Natoli, Characterization of iron oxides by XAS at the Fe $L_{2,3}$ and O K edges, J. Phys. IV JP **7**, 507–508 (1997).

[89] F. Frati, M. O. Hunault, and F. M. De Groot, Oxygen K-edge X-ray Absorption Spectra, Chem. Rev. **120**, 4056–4110 (2020).

[90] G. Schütz, W. Wagner, W. Wilhelm, P. Kienle, R. Zeller, R. Frahm, and G. Materlik, Absorption of circularly polarized x rays in iron, Phys. Rev. Lett. **58**, 737–740 (1987).

[91] C. T. Chen, N. V. Smith, and F. Sette, Exchange, spin-orbit, and correlation effects in the soft-x-ray magnetic-circular-dichroism spectrum of nickel, Phys. Rev. B **43**, 6785 (1991).

[92] C. T. Chen, Y. U. Idzerda, H. J. Lin, N. V. Smith, G. Meigs, E. Chaban, G. H. Ho, E. Pellegrin, and F. Sette, Experimental confirmation of the x-ray magnetic circular dichroism sum rules for iron and cobalt, Phys. Rev. Lett. **75**, 152 (1995).

[93] B. T. Thole, P. Carra, F. Sette, and G. Van Der Laan, X-ray circular dichroism as a probe of orbital magnetization, Phys. Rev. Lett. **68**, 1943–1946 (1992).

[94] P. Carra, B. T. Thole, M. Altarelli, and X. Wang, X-ray circular dichroism and local magnetic fields, Phys. Rev. Lett. **70**, 694–697 (1993).

[95] E. J. Jaeschke, S. Khan, J. R. Schneider, and J. B. Hastings, *Synchrotron light sources and free-electron lasers: accelerator physics, instrumentation and science applications* (springer, 2016).

[96] D. Attwood, *Soft x-rays and extreme ultraviolet radiation: principles and applications* (Cambridge University Press, 1999).

[97] A. Thompson, D. Attwood, E. Gullikson, M. Howells, K.-J. Kim, J. Kirz, J. Kortright, I. Lindau, Y. Liu, P. Pianetta, A. Robinson, J. Scofield, J. Underwood, G. Williams, and H. Winick, *X-Rray Data Booklet* (Lawrence Berkeley National Laboratory, University of California Berkeley, CA, 2009).

[98] S. Calvin, *XAFS for Everyone* (CRC press, 2013).

[99] F. D. Groot, High-Resolution X-ray Emission and X-ray Absorption Spectroscopy, Chem. Rev. **101**, 1779–1808 (2001).

[100] J. Stöhr and Y. Wu, X-Ray Magnetic Circular Dichroism: Basic Concepts and Theory for 3D Transition Metal Atoms, in *New Dir. Res. with Third-Generation Soft X-Ray Synchrotron Radiat. Sources* (Springer Netherlands, 1994) pp. 221–250.

[101] G. Schütz, E. Goering, and H. Stoll, Synchrotron Radiation Techniques Based on X-ray Magnetic Circular Dichroism, in *Handb. Magn. Adv. Magn. Mater. (eds H. Kronmüller, S. Park. R. Wiesendanger G. Guntherodt)* (John Wiley and Sons, Ltd, 2007).

[102] R. G. Newton, Optical theorem and beyond, Am. J. Phys. **44**, 639–642 (1976).

[103] S. Brück, S. Bauknecht, B. Ludescher, E. Goering, and G. Schütz, An advanced magnetic reflectometer, Rev. Sci. Instrum. **79**, 083109 (2008).

[104] E. Goering, S. Gold, A. Bayer, and G. Schuetz, Non-symmetric influences in the total electron yield X-ray magnetic circular dichroism signal in applied magnetic fields, J. Synchrotron Radiat. **8**, 434–436 (2001).

[105] S. Miwa, K. Matsuda, K. Tanaka, Y. Kotani, M. Goto, T. Nakamura, and Y. Suzuki, Voltage-controlled magnetic anisotropy in Fe|MgO tunnel junctions studied by x-ray absorption spectroscopy, Appl. Phys. Lett. **107**, 162402 (2015).

[106] T. Tsukahara, T. Kawabe, K. Shimose, T. Furuta, R. Miyakaze, K. Nawaoka, M. Goto, T. Nozaki, S. Yuasa, Y. Kotani, K. Toyoki, M. Suzuki, T. Nakamura, Y. Suzuki, and S. Miwa, Characterization of the magnetic moments of ultrathin Fe film in an external electric field via high-precision X-ray magnetic circular dichroism spectroscopy, Jpn. J. Appl. Phys. **56**, 060304 (2017).

[107] T. Kawabe, K. Yoshikawa, M. Tsujikawa, T. Tsukahara, K. Nawaoka, Y. Kotani, K. Toyoki, M. Goto, M. Suzuki, T. Nakamura, M. Shirai, Y. Suzuki, and S. Miwa, Electric-field-induced changes of magnetic moments and magnetocrystalline anisotropy in ultrathin cobalt films, Phys. Rev. B **96**, 220412(R) (2017).

[108] R. Miyakaze, S. Sakamoto, T. Kawabe, T. Tsukahara, Y. Kotani, K. Toyoki, T. Nakamura, M. Goto, Y. Suzuki, and S. Miwa, Voltage-controlled magnetic anisotropy in an ultrathin nickel film studied by operando x-ray magnetic circular dichroism spectroscopy, Phys. Rev. B **102**, 014419 (2020).

[109] A. Idhil, C. N. Borca, A. Uldry, N. Zema, S. Turchini, D. Catone, A. Foelske, D. Grolimund, and M. Samaras, The influence of Cr-composition on the local magnetic structure of FeCr alloys, Nucl. Inst. Methods Phys. Res. B **284**, 1–5 (2012).

[110] B. H. Frazer, B. Gilbert, B. R. Sonderegger, and G. De Stasio, The probing depth of total electron yield in the sub-keV range: TEY-XAS and X-PEEM, Surf. Sci. **537**, 161–167 (2003).

[111] G. S. Henderson, F. M. F. D. Groot, and B. J. A. Moulton, X-ray Absorption Near-Edge Structure (XANES) Spectroscopy, Rev. Mineral. Geochemistry **78**, 75–138 (2014).

[112] W. Kang, L. Chang, Y. Zhang, and W. Zhao, Voltage-controlled MRAM for working memory: Perspectives and challenges, Des. Autom. Test Eur. Conf. Exhib. (DATE), 2017 , 542–547 (2017).

[113] T. Nozaki, T. Yamamoto, S. Miwa, M. Tsujikawa, M. Shirai, S. Yuasa, and Y. Suzuki, Recent Progress in the Voltage-Controlled Magnetic Anisotropy Effect and the Challenges Faced in Developing Voltage-Torque MRAM, Micromachines **10**, 327 (2019).

[114] A. Barman, G. Gubbiotti, S. Ladak, A. O. Adeyeye, M. Krawczyk, J. Gräfe, C. Adelmann, S. Cotofana, A. Naeemi, V. I. Vasyuchka, B. Hillebrands, S. A. Nikitov, H. Yu, D. Grundler, A. V. Sadovnikov, A. A. Grachev, S. E. Sheshukova, J. Y. Duquesne, M. Marangolo, G. Csaba, W. Porod, V. E. Demidov, S. Urazhdin, S. O. Demokritov, E. Albisetti, D. Petti, R. Bertacco, H. Schultheiss, V. V. Kruglyak,

V. D. Poimanov, S. Sahoo, J. Sinha, H. Yang, M. Münzenberg, T. Moriyama, S. Mizukami, P. Landeros, R. A. Gallardo, G. Carlotti, J. V. Kim, R. L. Stamps, R. E. Camley, B. Rana, Y. Otani, W. Yu, T. Yu, G. E. Bauer, C. Back, G. S. Uhrig, O. V. Dobrovolskiy, B. Budinska, H. Qin, S. Van Dijken, A. V. Chumak, A. Khitun, D. E. Nikonov, I. A. Young, B. W. Zingsem, and M. Winklhofer, The 2021 Magnonics Roadmap, J. Phys. Condens. Matter **33**, 413001 (2021).

[115] F. Groß, M. Zelent, N. Träger, J. Förster, U. T. Sanli, R. Sauter, M. Decker, C. H. Back, M. Weigand, K. Keskinbora, G. Schütz, M. Krawczyk, and J. Gräfe, Building Blocks for Magnon Optics: Emission and Conversion of Short Spin Waves, ACS Nano **14**, 17184–17193 (2020).

[116] F. Schulz, R. Lawitzki, H. Głowiński, F. Lisiecki, N. Träger, P. Kuświk, E. Goering, G. Schütz, and J. Gräfe, Increase of Gilbert damping in Permalloy thin films due to heat-induced structural changes, J. Appl. Phys. **129**, 153903 (2021).

[117] M. Zahedinejad, H. Mazraati, H. Fulara, J. Yue, S. Jiang, A. A. Awad, and J. Åkerman, CMOS compatible W/CoFeB/MgO spin Hall nano-oscillators with wide frequency tunability, Appl. Phys. Lett. **112**, 132404 (2018).

[118] B. Dieny and M. Chshiev, Perpendicular magnetic anisotropy at transition metal/oxide interfaces and applications, Rev. Mod. Phys. **89**, 025008 (2017).

[119] S. Miwa, M. Suzuki, M. Tsujikawa, T. Nozaki, T. Nakamura, M. Shirai, S. Yuasa, and Y. Suzuki, Perpendicular magnetic anisotropy and its electric-field-induced change at metal-dielectric interfaces, J. Phys. D. Appl. Phys. **52**, 063001 (2019).

[120] F. Bonell, M. Goto, G. Sauthier, J. F. Sierra, A. I. Figueroa, M. V. Costache, S. Miwa, Y. Suzuki, and S. O. Valenzuela, Control of Spin-

Orbit Torques by Interface Engineering in Topological Insulator Heterostructures, Nano Lett. **20**, 5893–5899 (2020).

[121] G. G. B. Flores and K. D. Belashchenko, Effect of interfacial intermixing on spin-orbit torque in Co/Pt bilayers, Phys. Rev. B **105**, 054405 (2022).

[122] K. Zhang, L. Chen, Y. Zhang, B. Hong, Y. He, K. Lin, Z. Zhang, Z. Zheng, X. Feng, Y. Zhang, Y. Otani, and W. Zhao, Efficient and controllable magnetization switching induced by intermixing-enhanced bulk spin-orbit torque in ferromagnetic multilayers, Appl. Phys. Rev. **9**, 011407 (2022).

[123] S. Brück, G. Schütz, E. Goering, X. Ji, and K. M. Krishnan, Uncompensated moments in the MnPd/Fe exchange bias system, Phys. Rev. Lett. **101**, 126402 (2008).

[124] C. Klewe, T. Kuschel, J. M. Schmalhorst, F. Bertram, O. Kuschel, J. Wollschläger, J. Strempfer, M. Meinert, and G. Reiss, Static magnetic proximity effect in Pt/ Ni_{1-x} Fe_x bilayers investigated by x-ray resonant magnetic reflectivity, Phys. Rev. B **93**, 214440 (2016).

[125] O. Inyang, L. Bouchenoire, B. Nicholson, M. Tokaç, R. M. Rowan-Robinson, C. J. Kinane, and A. T. Hindmarch, Threshold interface magnetization required to induce magnetic proximity effect, Phys. Rev. B **100**, 174418 (2019).

[126] A. Moskaltsova, J. Krieft, D. Graulich, T. Matalla-Wagner, and T. Kuschel, Impact of the magnetic proximity effect in Pt on the total magnetic moment of Pt/Co/Ta trilayers studied by X-ray resonant magnetic reflectivity, AIP Adv. **10**, 015154 (2020).

[127] A. Verna, P. Alippi, F. Offi, G. Barucca, G. Varvaro, E. Agostinelli, M. Albrecht, B. Rutkowski, A. Ruocco, D. Paoloni, M. Valvidares, and S. Laureti, Disclosing the Nature of Asymmetric Interface

Magnetism in Co/Pt Multilayers, ACS Appl. Mater. Interfaces **14**, 12766–12776 (2022).

[128] D. M. Burn, S. L. Zhang, G. Q. Yu, Y. Guang, H. J. Chen, X. P. Qiu, G. van der Laan, and T. Hesjedal, Depth-Resolved Magnetization Dynamics Revealed by X-Ray Reflectometry Ferromagnetic Resonance, Phys. Rev. Lett. **125**, 137201 (2020).

[129] V. Chardonnet, M. Hennes, R. Jarrier, R. Delaunay, N. Jaouen, M. Kuhlmann, N. Ekanayake, C. Léveillé, C. von Korff Schmising, D. Schick, K. Yao, X. Liu, G. S. Chiuzbăian, J. Lüning, B. Vodungbo, and E. Jal, Toward ultrafast magnetic depth profiling using time-resolved x-ray resonant magnetic reflectivity, Struct. Dyn. **8**, 034305 (2021).

[130] https://www.remagx.org.

[131] M. Born and E. Wolf, *Principles of Optics: 60th Anniversary Edition*, 7th ed. (Cambridge University Press, 2019).

[132] L. G. Parratt, Surface studies of solids by total reflection of x-rays, Phys. Rev. **95**, 359–369 (1954).

[133] L. Névot and P. Croce, Caractérisation des surfaces par réflexion rasante de rayons X. Application à l'étude du polissage de quelques verres silicates, Rev. Phys. Appliquée **15**, 761–779 (1980).

[134] M. Mansuripur, Analysis of multilayer thin-film structures containing magneto-optic and anisotropic media at oblique incidence using 2×2 matrices, J. Appl. Phys. **67**, 6466–6475 (1990).

[135] J. Zak, E. R. Moog, C. Liu, and S. D. Bader, Universal Approach to Magneto-Optics, J. Magn. Magn. Mater. **89**, 107–123 (1990).

[136] J. Zak, E. R. Moog, C. Liu, and S. D. Bader, Fundamental magneto-optics, J. Appl. Phys. **68**, 4203–4207 (1990).

[137] J. Zak, E. R. Moog, C. Liu, and S. D. Bader, Magneto-optics of multilayers with arbitrary magnetization directions, Phys. Rev. B **43**, 6423–6429 (1991).

[138] R. Röhlsberger, Theory of X-ray grazing incidence reflection in the presence of nuclear resonance excitation, Hyperfine Interact. **123**, 301–325 (1999).

[139] S. Stepanov and S. Sinha, X-ray resonant reflection from magnetic multilayers: Recursion matrix algorithm, Phys. Rev. B **61**, 15302–15311 (2000).

[140] D. R. Lee, S. K. Sinha, D. Haskel, Y. Choi, J. C. Lang, S. A. Stepanov, and G. Srajer, X-ray resonant magnetic scattering from structurally and magnetically rough interfaces in multilayered systems. I. Specular reflectivity, Phys. Rev. B **68**, 224409 (2003).

[141] M. Elzo, E. Jal, O. Bunau, S. Grenier, Y. Joly, A. Y. Ramos, H. C. Tolentino, J. M. Tonnerre, and N. Jaouen, X-ray resonant magnetic reflectivity of stratified magnetic structures: Eigenwave formalism and application to a W/Fe/W trilayer, J. Magn. Magn. Mater. **324**, 105–112 (2012).

[142] J. P. Hannon, G. T. Trammell, M. Blume, and D. Gibbs, X-ray Resonance Exchange Scattering, Phys. Rev. Lett. **61**, 1245–1248 (1988).

[143] L. G. Parratt and C. F. Hempstead, Anomalous dispersion and scattering of X-rays, Phys. Rev. **94**, 1593–1600 (1954).

[144] P. Colombi, D. K. Agnihotri, V. E. Asadchikov, E. Bontempi, D. K. Bowen, C. H. Chang, L. E. Depero, M. Farnworth, T. Fujimoto, A. Gibaud, M. Jergel, M. Krumrey, T. A. Lafford, A. Lamperti, T. Ma, R. J. Matyi, M. Meduna, S. Milita, K. Sakurai, L. Shabel'Nikov, A. Ulyanenkov, A. Van Der Lee, and C. Wiemer, Repro-

ducibility in X-ray reflectometry: Results from the first world-wide round-robin experiment, J. Appl. Crystallogr. **41**, 143–152 (2008).

[145] J. A. Nelder and R. Mead, A Simplex Method for Function Minimization, Comput. J. **7**, 308–313 (1965).

[146] K. Levenberg, A Method for the Solution of Certain Non-Linear Problems in Least Squares, Q. Appl. Math. **2**, 164–168 (1944).

[147] D. W. Marquardt, An Algorithm for Least-Squares Estimation of Nonlinear Parameters, J. Soc. Ind. Appl. Math. **11**, 431–441 (1963).

[148] D. Lawrence, *Handbook of genetic algorithms* (Van Nostrand Reinhold Company, 1991).

[149] A. Ulyanenkov and S. Sobolewski, Extended genetic algorithm: Application to x-ray analysis, J. Phys. D. Appl. Phys. **38**, A235 (2005).

[150] J. Tiilikainen, V. Bosund, M. Mattila, T. Hakkarainen, J. Sormunen, and H. Lipsanen, Fitness function and nonunique solutions in x-ray reflectivity curve fitting: Crosserror between surface roughness and mass density, J. Phys. D. Appl. Phys. **40**, 4259–4263 (2007).

[151] Quantum Design Web Page: https://qd-europe.com/de/en/product/mpms3-squid-magnetometer/ (accessed 28.02.2023) (2023).

[152] J. Clarke and A. I. Braginski, *SQUID Handb.* (Wiley Online Library, 2004).

[153] O. V. Lounasmaa, *Experimental principles and methods below 1K* (Academic Press Inc., Ltd., London, 1974).

[154] L. A. Giannuzzi and F. A. Stevie, A review of focused ion beam milling techniques for TEM specimen preparation, Micron **30**, 197–204 (1999).

[155] D. B. Williams and C. B. Carter, *Transmission Electron Microscopy* (Springer New York, NY, 1996).

[156] Q. Jiang, N. Kurra, and H. N. Alshareef, Marker Pen Lithography for Flexible and Curvilinear On-Chip Energy Storage, Adv. Funct. Mater. **25**, 4976–4984 (2015).

[157] J. Tripathi, B. Satpati, M. Oskar Liedke, A. Gupta, and T. Som, Effects of thermal annealing on structural and magnetic properties of thin Pt/Cr/Co multilayers, J. Magn. Magn. Mater. **322**, 3464–3469 (2010).

[158] A. Frisk, H. Ali, P. Svedlindh, K. Leifer, G. Andersson, and T. Nyberg, Composition, structure and magnetic properties of ultra-thin Fe/Ni multilayers sputter deposited on epitaxial Cu/Si(001), Thin Solid Films **646**, 117–125 (2018).

[159] P. Houdy, P. Boher, F. Giron, F. Pierre, C. Chappert, P. Beauvillain, K. L. Dang, P. Veillet, and E. Velu, Magnetic and structural properties of rf-sputtered Co/Fe and Co/Cr multilayers, J. Appl. Phys. **69**, 5667–5669 (1991).

[160] D. Kumar and A. Gupta, Effects of Interface Roughness on Interlayer Coupling in Fe/Cr/Fe Structure, Hyperfine Interact. **160**, 165–172 (2005).

[161] J. Tripathi, A. Gupta, and T. Som, Phase formation and changes in magnetic property of Co/Cr/ Pt multilayers, Surf. Coatings Technol. **203**, 2700–2702 (2009).

[162] M. Swain, D. K. Satapathy, M. Gupta, and M. S. R. Rao, Effect of thermal annealing on structure and magnetic properties in a Ni–Cr multilayer, Int. J. Mater. Res. **114**, 418–424 (2023).

[163] F. Petroff, A. Barthélémy, A. Hamzić, A. Fert, P. Etienne, S. Lequien, and G. Creuzet, Magnetoresistance of Fe/Cr superlattices, J. Magn. Magn. Mater. **93**, 95–100 (1991).

[164] E. E. Fullerton, D. M. Kelly, J. Guimpel, I. K. Schuller, and Y. Bruynseraede, Roughness and giant magnetoresistance in Fe/Cr superlattices, Phys. Rev. Lett. **68**, 859–862 (1992).

[165] P. Beliën, R. Schad, C. D. Potter, G. Verbanck, V. V. Moshchalkov, and Y. Bruynseraede, Relation between interface roughness and giant magnetoresistance in MBE-grown polycrystalline Fe/Cr superlattices, Phys. Rev. B **50**, 9957–9962 (1994).

[166] K. Adachi, Figs. 127 - 155, Tables 35 - 38: Datasheet from Landolt-Börnstein - Group III Condensed Matter. Volume 19A: 3d, 4d and 5d Elements, Alloys and Compounds (1986).

[167] K. Adachi, 3d, 4d and 5d Elements, Alloys and Compounds. 1.2.3.7 Co-Cr: Datasheet from Landolt-Börnstein - Group III Condensed Matter. Volume 19A: 3d, 4d and 5d Elements, Alloys and Compounds (1986).

[168] K. Adachi, 3d, 4d and 5d Elements, Alloys and Compounds. 1.2.3.11 Ni-Cr: Datasheet from Landolt-Börnstein - Group III Condensed Matter. Volume 19A: 3d, 4d and 5d Elements, Alloys and Compounds (1986).

[169] V. Uzdin and N. Yartseva, Fe/Cr interface magnetism in the external magnetic field, J. Magn. Magn. Mater. **203**, 280–282 (1999).

[170] Y. Henry, C. Mény, A. Dinia, and P. Panissod, Structural and magnetic properties of semiepitaxial Co/Cr multilayers, Phys. Rev. B **47**, 15037–15045 (1993).

[171] A. M. N. Niklasson, B. Johansson, and H. L. Skriver, Interface magnetism of 3d transition metals, Phys. Rev. B **59**, 6373–6382 (1999).

[172] S. E. Ilse, G. Schütz, and E. Goering, Voltage X-Ray Reflectometry: A Method to Study Electric-Field-Induced Changes in Interfacial Electronic Structures, Phys. Rev. Lett. **131**, 036201 (2023).

[173] H. Ohno, D. Chiba, F. Matsukura, T. Omiya, E. Abe, T. Dietl, Y. Ohno, and K. Ohtani, Electric-field control of ferromagnetism, Nature **408**, 944–946 (2000).

[174] D. Chiba, M. Yamanouchi, F. Matsukura, and H. Ohno, Electrical Manipulation of Magnetization Reversal in a Ferromagnetic Semiconductor, Science, **301**, 943–945 (2003).

[175] D. Chiba, M. Sawicki, Y. Nishitani, Y. Nakatani, F. Matsukura, and H. Ohno, Magnetization vector manipulation by electric fields, Nature **455**, 515–518 (2008).

[176] M. Weisheit, S. Fähler, A. Marty, Y. Souche, C. Poinsignon, and D. Givord, Electric field-induced modification of magnetism in thin-film ferromagnets, Science, **315**, 349–351 (2007).

[177] R. A. One, H. Béa, S. Mican, M. Joldos, P. B. Veiga, B. Dieny, L. D. B. Prejbeanu, and C. Tiusan, Route towards efficient magnetization reversal driven by voltage control of magnetic anisotropy, Sci. Rep. **11**, 8801 (2021).

[178] G. Van Der Laan, Microscopic origin of magnetocrystalline anisotropy in transition metal thin films, J. Phys. Condens. Matter **10**, 3239–3253 (1998).

[179] C. G. Duan, J. P. Velev, R. F. Sabirianov, Z. Zhu, J. Chu, S. S. Jaswal, and E. Y. Tsymbal, Surface magnetoelectric effect in ferromagnetic metal films, Phys. Rev. Lett. **101**, 137201 (2008).

[180] K. Nakamura, R. Shimabukuro, Y. Fujiwara, T. Akiyama, T. Ito, and A. J. Freeman, Giant modification of the magnetocrystalline

anisotropy in transition-metal monolayers by an external electric field, Phys. Rev. Lett. **102**, 187201 (2009).

[181] M. Tsujikawa and T. Oda, Finite electric field effects in the large perpendicular magnetic anisotropy surface Pt/Fe/Pt(001): A first-principles study, Phys. Rev. Lett. **102**, 247203 (2009).

[182] J. Zhang, P. V. Lukashev, S. S. Jaswal, and E. Y. Tsymbal, Model of orbital populations for voltage-controlled magnetic anisotropy in transition-metal thin films, Phys. Rev. B **96**, 014435 (2017).

[183] S. Miwa, M. Suzuki, M. Tsujikawa, K. Matsuda, T. Nozaki, K. Tanaka, T. Tsukahara, K. Nawaoka, M. Goto, Y. Kotani, T. Ohkubo, F. Bonell, E. Tamura, K. Hono, T. Nakamura, M. Shirai, S. Yuasa, and Y. Suzuki, Voltage controlled interfacial magnetism through platinum orbits, Nat. Commun. **8**, 15848 (2017).

[184] B. El-Kareh, *Fundamentals of Semiconductor Processing Technology* (Springer New York, NY, 1995).

[185] W. Demtröder, Experimentalphysik 2 - Elektrizität und Optik (Springer Berlin, Heidelberg, 2009).

[186] T. Nishizawa and K. Ishida, The Co-Ni (Cobalt-Nickel) system, Bull. Alloy Phase Diagrams **4**, 390–395 (1983).

[187] D. B. Boltje, *Voltage induced near interface changes of the magnetocrystalline anisotropy energy*, Master thesis, University Stuttgart (2017).

[188] K. Ohta and H. Ishida, Comparison among several numerical integration methods for Kramers-Kronig transformation, Appl. Spectrosc. **42**, 952–957 (1988).

[189] S. M. Sze and K. K. Ng, *Physics of Semiconductor Devices* (John Wiley and Sons, Ltd, 2006).

[190] M. Miller, *Voltage Dependent Investigation on the Spin Polarization of Layered Heterostructures*, Master thesis, University Stuttgart (2022).

[191] R. Wu and A. J. Freeman, Limitation of the magnetic-circular-dichroism spin sum rule for transition metals and importance of the magnetic dipole term, Phys. Rev. Lett. **73**, 1994–1997 (1994).

[192] J. Krieft, D. Graulich, A. Moskaltsova, L. Bouchenoire, S. Francoual, and T. Kuschel, Advanced data analysis procedure for hard x-ray resonant magnetic reflectivity discussed for Pt thin film samples of various complexity, J. Phys. D. Appl. Phys. **53**, 375004 (2020).

Wissenschaftlicher Werdegang

Wissenschaftlicher Lebenslauf

Promotionsstudium **Februar 2018 - August 2023**
Universität Stuttgart

Dissertation mit dem Titel: Correlated Voltage Dependent- and Magnetic-Reflectometry at Transition Metal/Insulator Heterostructures. Unter der Betreuung von Eberhard Goering am Max Planck Institut für Intelligente Systeme (bis März 2023) und am Max-Planck-Institut für Festkörperforschung (ab April 2023), Stuttgart.

Masterstudium Physik **Oktober 2015 - November 2017**
Universität Stuttgart

Masterarbeit mit dem Titel: Using FORC to Understand the Microstructure-Micromagnetism Relationship in Supermagnets. Unter der Betreuung von Eberhard Goering am Max Planck Institut für Intelligente Systeme, Stuttgart.

Bachelorstudium Physik **Oktober 2012 - Oktober 2015**
Universität Stuttgart

Bachelorarbeit mit dem Titel: Motility Induced Phase Separation of Active Triangles with Surface Roughness. Unter der Betreuung von Joost De Graaf am Institut für Computerphysik, Universität Stuttgart.

Publikationsliste

- **S. E. Ilse**, G. Schütz, E. Goering. Voltage X-Ray Reflectometry: A Method to Study Electric-Field-Induced Changes in Interfacial Electronic Structures. Physical Review Letters, 131, 036201, 2023.
- **S. E. Ilse**, René Nacke, G. Schütz, E. Goering. Disentangling Different Interfacial Effects of Reduced Thin Layer Magnetizations. In preparation (2023).
- S. Soltan, S. Macke, **S. E. Ilse**, T. Pennycook, Z. L. Zhang, G. Christiani, E. Benckiser, G. Schütz, E. Goering. Ferromagnetic order controlled by the magnetic interface of $LaNiO_3/La_{2/3}Ca_{1/3}MnO_3$ superlattices. Scientific Reports 13(1), 3847, 2023.
- L. Wysocki*, **S. E. Ilse***, L. Yang, e. Goering, F. Gunkel, R. Dittmann, P. H. M. Van Loosdrecht, I. Lindfors-Vrejoiu. Magnetic interlayer coupling between ferromagnetic $SrRuO_3$ layers through a $SrIrO_3$ spacer. Journal of Applied Physics 131(13), 133902, 2022.
  * L. Wysocki and S.E. Ilse contributed equally to this work.
- P. Radhakrishnan, B. Geisler, K. Fürsich, D. Putzky, Y. Wang, **S. E. Ilse**, G. Christiani, G. Logvenov, P. Wochner, P. A. Van Aken, E. Goering, R. Pentcheva, E. Benckiser. Orbital engineering in YVO_3-$LaAlO_3$ superlattices. Physical Review B, 104(12), L121102, 2021.

- J. Gräfe, F. Groß, **S. E. Ilse**, D. B. Boltje, S. Muralidhar, E. Goering. LeXtender: A software package for advanced MOKE acquisition and analysis. Measurement Science and Technology, 32(6), 067002, 2021.

- **S. E. Ilse**, F. Groß, G. Schütz, J. Gräfe, E. Goering. Understanding the interaction of soft and hard magnetic components in NdFeB with first-order reversal curves. Physical Review B, 103(2), 024425, 2021.

- F. Groß, J. C. Martínez-García, **S. E. Ilse**, G. Schütz, E. Goering, M. Rivas, J. Gräfe.GFORC: A graphics processing unit accelerated first-order reversal-curve calculator. Journal of Applied Physics 126(16), 163901, 2019.

- F. Groß, **S. E. Ilse**, G. Schütz, J. Gräfe, E. Goering. Interpreting first-order reversal curves beyond the Preisach model: An experimental permalloy microarray investigation. Physical Review B, 99(6), 064401, 2019.

- **S. E. Ilse**, C. Holm, J. De Graaf. Surface roughness stabilizes the clustering of self-propelled triangles. The Journal of Chemical Physics, 145(13), 134904, 2016.

Konferenzbeiträge

- S. E. Ilse, G. Schütz, E. Goering. Identifying the Origin of Reduced Magnetization in Buried Thin Layers.
  Posterpräsentation: *15th Joint International Magnetics Conference and Magnetism and Magnetic Materials Conference, New Orleans, USA*

- S. E. Ilse, D. B. Boltje, G. Schütz, E. Goering. X-ray resonant magnetic reflectometry (XRMR) study of the interface between ferromagnetic transition metals and MgO.
  Posterpräsentation: *3rd IEEE Conference on Advances in Magnetism 2020/21, Virtual Conference.*

- S. E. Ilse, D. B. Boltje, G. Schütz, E. Goering. X-ray resonant magnetic reflectometry (XRMR) study of the interface between ferromagnetic transition metals and MgO.
  Posterpräsentation: *64th Annual Conference on Magnetism and Magnetic Materials, Las Vegas, USA*

- S. E. Ilse, D. B. Boltje, G. Schütz, E. Goering. X-ray resonant magnetic reflectometry (XRMR) study of the interface between ferromagnetic transition metals and MgO.
  Posterpräsentation: *Frühjahrstagung der DPG 2019 in Regensburg, Deutschland.*

- S. E. Ilse, F. Groß, G. Schütz, J. Gräfe, E. Goering. Quantifying micromagnetic interactions in NdFeB by using FORC.
  Vortrag: *14th Joint International Magnetics Conference and Magnetism and Magnetic Materials Conference, Washington DC, USA.*

- S. E. Ilse, D. B. Boltje, G. Schütz, E. Goering. X-ray resonant magnetic reflectometry (XRMR) study of the interface between ferromagnetic transition metals and MgO.
  Posterpräsentation: *10th Joint BER II and BESSY II User Meeting 2018, Berlin, Deutschland.*

- S. E. Ilse, F. Groß, J. Gräfe, E. Goering. Quantifying micromagnetic Interactions in NdFeB by using FORC.
  Posterpräsentation: *The European School on Magnetism 2018 in Krakau, Polen.* (Received Best Poster Prize)

- S. E. Ilse, F. Groß, J. Gräfe, E. Goering. Using FORC to Understand the Microstructure-Micromagnetism Relationship in Supermagnets. Vortrag: *21st International Conference on Magnetism 2018, San Francisco, USA.*

- S. E. Ilse, F. Groß, J. Gräfe, E. Goering. Using FORC to understand the microstructure-micromagnetism relationship in supermagnets. Vortrag: *Frühjahrstagung der DPG 2018 in Berlin, Deutschland.*

- S. E. Ilse, F. Groß, J. Gräfe, E. Goering. Grain size dependent FORC investigations on rare earth based permanent magnets. Vortrag: *2nd IEEE Conference on Advances in Magnetism 2018, La Thuile, Italy.*

Danksagung

Abschließend möchte ich meinen Dank an alle aussprechen, die zum erfolgreichen Gelingen dieser Arbeit beigetragen und mich während meiner Zeit als Doktorand in unterschiedlichster Weise unterstützt haben. Besonders bedanken möchte ich mich bei:

- Privatdozent Dr. Eberhard „Ebs“ Goering für die Betreuung meiner Doktorarbeit, dafür dass seine Bürotür immer offen war wenn ich Fragen hatte, für die tatkräftige Unterstützung während der Strahlzeiten bei BESSY II und für seine unendliche Begeisterung für Physik, die mich immer wieder mitgerissen hat.
- Professor Dr. Peter Michler für die Übernahme des Mitberichts meiner Doktorarbeit.
- Professor Dr. Thomas Speck für die Übernahme des Prüfungsvorsitzes bei meiner Promotionsprüfung.
- Professor Dr. Gisela Schütz für die Möglichkeit, meine Doktorarbeit in ihrer Abteilung *Moderne Magnetische Systeme* am Max-Planck-Institut für Intelligente Systeme durchzuführen.
- Dr. Frank Schulz und Dr. Felix Groß für die *exciting & dynamic* Zeit im Büro 4E4. All die wissenschaftlichen und nicht-wissenschaftlichen

Diskussionen haben unsere gemeinsame Doktorandenzeit geprägt und unvergesslich gemacht. Wir haben so viel zusammen und voneinander gelernt. Ihr habt mich immer unterstützt und wieder aufgebaut wenn ich in einer Sackgasse gelandet bin.

- Daan Boltje für die Unterstützung am Anfang meiner Doktorarbeit.
- Dr. Joachim Gräfe und Dr. Nick Träger für anregende wissenschaftliche Diskussionen und die gemeinsame Zeit auf Konferenzen.
- Bernd Ludescher für die Hilfe bei der Herstellung meiner Proben und Unterstützung bei der Wartung von ERNSt.
- René Nacke für die Strahlzeit-Unterstützung.
- Ulrike Eigenthaler für die Präparation von TEM Lamellen.
- Kersten Hahn und der Wissenschaftlichen Einrichtung *Stuttgarter Zentrum für Elektronenmikroskopie* von Prof. Dr. Peter van Aken für die Hilfe bei TEM Messungen.
- Monika Kotz für ihre Unterstützung bei allen administrativen Problemen und auch bei persönlichen Anliegen.
- Der ganzen Abteilung Schütz mit allen ehemaligen Kollegen, für die entspannte Arbeitsatmosphäre, die Kaffeepausen und Kickerrunden.
- Professor Dr. Bernhard Keimer dafür, dass ich zum Ende meiner Doktorarbeit zusammen mit Ebs in seine Abteilung am Max-Planck-Institut für Festkörperforschung wechseln durfte.
- Meinen Freunden, für die schönen Momente und großartigen Erlebnisse, die wir gemeinsam erleben durften und für die Ablenkung vom physikalischen Alltag.
- Meinen Mannschaftskollegen, ohne den sportlichen Ausgleich beim Handball hätte ich das nicht geschafft.

- Meiner Freundin Anja, die mich in der Schlussphase meiner Doktorarbeit unendlich unterstützt und mich in dieser stressigen Phase ertragen hat.
- Meinen Eltern und Geschwistern für die immerwährende Unterstützung und Liebe. Das Gefühl, dass ich mich immer auf euch verlassen kann, gibt mir so viel Rückhalt.

Danke!